Programming the Energy Landscape of 3D-Printed Kresling Origami via Crease Geometry and Viscosity

Samantha Mora[1,2], Nicola M. Pugno[2,3], Diego Misseroni[1*]

[1] Department of Civil, Environmental and Mechanical Engineering, University of Trento, Italy.

[2]Laboratory for Bioinspired, Bionic, Nano, Meta Materials and Mechanics,
Department of Civil, Environmental and Mechanical Engineering, University of Trento, Italy.

[3]School of Engineering and Materials Science, Queen Mary University of London, UK.

[*]Corresponding author. Email: diego.misseroni@unitn.it

Origami extends beyond intricate paper creations, envisioning revolutionary engineering applications. While 3D printing has simplified fabricating complex structures, Kresling origami remains predominantly paper based due to the challenge of achieving multistable behavior, especially at a small scale. Our study focuses on investigating modifications to the energy landscape induced by changes in crease geometrical parameters, addressing the effects of viscoelasticity in the creases. The latter aspect is investigated using different rubbery materials with varying relaxation moduli. Considering the limitations of manufacturing techniques, we also provide design insights for crease geometry and distribution, along with photopolymers suitable for fabricating both multi- and monomaterial bistable cells, at both micro- and macro- scales. By leveraging 3D printing and overcoming its material and technological constraints, our goal is to contribute to a deeper understanding of the mechanics of 3D printed materials and broaden their applications into new frontiers.

Keywords: Origami, Metamaterials, Multistability, Multi-Material printing, Viscoelasticity.

1 Introduction

Once origami has surpassed the barrier of being merely decorative folded paper objects, it has become a source of inspiration for creating groundbreaking devices across various engineering fields (*1*). Kresling origami is currently one of the most studied origami patterns for the development of versatile structures, particularly in the programmable soft robotics area (*2–9*), highly deployable and energy absorption devices (*10–14*), and wave control metastructures (*15–18*). Kresling origami is considered a natural twisted buckling shape that results from the compression of two interacting tubes. This pattern can also be identified in nature, for example, in the bellows shapes found in the abdomen of hawk-moths (*19, 20*). The intrinsic bistability exhibited by a single Kresling cell, permits the achievement of controlled compliant mechanisms and in the case of coupled Kresling cell modules, multistability (*21–27*). The material characteristics of the creases play a key role in Kresling origami mechanics, regulating the contraction/expansion process, tailoring the overall stiffness, and leading to mono or bistable behaviour (*28*). Thus, the creases become essential components for controlling the energy landscape of the Kresling cell. Manual, subtractive and additive manufacturing processes have been used for the fabrication of Kresling structures with materials different than the traditional paper or cardboard. This is mostly done at the macro and meso-scale. Since multi-material 3D printing techniques, such as Material Jetting (MJ), Fused Deposition Modeling (FDM), or Fused Filament Fabrication (FFF), enable a more direct methodology to manufacture complex origami shapes and the use of rigid and flexible materials during a single printing round, their popularity has been increasing among academics and industry. There are current examples that exploit these techniques for the fabrication of Kresling structures, with panels made up of stiffer materials and softer creases that act as hinges. It allows for a smoother transition between an expanded and a compressed state, or vice-versa, by using different photopolymers (*29–31*) or filaments (*32–36*). In addition, the use of flexible creases improves the fatigue resistance and life cycle of the Kresling cells (*37*). Resin-based techniques, such as MJ, offer the possibility to build objects with high precision (layers 16-27 microns), a lower level of anisotropy (<5%), smoother surface finishing, fewer support removal operations, stronger interface bond be-

tween rigid and flexible parts, and a broader range of soft photopolymers for fabricating flexible creases, compared to other multi-material printing processes.These types of soft photopolymers are characterized by a long-range crystalline order, which enhances their mechanical strength and enables tunable deformation responses (*38*). However, this type of 3D printing photo-resins exhibits an inherent viscoelastic (*39*) behavior that can lead to a temporary bistability in Kresling cells and a gradual loss of stiffness over time. Consequently, the expected achievement of this mechanical characteristic in theory tends to be compromised in practice, and the Kresling cells return to their initial configuration prematurely. Moreover, the technological limitations of most multi-material 3D printers could restrict the possibility of miniaturizing devices, especially in demanding sectors such as biomedical for the fabrication of drug delivery soft robotics. For instance, the minimum wall thickness is constrained by the nozzle size of extrusion printers in FDM and FFF techniques, typically ranging from 0.25 mm to 1.00 mm depending on the current printer series (*40, 41*). Regarding MJ, producing strong load-bearing elements with less than 1.0 mm thickness is restricted due to the likelihood of presenting defects (*42*). Furthermore, the majority of the ”micro-scale” printers currently available in the market still utilize a single photo-resin. Therefore, this limitation prevents direct fabrication of Kresling cells with the required difference in stiffness between rigid panels and soft creases, and this feature is essential for facilitating the characteristic contraction/expansion mechanism, as seen in multi-material techniques.

1.1 Motivation and outline

The outcomes of our study provide design insights for programming the energy landscape of 3D printed Kresling cells, counteracting the material and technological limitations in 3D printing. Our goal is to enable the manufacturing of more precise, reliable, scalable and multistable Kresling structures. We explored two main manufacturing approaches: Multi-material and Mono-material. In the multi-material scenario, rigid and rubbery photopolymers are assigned to the panels and creases, respectively. Although the bending of the panels plays a significant role in the folding of non-rigid Kresling cells, as seen in paper-based models, we chose to print the panels using rigid materials to better understand the role of the geometry of the creases on the energy landscape of the Kresling cell. Therefore, the primary folding relies mostly on the flexible, rubbery-like creases.

We initially defined the fundamental geometrical parameters of a cylindrical Kresling cell to achieve theoretical bistability and developed parametric 3D models based on this configuration, as illustrated in Fig. 1A. However, the viscoelastic nature of rubbery photopolymers interferes with practical bistability, causing the cell to prematurely return to its original configuration during the compression/expansion process. Then, we implemented a design strategy that involved gradually reducing the cross-section of the crease geometries. This created peak and valley creases with V+circular shapes, variable widths (w), and internal thicknesses (s_i). A parametric study was conducted to assess the influence of these reductions on cross-section and rotational stiffness, using Reduction Factors (RF) ranging from $0.25 \leq RF \leq 0.80$, as shown in Fig. 1B. These gradual reductions facilitated transitions between bistable (Bi), and monostable (M) behavior, as detailed in the results section 2.

The bistable behavior is related to a Kresling cell whose energy landscape exhibits a second local minimum of energy, and negative force in the load path. We categorized the behavior as monostable when the Kresling cell's load path does not intersect its displacement axis at zero load (*43*).

Time-dependent stress-strain responses and energy loss are key characteristics of viscoelastic materials, which exhibit residual strain that recovers over time, allowing the material to return to its original state. This results in temporary bistability. Once stress relaxation occurs, stability is lost, and the structure gradually returns to its initial configuration. In our second analysis, we evaluated these effects in bistable multi-material Kresling cells with rubbery photopolymer creases of varying relaxation moduli. In the numerical simulations, we considered elasto-plastic and visco-hyperelastic models with 3D hybrid formulation elements to accurately capture the mechanical behavior of 3D-printed rigid and rubbery photopolymers, respectively. This approach offers a more realistic alternative to traditional 2D origami models, particularly for materials such as paper or thin polymeric sheets.

We experimentally validated the load paths and energy landscapes obtained numerically by testing 3D-printed Kresling cells fabricated using the Polyjet technique. In addition, we performed microscopic characterization of the rubbery creases to assess potential dimensional discrepancies between the CAD model and actual printed dimensions, as illustrated in Fig. 1C. Lastly, we explored alternative designs for a mono-material bistable cell, as depicted in Fig. 1D, aimed

at microfabrication. The stiffness differences between creases and panels are achieved through geometric reductions, including voids along the peaks and valleys. Furthermore, we also investigated the effects of various 3D printing photo-resins on Kresling multistability and the programmability of monostable Kresling assemblies through crease stiffness distribution.

2 Results

2.1 Parametric study of creases geometry for Bistability

First, we selected the following initial sizing configuration for the parametric design of 3D Kresling cells, shown in Fig. 1A: polygons with n=6 sides, initial relative angle $\theta_o = \pi/6$, and an aspect ratio h_o/r=1.75, as detailed in sections S.1.1 and S.1.2 of Supplementary Materials and Methods. Initially, we analyzed Kresling cells with intact crease cross-sections. The results showed that their bistability was compromised by a sudden return to the initial configuration, attributed to the viscosity of the rubbery creases (as further explained in the Supplementary Text S.2.1).

As a design strategy to achieve bistability and program energy landscapes, we conducted a parametric study to assess how gradually reducing crease cross-sections influences the energy landscape. The geometrical changes illustrated in Fig. 1B were proposed based on the following procedure: The upper V-shape remained constant, preserving the crease width w, while the bottom part was gradually reduced by considering a variable cutting radius s_c. It encompasses a circumference with its center at the extreme vertex o. Using imposed reduction factors, denoted as RF, we can control the decrease of the parameter s_c relative to the limiting crease radius r', and thereby determine the extent of crease cross-section reduction. Accordingly, we can define the reduction factor as: $RF = s_c/r'$.

We then introduced a new geometrical parameter corresponding to the internal thickness s_i. This term represents the difference between the external thickness s and the variable cutting-radius s_c, which depends on the selected reduction factor RF. As the RF values increase, the generated creases exhibit smaller internal thickness s_i and these gradual reductions can be quantified as the ratios of the reduced to intact cross-sections, $\tilde{A}/A$, and their corresponding rotational stiffness, $\tilde{K}/K$. Here, the reduced cross-sections and corresponding rotational stiffness are denoted by $\tilde{A}$ and

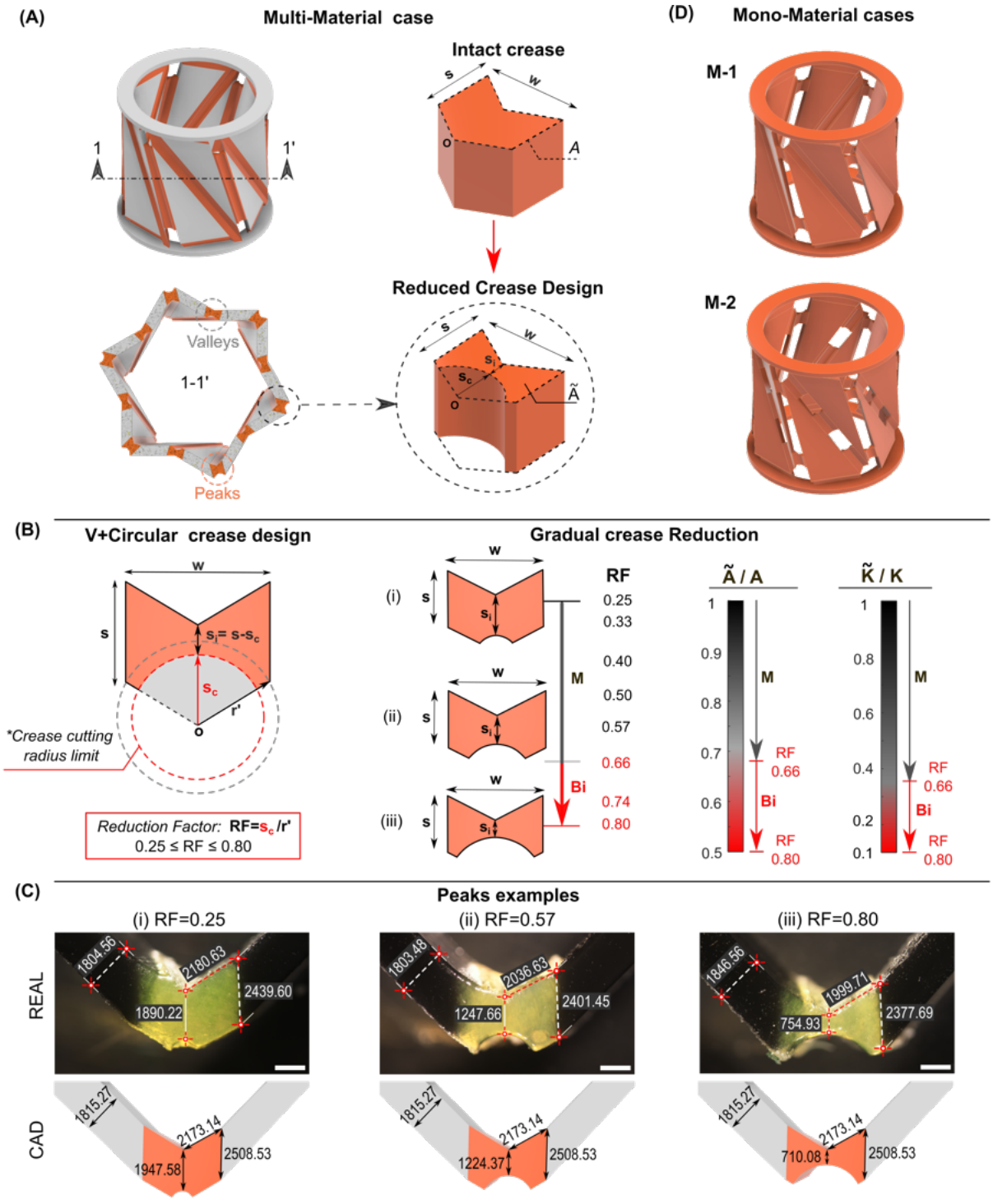

Figure 1: **3D models of the Kresling cell.** (**A**) Multi-material (MM) with crease design cases. (**B**) Crease cross-section gradual reductions derived from the former intact creases cross-sections, A, with a variable width-thickness ratio w/s, an internal thickness s_i obtained from cutting radius s_c and reduction factors RF. Here, $\tilde{A}$ and A represent the reduced and intact cross-sections, respectively. Similarly, $\tilde{K}$ denotes the rotational stiffness of the reduced cross-sections, while K corresponds to that of the intact cross- sections. (**C**) Comparison between 3D printed creases dimensions taken from microscope images and CAD files of case C8 with gradual reductions. Units: microns. Scale bar:1 mm. (**D**) Mono-material cases M-1 and M-2.

$\tilde{K}$, respectively, while the intact cross-section and its rotational stiffness are denoted as A and K.

As a result, the proposed variable creases geometry consists of a combined V+circular typology, yielding a series of Kresling cell cases to be analyzed in terms of the parameters: w, RF, s_i, and s. Thereby, we introduced eleven main cases, C1 to C11, derived from the variation of the width with respect to the external thickness, expressed as the ratio w/s=0.50, 0.60, 0.75, 0.90, 1.07, 1.20, 1.35, 1.50, 1.65, 1.80, 2.00. The gradual reductions applied to each of the main cases are represented by the variations in internal thickness s_i, which directly depend on the reduction factors, denoted as RF= 0.25, 0.33, 0.40, 0.50, 0.57, 0.66, 0.74, and 0.80. This process subdivided each crease case into eight sub-cases, each corresponding to one of the specified RF values. The load paths and stored energy landscapes of the generated geometrical combinations were obtained through numerical simulations, as detailed in Supplementary Text S.2.2, using a multi-material approach. A rigid photopolymer (VB), modeled as an elasto-plastic material, was assigned to the panels. A rubbery photopolymer (DM60), modeled as a visco-hyperelastic material, was assigned to the creases. For this, we incorporated viscoelastic parameters into its characteristic hyperelastic behavior, such as the Prony series coefficients (g_i, τ_i) and relaxation moduli ($G(t)$), as explained in sections 5.3, and S.1.3 of Supplementary Materials and Methods. Then, the effect of the gradual reduction of the creases on the energy landscape was evaluated based on the variation of the width w and internal thickness s_i with respect to the external thickness s, denoted as the ratios w/s and s_i/s, respectively.

Thereafter, in Fig. 2A, we show which geometrical combinations exhibited a bistable, or monostable behavior, along with their rotational stiffness $\tilde{K}$, estimated using the bending formulations of an incompressible elastic Neo-Hookean block (*44*) (as detailed in Supplementary Text S.2.3). For instance, the Kresling cells that satisfied the bistability criteria were made of wider creases ($1.07 \leq w/s \leq 2.00$) and designed with greater cross-section reductions ($0.58 \geq s_i/s \geq 0.05$). The latter were generated by reduction factors relying on the range $0.66 \leq RF \leq 0.80$. Such reduction factors enabled the creation of creases with the thinnest internal thicknesses s_i, resulting in the highest decrement of cross-section and rotational stiffness up to $\tilde{A}/A$=0.50 and $\tilde{K}/K$=0.10 compared to the corresponding intact creases, as shown in Fig. 1B. Therefore, this confirms that as the crease becomes less stiff, it gains enough flexibility to ensure the achievement of bistability. On the other hand, creases designed with reduction factors below RF=0.66 reached greater internal

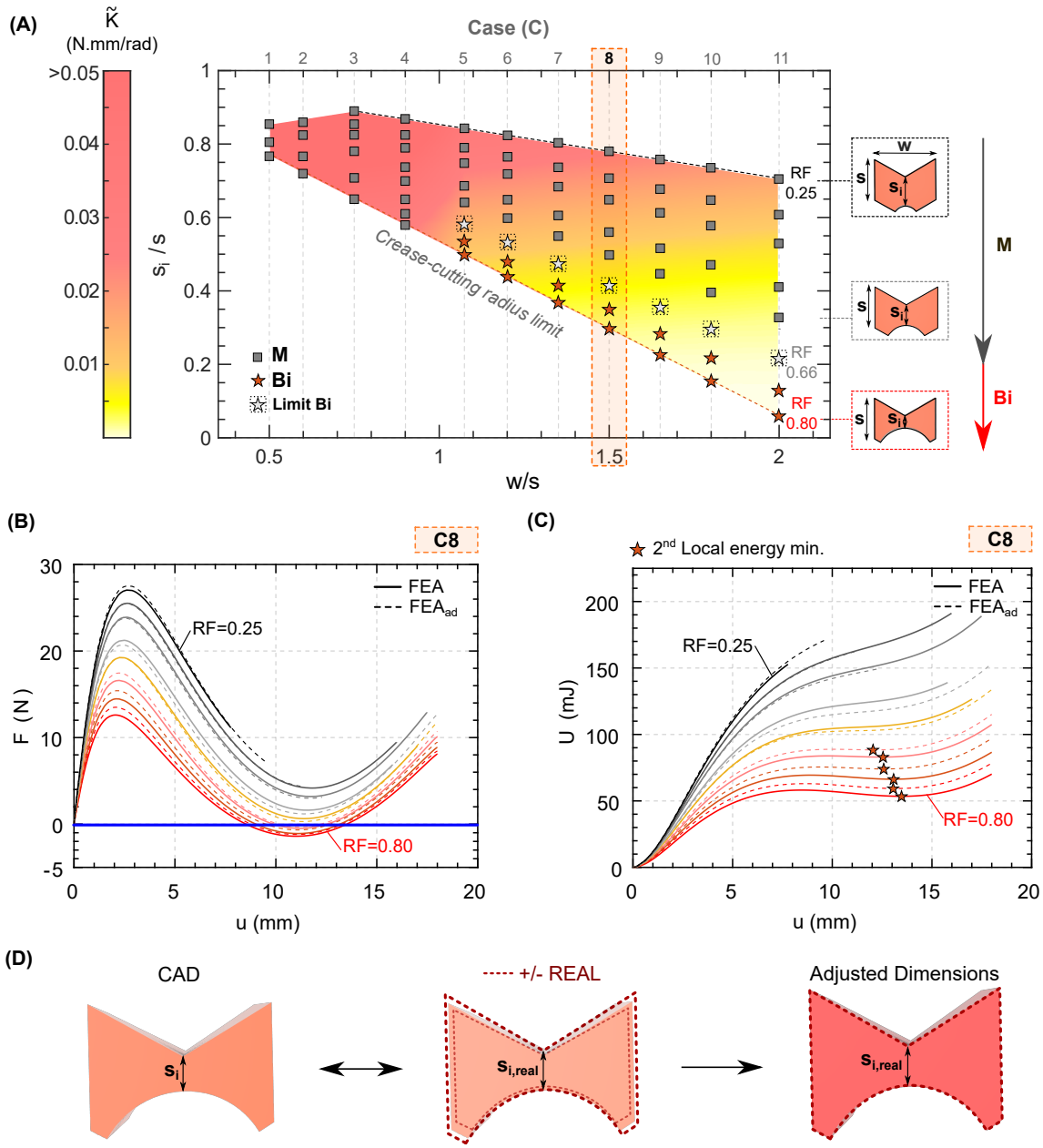

Figure 2: **Influence of the creases geometrical parameters on the energy landscape.** (**A**) Parametric study of creases to evaluate the achievement of bistability (Bi), or monostability (M), in terms of the variation of width (w) and internal thickness (s_i) with respect to the external thickness (s), reduction factors (RF) and Rotational Stiffness ($\tilde{K}$). The crease-cutting radius limit determines the range of reduction factors necessary to maintain a circular shape at the lower part of the crease. 'Limit Bi': boundary between bistability and monostability determined experimentally. Results are based on Kresling cells at 1:1 scale (x1). (**B**) Load paths and (**C**) stored energy (U) landscapes of case C8 (w/s=1.50) at 3:1 scale (x3). The corresponding curves are presented in the following order RF: 0.25, 0.33, 0.40, 0.50, 0.57, 0.66, 0.74, and 0.80. (**D**) Iterative process to adjust CAD dimensions, verify discrepancies with the real dimensions of 3D-printed Kresling cells, and determine the corresponding adjusted load paths (FEA_{ad}).

thickness (s_i) values. They tend to increase the restoring force values of the respective Kresling cells, gradually moving them away from zero. Therefore, they are unable to achieve bistability and are prone to show a monostable behavior instead. Thus, we determined a possible limit for achieving bistability from the combinations with $RF \geq 0.66$, as shown in Fig. 2A.

In an extreme scenario, when the width versus external thickness ratio is below $w/s \leq 1.07$, the creases tend to be narrower and very rigid, falling into a mono-stable category, and when they presented higher s_i values, the stored energy values also increased. In general, we observed that Kresling cells exhibited monostable behaviors when they are formed by stiffer creases. These crease configurations reached reduction ratios of approximately $\tilde{A}/A \geq 0.70$ for cross-sections and $\tilde{K}/K \geq 0.30$ for rotational stiffness. Moreover, we analyzed the load paths and the corresponding stored energy obtained numerically for the intermediate case C8 (w/s=1.50), as shown in Fig. 2B, and Fig. 2C. We compared two types of numerical simulations, the first considering the exact cross-section dimensions from the CAD file and the second with the adjusted dimensions obtained from the microscope characterization, indicated as FEA and FEA_{ad}, respectively. We also observed that a second local minimum of energy was reached when the creases presented gradual reductions between the range $0.40 \geq s_i/s \geq 0.35$ corresponding to the already mentioned reduction factors $0.66 \leq RF \leq 0.80$.

2.2 Scalability and experimental validation

Furthermore, we observed through numerical simulations that the load paths of the analyzed Kresling cells can be scaled. For instance, Fig.3A shows that the position of the second local minimum of energy of the C8 RF=0.80 Kresling cell, at a 1:1 scale (x1), varies from a displacement u=4.53 mm, to 9.06 mm at a 2:1 scale (x2) and 13.59 mm at a 3:1 scale (x3). This fact demonstrates that scaled Kresling cells maintained the expected bistable behavior at the same geometrical proportions with respect to 1:1 scale (x1). Thus, Kresling cells can be scaled to meet manufacturing requirements across different length scales, from microfabrication to large-scale additive manufacturing. In the present study, Kresling cells for the C8 case were fabricated using the PolyJet technique at a 3:1 scale (x3) for the corresponding experiments, as detailed in section 5.4. This scale ensures feasible printing, as the internal thickness dimensions s_i, fall within the PolyJet manufacturing limits of

0.6–1.0 mm.

The experimental setup for the compression tests is illustrated in Fig. 3B. The experiments were performed by imposing a displacement u at one side of the sample and leaving free the rotation in the opposite side, as detailed in section 5.5. During the test we monitored the applied displacement u against the measured restoring force F. Moreover, the achievement of bistability is highly sensitive to geometric variations in crease parameters, such as width w and internal thickness s_i. The existent differences between the exact (CAD) and the real dimensions of the 3D printed Kresling cells are attributed to the inherent loss of dimensional accuracy of the 3D printer in use.

Thorough a microscopic characterization (further explained in sections 5.6, and S.1.10 of Supplementary Materials and Methods), we estimated a mean percentage error, M_{PE} (%), between the exact and the real dimensions of the analyzed creases and panels from a sample corresponding to the case C8. In this example, the internal thickness s_i dimensions exhibited an mean percentage error in the range: -25 $\leq M_{PE}$ (%) $\leq$ 10, where negative values imply higher real measures than the CAD models. This error range represents a small difference between the exact dimensions and the real dimensions of the creases, and corresponds to the expected dimensional accuracy of a J750 Polyjet 3D printer, which is commonly about 10%. Therefore, we primarily relied on the load paths obtained from the numerical simulations (FEA) using the exact dimensions from the CAD file geometry for their respective experimental validation, as shown in Fig. 3C, D and E.

Subsequently, we experimentally confirmed that C8 case samples with reduction factors in the range $0.25 \leq RF \leq 0.57$ exhibited monostability, as illustrated in Fig. 3C. These cases corresponded to creases with internal thickness s_i greater than the manufacturing limit of 1.0 mm. The effect of crack formation during the experiments on these thicker creases was minimized. For this reason, the numerical load paths (FEA) closely matched those obtained experimentally (EXP). In Fig. 3D, the experiments from C8 cases with $0.74 \leq RF \leq 0.80$ validated the bistable behavior observed in the corresponding Kresling cells at a 1:1 scale, as described in Fig. 2A.

However, some discrepancies were observed in the load path region where a change in the sign of the load was expected. This may be attributed to the fact that these narrow creases, with thicknesses below the manufacturing limit of 0.6 mm, are prone to develop longitudinal cracks that dramatically reduce their stiffness. In addition, the load path corresponding to the configuration with a reduction factor of $RF = 0.66$ may represent the actual limit between bistability and

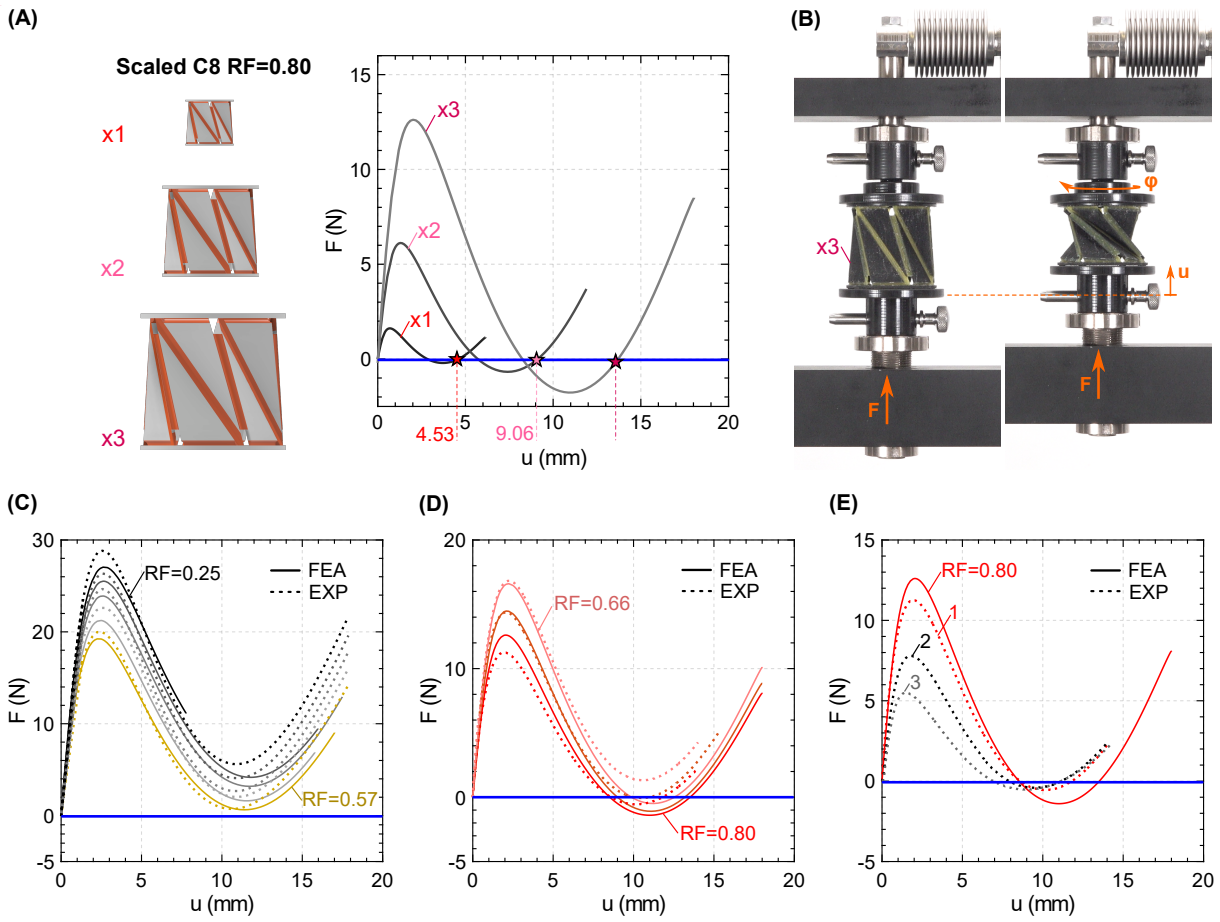

Figure 3: **Scalability and experiments on multi-material 3D printed Kresling cells.** (**A**) Observed scalability in Load paths and in the position of the second local minimum of energy on Kresling cells, at a 1:1 (x1), 2:1 (x2) and 3:1 (x3) scales. (**B**) Experimental Setup for multi-material 3D printed Kresling cells at 3:1 scale, designed to impose a vertical displacement u corresponding to a restoring force F, with free rotation at one end. (**C-E**) Comparison between Numerical and Experimental tests performed on case C8 with: (**C**) $RF = 0.25, 0.33, 0.40, 0.50$ and 0.57. (**D**) $RF = 0.66$, 0.74, and 0.80. (**E**) Effect of the degradation of the rubbery crease cross-sections on the load path after performing three sequential experiments on the same sample (C8, RF=0.80 creases made of DM60).

monostability, denoted as 'Limit Bi' in Fig. 2A. Its experimental load path tends to remain above zero, making it difficult to confirm whether the condition for achieving a second local minimum of energy is truly satisfied, as shown by the corresponding numerical load path. A summary of the experiments, including hands-on experimental validation of bistability, is presented in videos S1 and S2. Furthermore, we observed that sequential compression tests can induce degradation in the rubbery photopolymer, resulting in longitudinal cracks along the creases, particularly in areas with cross-sectional dimensions smaller than 0.6 mm. To investigate this, we performed the compression

experiment three times on the same samples.

Gradual decreases in the load values achieved for sample RF = 0.80 were detected across experimental curves denoted 1, 2, and 3, as shown in Fig. 3E, along with additional details in video S3 and supporting Fig. S24. We determined that approximately 30% and 50% of the load capacity achieved in test 1 was lost after tests 2 and 3, respectively.

2.3 Effects of creases viscosity on bistability

In a second parametric study, we focused on the effects of viscosity on the bistability and stored energy in Kresling cells composed of rubbery creases while preserving the same rigid panels. Specifically, we analyzed the configurations of creases from cases C8 to C11, which led to bistability during the first parametric study described in section 2.1. Those creases were modeled exclusively with the rubbery material DM60, which has a relaxation modulus of G_{60}=0.220 MPa. The selected groups of creases are located within the following geometrical ranges: $0.05 \leq s_i/s \leq 0.41$ and $1.50 \leq w/s \leq 2.00$, as shown in Fig. 4A. We obtained the corresponding numerical load paths and energy landscapes using various rubbery photopolymers characterized by different relaxation moduli and viscosity with respect to DM60, including AG30 (G_∞=0.7G_{60}), DM70 (G_∞=1.4G_{60}), DM85 (G_∞=2.6G_{60}), and DM95 (G_∞=3.9G_{60}), as detailed in Supplementary Text S.2.4. Their viscoelastic properties, such as relaxation modulus ($G(t)$) and Prony parameters (g_i, τ_i), were determined experimentally (see Section S.1.6 of Supplementary Materials and Methods for more details). As a result, Fig. 4A summarizes whether bistability is preserved in the geometrical configurations analyzed under various levels of relaxation modulus and viscosity. In addition, bistability was numerically evaluated over different time scales, considering the initial (τ_i^*), short- (τ), and long-term ($n\tau$) relaxation times exhibited by the visco-hyperelastic materials analyzed, as indicated in Fig. 4B.

Thus, we observed that Kresling cells composed of creases with a lower relaxation modulus, characterized by the softest photopolymers AG30, DM60, and DM70, remained in bistable behavior in the majority of cases and in all the analyzed time scales. Configurations whose reduction factors are in the range within $0.74 \leq RF \leq 0.80$ can also achieve bistability with rubbery materials having an intermediate relaxation modulus, such as that of DM85. However, in cases where geometrical

configurations are at the limit of achieving bistability, which are generated with a reduction factor RF=0.66 and when using DM85, a monostable scenario occurred. On the other hand, we inferred that at the highest relaxation modulus and viscosity, for instance DM95 material, the Kresling cell tends to exhibit monostability in most cases. Consequently, we estimate that as the rubbery material in the creases becomes more highly viscous, with a high relaxation modulus, the load values consistently stay above zero, and the sample tends to return to its initial state, compromising a bistable behavior.

2.4 Experiments on Kresling Cells with variable visco-hyperelastic creases

We selected the configurations of the case C8 RF=0.80 to experimentally validate their bistable behavior previously described in Fig. 4A. For this, we compared their numerical and experimental load paths and stored energy landscapes, as illustrated in Fig 4C. The fabrication of the samples and the experiments were done as detailed in sections 5.4 and 5.5, respectively. We confirmed experimentally that bistability is maintained by Kresling cells made of creases with the less stiff rubbery materials and characterized by lower relaxation moduli, such as AG30, DM60, DM70, and the intermediate, DM85. Similarly, Kresling cells with creases made of DM95, which has the highest relaxation modulus among the analyzed rubbery materials, lost the ability to achieve bistability in practice. Instead, the Kresling cell transitioned to a monostable scenario, where the load values tend to deviate further from intersecting the displacement axis at zero force. Then, a corresponding rise in stored energy is observed without reaching a second local minimum of energy. This occurs despite the fact that the geometrical design favors bistability when using softer materials with lower relaxation moduli. We can attribute this to the fact that the rubbery material DM95 is more likely to exhibit higher viscosity than the other photopolymers and retain stiffness over time, making even the folding of the Kresling cell more difficult. Consequently, we observed that variations in relaxation modulus can aid in tuning the energy landscapes, as well as modifying the geometrical parameters of the creases.

The experiments were conducted similarly to those described in section 2.2 and included hands-on experimental validation of bistability, as shown in video S4. We also detected crack initiation along the creases made of other rubbery materials different from DM60, including

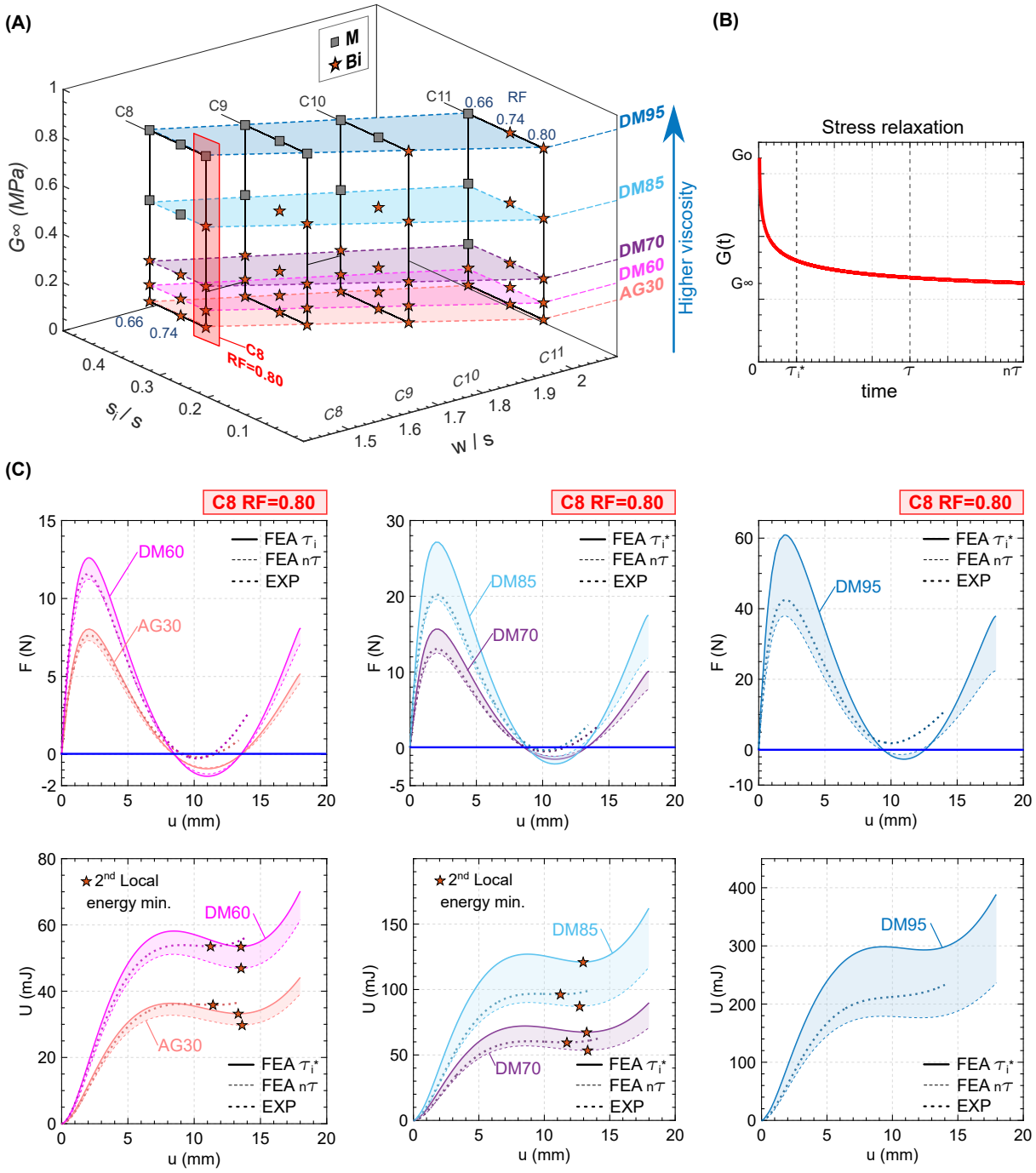

Figure 4: **Visco-hyperelastic effects on the achievement of bistability.** (**A**) Parametric study to assess bistable Kresling cells with creases made of rubbery materials (AG30, DM60, DM70, DM85 and DM95) with different viscoelastic properties in terms of relaxation modulus G_∞, for Cases C8, C9, C10, and C11 designed with reduction factors within the ranges $0.66 \leq RF \leq 0.80$. Results of Kresling cells at 1:1 scale (x1). (B) Experimental relaxation curve. Times τ_i^*, τ and nτ, respectively considered for the numerical analysis of viscosity effects. Experiments were performed at a test speed which correspond to a relaxation time τ_i^*=180 s. (C) Numerical and experimental load paths, along with stored energy landscapes (U). Results for C8 RF=0.80 cells at a 3:1 scale (×3), with rubbery creases exhibiting different relaxation moduli. Filled regions include FEA simulations within the range $\tau_i^* \leq \tau \leq n\tau$.

AG30, DM70, DM85 and DM95, in the tested Kresling cells. This affected the accuracy of the experimental load paths with respect to the corresponding numerical counterparts, as we observed in the experiments shown in Fig. 3D. Likewise, degradation in the creases was noted after testing each sample consecutively three times, representing a technological limitation related to the use of rubbery photopolymers with very small cross-sections (≤0.6 mm), as further detailed in supporting Fig. S33.

2.5 Mono-material cells

In the context of the multi-material 3D printing approach, the compression/expansion process of Kresling cells, as well as the achievement of bistability, becomes feasible by combining the bending of rigid panels and rubbery creases. In the case of using a single material, we propose a strategy in which we segmented the creases and create voids along the full volume of the valleys (V_{vf}), and peaks (V_{pf}), as shown in Fig. 5A and B. This difference in volume contributed to reduce the stiffness of the creases with respect to the panels. Then, the analyzed Kresling cells, denoted as M-1 and M-2, are designed with the geometrical configuration of case C11 RF=0.80. We selected this configuration because it potentially exhibits bistability, independently of the viscoelastic properties of the creases materials, as described in Section 2.3. The variable volume of the valley creases is denoted as V_v. In the M-1 case, where the number of voids along the valleys is zero, and their volume is $V_v = V_{vf}$. In M-2 case, the number of voids along the valleys is 2, and their volume is equal to V_v=3/5 V_{vf}.

In both Kresling cell cases M-1 and M-2, the reduction of the peaks volume was also considered as a minimum fraction of their respective full volume, denoted as V_p=2/7 V_{pf}. The remaining small amount of material that forms the peaks, only contributes to the connection between the panels. Thus, we simplify the analysis by regarding the volume of the valleys V_v with their voids inclusions, as the sole variable of analysis. The load paths and energy landscapes corresponding to M-1 and M-2 cases are shown in Fig. 5A and B. They indicate that both Kresling cells, made completely of rubbery photopolymers such as Origin 402, IP-PDMS, and DM95, exhibited a monostable behavior. In addition to these materials, the use of photopolymers with a stiffness of around 600 MPa, like UTL, suggests that monomaterial Kresling cells can also achieve bistability. This type of photopolymers

are used in micro-printing being characterized by high-flexibility and toughness, suitable for snap-fits or similar fixtures. Additional results with rubbery photopolymers, including DM60, DM70, and DM85, are presented in Supplementary Text S.2.5.

2.6 Programmable Monostable Kresling Assemblies

The variation of geometrical parameters in Kresling cells, such as initial relative angle θ_o and the aspect ratio between the initial height and the polygon's radius h_o/r, can lead to programmable energy absorption levels. We analyzed the following mono-stable Kresling cell configuration: number of polygon's sides n=8, $\theta_o = 45°$, and h_o/r=0.40, determined using the same criteria as the previously analyzed configuration with n=6. Next, 3D parametric Kresling cells were designed and coupled in chiral configurations to form multi-story cylinders with five stories (#$stories$=5). In this analysis, we aimed to explore the crucial role of crease stiffness in the compression/expansion process and storing energy in multi-story and monostable Kresling cells.

These structures were numerically analyzed in Abaqus/CAE standard to determine their load paths and energy landscapes during compression, as detailed in section 5, and were validated experimentally, as described in section 5.5 and video S5. A vertical displacement was applied at the top, while the bottom is fixed, as shown in Fig. 5C. The Kresling multi-story cylinders were designed for fabrication using multi-material 3D printing, with rigid panels (VB), and creases made of softer (DM60) and stiffer (DM95) rubbery materials. Thereafter, we generated three different cases to specifically evaluate the influence of creases with variable stiffness: (i) creases made entirely of the softer rubbery material DM60 across all five stories, (ii) stiffer creases in the even stories (DM60-DM95-DM60-DM95-DM60), and (iii) stiffer creases in the odd stories (DM95-DM60-DM95-DM60-DM95).

During the folding of the multi-story cylinders, the numerical load paths were tracked until the contact between panels started, reaching a displacement in the range of 12 mm $\leq$u$\leq$16 mm. We calculated the stored energy at these points. Using the value from case (i) as a reference, we observed increases of 59.15% and 139.05% with the inclusion of stiffer creases, as seen in cases (ii) and (iii), respectively. Moreover, considering the intermediate stories 2, 3, 4 as points of analysis, we observed that all the stories are folded uniformly in the case (i), where creases are made of

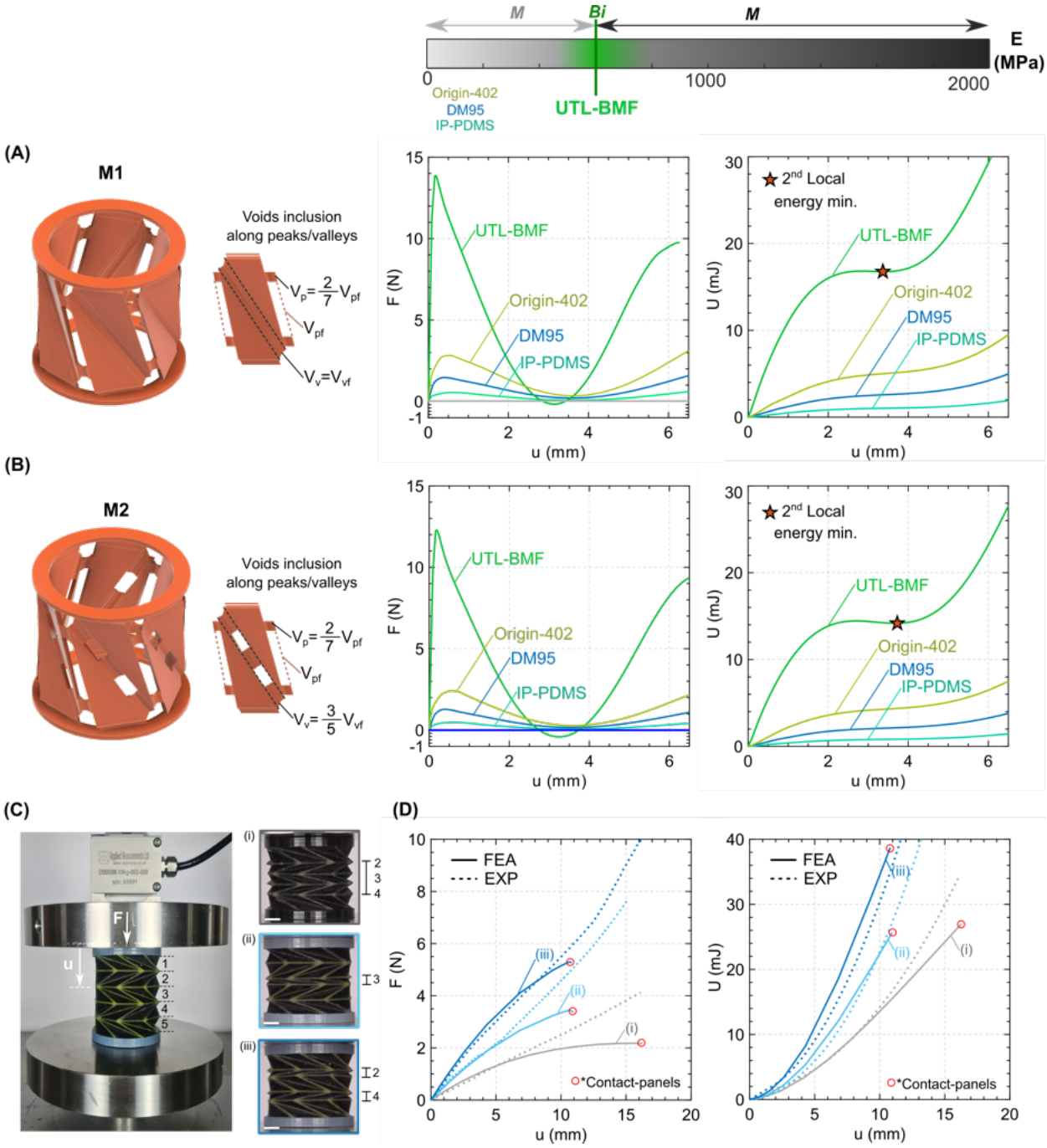

Figure 5: **Load paths and stored energy landscapes of monomaterial Kresling cells and programmable Kresling assemblies.** (**A**) M-1, and (**B**) M-2 cases. Materials with intermediate stiffness tend to achieve bistability (Bi). Results of Kresling cells at 1:1 scale. (**C**) Compression test and folding process of cases (i) All the creases DM60, (ii) Stiffer creases (DM95) in the even stories, and (iii) Stiffer creases (DM95) in the odd stories. The number of folded stories at a displacement u≈ 12mm is indicated. (**D**) Numerical (FEA) and experimental (EXP) results. The numerical simulations stopped at the first contact among panels.

the same material DM60. On the alternating creases stiffness cases, stories with creases made of softer material tended to be folded first than their rigid counterparts. For instance, the odd story 3 (DM60) in case (ii), was folded first than the even stories 2 and 4 made of stiffer material (DM95) and vice-versa in case (iii), as described in Fig. 5D. Hence, we proposed another approach for the programmability of stored energy and to control the localized deformation of specific stories during the folding process of multi-story Kresling structures. Therefore, we aimed to provide design hints for 3D printed structures that could potentially be employed in programmable motion and damping devices.

3 Discussion and Limitations

Starting with a Kresling cell configuration (n=6, h_o/r=1.75, $\theta_o = \pi/6$), along with the proposed gradual reduction of the creases cross sections, we conducted numerical simulations to obtain the corresponding load paths and energy landscapes. Traditional modeling approaches for Kresling structures typically involve thin-shell elements primarily intended for physical prototypes made from paper-based or thin polymer sheets. However, using 3D hybrid-modified elements enabled us to incorporate visco-hyperelastic models, providing a more realistic mechanical response for viscous and nearly incompressible materials, such as the flexible photopolymers used in 3D printing. Under the assumptions of paper-based models, such as constant crease cross-sections and zero viscosity, predictions of mechanical behavior differ when applied to 3D-printed Kresling cells. For example, the design of an intact rubbery crease is more likely to not exhibit the theoretically predicted bistability. For multi-material 3D printing Kresling cells, we established a range of geometrical parameters, including width-to-external thickness ratio w/s, internal thickness s_i, and reduction factor RF, leading to parametric design process to obtain bistable cells. Based on the results of the parametric study, we have confirmed that the geometry of the creases is influential when aiming a specific load path.

Particularly, when the crease width w exceeds a ratio $w/s \geq 1$, the energy landscapes of the multi-material 3D-printed Kresling cells can be significantly controlled by modifying the internal thickness s_i using imposed reduction factors RF, while maintaining the same width w. For example, we demonstrated that the internal thickness s_i is a critical factor in achieving bistability.

Specifically, values in the range $0.30 \leq s_i/s \leq 0.05$ generated by reduction factors RF between 0.74 and 0.80, ensure bistability while reducing the cross-section relative to the intact cross-section by an approximate ratio of $0.60 \geq \tilde{A}/A \geq 0.50$. Consequently, the rotational stiffness of the reduced creases relative to the intact crease decreases to a range of $0.20 \geq \tilde{K}/K \geq 0.10$, ensuring the flexibility required for bistable Kresling cells. In contrast, Kresling cells generated with RF values below 0.66 tended toward monostable behavior in practice. In these cases, we observed that the experimental load path remains above zero, which differs from the numerical counterpart's prediction. Furthermore, we noted that, after applying a compressive load to the Kresling cell, it returned to its initial configuration more quickly, as shown in video S2. Thus, we confirmed that bistability was not achieved in practice.

For this reason, we established a reduction factor RF=0.66 as a geometric limit for determining bistability. This discrepancy may be due to slight increases in cross-sectional dimensions resulting from printing accuracy, potentially leading to a greater thickness, s_i, and closer to that of the next case with $RF = 0.57$. Although taking measurements along the crease length is complicated due to the complex geometry of the Kresling cell, the fact of having such a greater crease thickness is confirmed by the microscopic measurements we performed along an horizontal slicing plane that cuts the Kresling cell at the mid-height.

We numerically and experimentally determined how the achieved bistability is affected by the visco-hyperelastic behavior characteristic of rubbery 3D printing materials. For example, in the particular case of C8 Kresling cells with creases made of rubbers with lower (AG30, DM60, DM70) and intermediate (DM85) relaxation moduli preserved bistability. Considering DM60 relaxation modulus as G_∞=1.0G_{60}, we have AG30 (G_∞=0.7G_{60}), DM70 (G_∞=1.4G_{60}) and DM85 (G_∞=2.6G_{60}). In contrast, when the creases were characterized by a higher relaxation modulus such as the case of DM95 material (3.9 G_{60}), the Kresling cells transitioned towards a monostable behavior. Our numerical simulations also predicted that bistability is preserved over different time scales corresponding to the initial (τ_i^*), short- (τ), and long-term (nτ) relaxation times. Since numerical simulations showed that the energy landscapes did not vary significantly for relaxation times higher than τ_i, we decided to perform them a test speed which correspond to a relaxation time τ_i^*=180 s. This choice allows for efficient characterization while avoiding unnecessary long-term testing, as the observed bistability remains over time. When comparing visco-hyperelastic creases made of

different rubbery materials, the viscoelastic component, specifically the difference in relaxation modulus, appeared to have a greater effect on achieving bistability than the time scale of analysis. Furthermore, these results suggest that specific geometrical parameters leading to creases with smaller cross-section thickness s_i, such as those generated with a reduction factor RF=0.80, play a more significant role in the achievement bistability and programming the energy landscape, counteracting the inherent viscoelastic effects.

In the case of a monomaterial approach, the geometrical designs with the narrowest creases (especially those generated with a reduction factor RF=0.80) were selected, as they provide the highest rotational stiffness reduction $\tilde{K}/K \approx 0.10$ and flexibility. Our design strategy was based on variations in stiffness along the creases, achieved through the inclusion of voids in the peaks and valleys, which facilitated the compression and expansion processes of the Kresling cell. Regardless of the material used, we also evidenced that decreasing the volumes of the creases by including more voids along the valleys, can modify the energy landscapes resulting in lower stored energy values. These differences can be observed by comparing the energy landscapes corresponding to the cases M-1 in Fig. 5A and M-2 in Fig. 5B. For example, considering both cases made of UTL resin, M-1 and M-2, their achieved total stored energy values were U=32 mJ and U=26 mJ, respectively. This means that the inclusion of two voids along the valleys, corresponding to the fraction V_v=3/5 Vvf, can result in a decrease of 18.75% in the total stored energy.

Since rubbery photopolymers exhibit low tensile instantaneous relaxation moduli between 1.0MPa $\leq E_o \leq$ 10MPa, the effect of their visco-hyperlastic properties on preserving bistability is almost not mitigated without the interaction with stiffer panels. On the other hand, very rigid photopolymers led to earlier failure, tending to present a brittle behavior, and the folding mechanism is limited. For this reason, materials with intermediate stiffness values can be an alternative for achieving bistability. We have confirmed this fact by analyzing a Kresling cell composed of UTL resin (*45*), with a Young's Modulus around E $\approx$ 600 MPa, where bistability was observed. Therefore, it opens the possibility of miniaturizing bistable Kresling cells using a single material. These configurations can be used to fabricate downscaled Kresling cells, even at the micro-scale, thereby overcoming the dimensional limitations of traditional 3D printing technologies.

In addition, we investigated the role of creases in monostable Kresling assemblies. Using a multi-material printing approach, we evaluated and fabricated Kresling structures with variable

stiffness assigned to the creases in even and odd stories. For instance, during the folding process, deformation occurs first in the stories with softer creases, such as those made of DM60, and later in the stiffer ones made of DM95. This approach facilitates the control and programming of the energy landscape. Notably, we also achieved an increase of up to approximately 140% in stored energy by including stiffer creases.

3.1 Limitations

We validated the numerical predictions experimentally, considering manufacturing limitations to prevent defects at the time of fabricating 3D-printed parts. Dimensional constraints due to technological limitations restrict the size of 3D-printed multi-material Kresling cells that can be tested. In the case of the PolyJet technique, load-bearing elements with cross-sections smaller than 0.6 mm tend not to cure well and may exhibit defects during the photopolymerization and layer deposition processes. However, considering cross-sections above 1.0 mm helps reduce defects and they remain intact during post-processing operations (*42*). During subsequent compression tests on Kresling cell samples, we observed a reduction in stiffness and peak loads of 30% after the second test and 50% after the third test. This can be attributed to crack initiation in thin creases made of rubbery photopolymers. This suggests material degradation in thin cross-sections made of the rubbery material after repeated loading cycles, potentially compromising its suitability for long-term applications. This observation highlights potential limitations in the reliability of this technique for experiments on multi-material Kresling cells, indicating potential long-term durability concerns. However, fabricating on a larger scale could be an option to overcome these manufacturing dimensional limitations, although it might result in higher material costs and longer working times.

4 Concluding remarks

We proposed alternatives to explore the untapped engineering potential of Kresling origami beyond traditional paper models. The advent of 3D printing has enabled the creation of complex multistable structures with programmable energy landscapes inspired by Kresling patterns. However, this approach also faces unique challenges related to manufacturing and material limitations, especially at small scales and when addressing the visco-hyperelastic nature of photopolymers.

Our study emphasized the critical role of crease design in achieving reliable multistability in Kresling cells, highlighting overlooked parameters such as crease geometry and viscosity. By modifying the crease cross-section, we obtained diverse energy landscapes ranging from bistability, to monostability.

For instance, reducing the crease internal thickness s_i, through proposed reduction factors RF, by over 50% of the intact cross-section facilitated bistability, as confirmed by experimental validation that accounted for manufacturing limitations and scalability considerations. Rubbery creases with the highest relaxation modulus ($G_\infty \approx 0.855$MPa) compromised bistability, while those with lower relaxation moduli preserved it. In addition, the observed bistability remained over different time scales, including the initial, short- and long-term relaxation times regions. Consequently, we found that the difference in relaxation modulus had a greater impact on bistability than the time scale of analysis. Our results further indicate that the most significant changes in the energy landscape were primarily attributed to modifications in the geometrical parameters of the crease cross-section, which contributed to limiting the influence of visco-hyperelastic effects, especially in the configurations with the smallest cross-sections generated with a reduction factor RF=0.80.

Considering a monomaterial approach, stiffness variations achieved through voids in crease geometry improved the compression and expansion of Kresling cells and allowed energy storage to be tailored. Materials with intermediate stiffness (E ≈600MPa) were identified as optimal for foldable, bistable designs, particularly oriented to micro-fabrication.

Moreover, we explored the role of creases in monostable Kresling assemblies by varying their stiffness. This allowed us to control the deformation of specific stories, enabling programmable energy landscapes and adjustable energy storage based on the inclusion of softer or stiffer creases.

In summary, our findings address key 3D printing challenges and offer potential for applications such as customized and scalable energy absorbers, actuators, and delivery robots that rely on compact and programmable energy landscapes. These configurations advance our understanding of Kresling-origami-inspired structures while also paving the way for future research.

5 Materials and Methods

5.1 Initial Sizing of Kresling cells

The geometrical parameters that define the initial sizing configuration of the Kresling cells were estimated using a five-parameters model (*26*), as further detailed in section S.1.1 of Supplementary Materials and Methods. Considering a Kresling cylinder defined by top and bottom polygons with a number of sides n=6, under an axial displacement u, the total elastic stored energy of the creases U can be defined by the sum of the deformation strain U_b and the rotational springs U_s contribution of the peak and valley creases, by using the expressions:

$$U_b = \frac{1}{2}nK_{sb}(b - b_o)^2 + \frac{1}{2}nK_{sc}(c - c_o)^2, \tag{1}$$

$$U_s = \frac{1}{2}nK_a(\delta_a - \delta_{ao})^2 + \frac{1}{2}nK_b(\delta_b - \delta_{bo})^2 + \frac{1}{2}nK_c(\delta_c - \delta_{co})^2, \tag{2}$$

$$U = U_b + U_s \tag{3}$$

Here, K_{sb} and K_{sc} represent the stretching stiffness of the creases, while b and c denote the final lengths during the compression/expansion corresponding to the peaks and valleys, respectively. The original peak and valley lengths are denoted as b_o and c_o, respectively. The terms K_a, K_b, and K_c represent the rotational stiffness of the creases. The dihedral angles in the original configuration are $\delta_{ao}, \delta_{bo}, \delta_{co}$, while those in the folded configuration are $\delta_a, \delta_b, \delta_c$, corresponding to their respective creases. An iterative process was performed applying Eq.3 to select the initial sizing configuration that theoretically leads to a second local minimum of energy when $\delta U/\delta u$=0 (*46, 47*).

5.2 Parametric Design

The cylindrical Kresling cells were designed as solid bodies in Autodesk Inventor in 1:1 scale (x1), following the initial sizing configuration: polygons with n=6 sides, rotating at an initial angle $\theta_o = \pi/6$ with respect to each other, and an aspect ratio h_o/r=1.75. The panels were modeled with a small thickness value with respect to the initial height (0.04 $h_o \leq \bar{s} \leq$ 0.08 h_o). In addition, rings were included at the top and bottom of the cylinders to ensure a uniform rotation of the upper and

lower polygons. Moreover, we created a small gap at the top and bottom intersections of the creases with the rings to prevent stress concentrations, as illustrated in the 3D Kresling cell renders from Fig. 3A.

In the Multi-material approach, the creases of the Kresling cells were parametrically designed with dimensional and geometrical variations. The dimensionless ratio w/s represents the creases width, w, variation relative to its thickness, s, ranging within $0.50 \leq w/s \leq 2.00$, and being gradually reduced considering the reduction factors $0.25 \leq RF \leq 0.80$. The generated configurations were obtained by combining the mentioned parameters and they are detailed in section S.1.2 of Supplementary Materials and Methods.

In the Mono-material approach, the Kresling cells were similarly designed following the initial sizing configuration and incorporating the creases design from the case C11 RF=0.80. The latter represents the most flexible crease with the lowest rotational stiffness ($\tilde{K}$= 1.26x10^{-5} N.mm/rad). The voids inclusions along the peaks and valleys, corresponded to a fraction of the total volume of their respective full creases, as explained in section 2.5. Thereby, multiple Kresling cell configurations for Multi-material and mono material approaches were exported as *.step and *.x_b Parasolid files, for the respective numerical simulations and 3D printing, respectively.

5.3 Numerical simulations and constitutive models

Quasi-static non-linear analyses were carried out in Abaqus/CAE Standard meshing the systems with quadratic tetrahedron C3D10MH elements due to the complexity of the geometry. This type of mesh contains 10 node quadratic tetrahedron with hybrid modified constant pressure elements. This choice was dictated by the hyperelastic nature of the rubbery material which is nearly incompressible. Tie constraints were assigned to the panels, creases, top and bottom ring surfaces to create a uniform contact among them. The defined boundary conditions at the bottom of the cylinder constrained all the displacements and the rotations. An imposed vertical displacement close to the one third of the initial height ($\approx 1/3\ h_o$) was applied at the top.

Simultaneously, the rotation of the upper part was also released to simulate the natural twisted motion, characteristic of the Kresling patterns along with a compressive force. Furthermore, we remark that the quasi-static simulations were conducted using a VISCO step to capture the time-

dependent behavior of the visco-hyperelastic elements. The simulations proceeded until the target displacement was reached, ensuring that while the panels made initial contact during the folding process, overlapping was prevented. Further details are explained in section S.1.3 of Supplementary Materials and Methods. Moreover, we incorporated calibrated material models obtained from their respective material characterization tests, as described in section S.1.5 of Supplementary Materials and Methods. The components made of rigid materials, such as the panels and rings, were modeled with an elasto-plastic behavior. In contrast, flexible photopolymers were assigned to the creases, being initially characterized by a Neo-Hookean strain potential energy function described as follows:

$$U_N = C_{10}(\overline{I_1} - 3) \tag{4}$$

where C_{10}=G_o/2, being G_o the instantaneous shear modulus and $\overline{I_1}$ is the first stretch invariant. This hyperelastic model assumes an almost incompressible material and was fitted to experimental data to find the C_{10} coefficients, which define the rate-independent behavior (*48*). Subsequently, the viscoelastic effects of the rubbery materials were then incorporated into the hyperelastic model. The Prony parameters dimensionless weight g_i and relaxation time τ_i characterize the time-dependent behavior associated with viscosity (*49*). They were determined by a non-linear regression analysis by fitting them to the relaxation test data, as detailed in section S.1.6 of Supplementary Materials and Methods. We then applied the obtained Prony parameters to the constants within the strain energy function $U_N(t)$, which is defined by the instantaneous constant C_{10}^o, and the visco-hyperelastic relaxation function can be expressed as follows:

$$U_N(t) = C_{10}^o \left(1 - \sum_{i=1}^{N} g_i(1 - e^{-t/\tau_i})\right) \tag{5}$$

In the context of Polyjet photopolymers, the selected rigid material for the panels in all the numerical simulations of multi-material cases was VeroBlack (VB). Regarding the flexible creases, the rubbery digital material DM60 was used for the first parametric study (section 2.1). In subsequent analyses, we included additional rubbery photopolymers with different relaxation moduli and viscosity than DM60, such as Agilus30 (AG30) and digital materials DM70, DM85, and DM95, to evaluate and predict the effects of viscosity on bistability (section 2.3). The duration of each numerical simulation using the VISCO step, was set equal to the initial, short-term and long-term relaxation times exhibited by the different rubbery materials, based on their relaxation times τ_i from

the Prony series. For the mono-material approach, flexible photopolymers used in other 3D printing techniques were also considered, including Origin 402 (Direct Light Processing), IP-PDMS and UTL-BMF (Two-photon polymerization for micro-fabrication).

5.4 Fabrication of Multi-material Kresling cells

The Kresling cell samples were fabricated following the framework of Polyjet multi-material technique. It is important to remark that cross-sections of structural elements lower than 1.0 mm demand special attention during the Polyjet process. They are prone to exhibit defects and demand extremely careful post-processing operations. For this reason, the printed Kresling cells were scaled three times to make the printing feasible, maintaining the ratios and proportions previously detailed in the parametric design section 5.2, video S6 and section S.1.2 of Supplementary Materials and Methods. Based on the materials we used in the numerical simulations, the panels were fabricated with VeroBlack (VB). For the creases, the following flexible materials were employed in the different Kresling cells: AG30, DM60, DM70, DM85 and DM95.

The 3D CAD models were generated in Autodesk Inventor, to be subsequently printed in a Stratasys J750 printer series. The selected printing setting was High-Mix mode with a layer resolution thickness of 27 microns and glossy surface finishing. The majority of the supports grids made of SUP706B material surrounding the printed Kresling cells were manually removed, and briefly rinsed in water for less than five minutes. A prolonged contact between small elements or multi-material interfaces, lower than 1.0 mm cross-section, with water or alkaline solutions lead to a premature breakage and detachment. Further details on the fabrication of 3D printed Kresling cells protocol are presented in section S.1.7 of Supplementary Materials and Methods.

5.5 Experimental validation

A series of quasi-static experiments were carried on the 3D printed Kresling cells to validate the numerical simulations results. A compression load was applied at the top with an imposed displacement of approximately $u \approx 1/3\ h_o$. The experimental setup, described detail in section S.1.8 - Fig. S10 of Supplementary Materials and Methods, consists on a fixture that resembles free rotation assigned to the top of the sample, with a fixed bottom fixture to prevent displacements

and rotations. Thus, replicating the natural twist under compression inherent in Kresling patterns kinematics (*26*). The connections between the sample and the setup were implemented in two different systems: (i) A female-male pinned system, and (ii) Use of magnets to prevent the sliding of the samples. The cross-head testing speed was 0.1 mm/sec, which can be considered sufficiently slow to capture viscosity effect (relaxation time $\tau_i^* = 180$ s), as well as the most representative bistable behavior according to numerical predictions across different time scales.

5.6 Microscopic characterization of 3D printed creases

The real dimensions of the 3D printed samples were determined via a stereo microscope (Nikon SMZ800) equipped with an ED Plan 1.5x lens and with a DS-Ri2 camera. The analyzed creases belong to the configurations presented in case C8 with gradual reductions between $0.25 \leq RF \leq 0.80$. We compared the mean values of the real measurements of the 3D printed Kresling cells, versus the exact measurements of the CAD models, as detailed in section S.1.10 of Supplementary Materials and Methods. Thus, we determined the mean percentage error, M_{PE} (%) between the dimensions from the tested samples and those used in the numerical simulations. Hence, this estimated error was incorporated to update the analyzed geometrical configurations and considering the loss of dimensional accuracy attributed to the Polyjet printing process.

References and Notes

1. D. Misseroni, *et al.*, Origami engineering. *Nature Reviews Methods Primers* **4** (1), 40 (2024).

2. J. Kaufmann, P. Bhovad, S. Li, Harnessing the multistability of kresling origami for reconfigurable articulation in soft robotic arms. *Soft Robotics* **9** (2), 212–223 (2022).

3. P. Bhovad, J. Kaufmann, S. Li, Peristaltic locomotion without digital controllers: Exploiting multi-stability in origami to coordinate robotic motion. *Extreme Mechanics Letters* **32**, 100552 (2019).

4. Q. Ze, *et al.*, Soft robotic origami crawler. *Science Advances* **8** (13), eabm7834 (2022).

5. L. S. Novelino, Q. Ze, S. Wu, G. H. Paulino, R. Zhao, Untethered control of functional origami microrobots with distributed actuation. *Proceedings of the National Academy of Sciences* **117** (39), 24096–24101 (2020).

6. S. Wu, *et al.*, Stretchable origami robotic arm with omnidirectional bending and twisting. *Proceedings of the National Academy of Sciences* **118** (36), e2110023118 (2021).

7. X. Wang, *et al.*, Multi-triangles cylindrical origami and inspired metamaterials with tunable stiffness and stretchable robotic arm. *PNAS Nexus* **2** (4), pgad098 (2023).

8. S. Wu, T. Zhao, Y. Zhu, G. H. Paulino, Modular multi-degree-of-freedom soft origami robots with reprogrammable electrothermal actuation. *Proceedings of the National Academy of Sciences* **121** (20), e2322625121 (2024).

9. Y. Yao, G. Li, X. Ning, Origami electronic membranes as highly shape-morphable mechanical and environmental sensing systems. *Extreme Mechanics Letters* **73**, 102264 (2024).

10. H. Yasuda, *et al.*, Origami-based impact mitigation via rarefaction solitary wave creation. *Science advances* **5** (5), eaau2835 (2019).

11. J. Li, Y. Chen, X. Feng, J. Feng, P. Sareh, Computational modeling and energy absorption behavior of thin-walled tubes with the Kresling origami pattern. *Journal of the International Association for Shell and Spatial Structures* **62** (2), 71–81 (2021).

12. J. Cai, X. Deng, Y. Zhang, J. Feng, Y. Zhou, Folding behavior of a foldable prismatic mast with kresling origami pattern. *Journal of Mechanisms and Robotics* **8** (3), 031004 (2016).

13. H. Yang, *et al.*, 3D-printable Kresling-embedded honeycomb metamaterials with optimized energy absorption capability. *Smart Materials and Structures* **33** (12), 125008 (2024).

14. Z. Zhai, Y. Wang, H. Jiang, Origami-inspired, on-demand deployable and collapsible mechanical metamaterials with tunable stiffness. *Proceedings of the National Academy of Sciences* **115** (9), 2032–2037 (2018).

15. V. Agarwal, K. Wang, On the nonlinear dynamics of a Kresling-pattern origami under harmonic force excitation. *Extreme Mechanics Letters* **52**, 101653 (2022).

16. S. Li, Y. Miyazawa, K. Yamaguchi, P. G. Kevrekidis, J. Yang, Geometry-informed dynamic mode decomposition in Kresling origami dynamics. *Extreme Mechanics Letters* **64**, 102082 (2023).

17. Y. Wang, X. Zhang, S. Zhu, Highly intensive and controllable supratransmission in a Kresling-origami metastructure. *Extreme Mechanics Letters* **59**, 101964 (2023).

18. Z.-L. Xu, D.-F. Wang, T. Tachi, K.-C. Chuang, An origami longitudinal–torsional wave converter. *Extreme Mechanics Letters* **51**, 101570 (2022).

19. B. Kresling, Natural twist buckling in shells: from the hawkmoth's bellows to the deployable Kresling-pattern and cylindrical Miura-ori, in *Proceedings of the 6th International Conference on Computation of Shell and Spatial Structures IASS-IACM* (2008), p. 4.

20. B. Kresling, Folded tubes as compared to kikko ('tortoise-shell55) bamboo, in *Origami* (Barnes Noble), p. 197 (2002).

21. Q. Zhang, J. Cai, M. Li, J. Feng, Bistable behaviour of a deployable cylinder with Kresling pattern, in *Proceedings of the 7th International Meeting on Origami in Science, Mathematics and Education (7OSME), Oxford, UK* (2018), pp. 4–7.

22. S. V. Georgakopoulos, *et al.*, Origami antennas. *IEEE Open Journal of Antennas and Propagation* **2**, 1020–1043 (2021).

23. X. Liu, S. Yao, S. V. Georgakopoulos, Mode reconfigurable bistable spiral antenna based on kresling origami, in *2017 IEEE International Symposium on Antennas and Propagation & USNC/URSI National Radio Science Meeting* (IEEE) (2017), pp. 413–414.

24. K. Liu, G. Paulino, Nonlinear mechanics of non-rigid origami: an efficient computational approach. *Proceedings of the Royal Society A: Mathematical, Physical and Engineering Sciences* **473** (2206), 20170348 (2017).

25. Z. Li, N. Kidambi, L. Wang, K.-W. Wang, Uncovering rotational multifunctionalities of coupled Kresling modular structures. *Extreme Mechanics Letters* **39**, 100795 (2020).

26. S. Zang, D. Misseroni, T. Zhao, G. H. Paulino, Kresling origami mechanics explained: Experiments and theory. *Journal of the Mechanics and Physics of Solids* p. 105630 (2024).

27. X. Wang, H. Qu, S. Guo, Tristable property and the high stiffness analysis of Kresling pattern origami. *International Journal of Mechanical Sciences* **256**, 108515 (2023).

28. D. Dureisseix, An overview of mechanisms and patterns with origami. *International Journal of Space Structures* **27** (1), 1–14 (2012).

29. A. S. Dalaq, M. F. Daqaq, Experimentally-validated computational modeling and characterization of the quasi-static behavior of functional 3D-printed origami-inspired springs. *Materials & Design* **216**, 110541 (2022).

30. A. S. Dalaq, S. Khazaaleh, M. F. Daqaq, An origami-inspired design of highly efficient cellular cushion materials. *Applied Materials Today* **32**, 101835 (2023).

31. R. Masana, M. F. Daqaq, Quasi-static behavior of a pair of serially-connected Kresling Origami springs. *International Journal of Solids and Structures* **298**, 112877 (2024).

32. Q. Liu, *et al.*, Stiffness-Tunable Origami Structures via Multimaterial Three-Dimensional Printing. *Acta Mechanica Solida Sinica* pp. 1–12 (2023).

33. D. Melancon, A. E. Forte, L. M. Kamp, B. Gorissen, K. Bertoldi, Inflatable origami: Multimodal deformation via multistability. *Advanced Functional Materials* **32** (35), 2201891 (2022).

34. H. Ye, *et al.*, Multimaterial 3D printed self-locking thick-panel origami metamaterials. *Nature communications* **14** (1), 1607 (2023).

35. Y. X. Mak, A. Dijkshoorn, M. Abayazid, Design Methodology for a 3D Printable Multi-Degree of Freedom Soft Actuator Using Geometric Origami Patterns. *Advanced Intelligent Systems* **6** (6), 2300666 (2024).

36. C. Zhang, *et al.*, Plug & play origami modules with all-purpose deformation modes. *Nature Communications* **14** (1), 4329 (2023).

37. M. Moshtaghzadeh, E. Izadpanahi, P. Mardanpour, Prediction of fatigue life of a flexible foldable origami antenna with Kresling pattern. *Engineering Structures* **251**, 113399 (2022).

38. H. Cho, *et al.*, Engineering the mechanics of heterogeneous soft crystals. *Advanced Functional Materials* **26** (38), 6938–6949 (2016).

39. F. F. Abayazid, M. Ghajari, Material characterisation of additively manufactured elastomers at different strain rates and build orientations. *Additive Manufacturing* **33**, 101160 (2020).

40. Ultimaker, How to design for FFF 3D printing, Ultimaker, https://ultimaker.com/wp-content/uploads/2024/06/How-to-design-for-FFF-1.pdf.

41. Stratasys, Four Key Factors for a Balanced Design, Stratasys, https://www.stratasys.com/en/stratasysdirect/resources/articles/3d-printing-balanced-design-key-factors/.

42. S. Mora, N. M. Pugno, D. Misseroni, 3D printed architected lattice structures by material jetting. *Materials Today* (2022).

43. Y. Chi, *et al.*, Bistable and multistable actuators for soft robots: Structures, materials, and functionalities. *Advanced Materials* **34** (19), 2110384 (2022).

44. D. Bigoni, *Nonlinear solid mechanics: bifurcation theory and material instability* (Cambridge University Press) (2012).

45. BMF, UTL resin datasheet, BMF, https://ultimaker.com/wp-content/uploads/2024/06/How-to-design-for-FFF-1.pdf.

46. R. Masana, M. F. Daqaq, Equilibria and bifurcations of a foldable paper-based spring inspired by Kresling-pattern origami. *Physical Review E* **100** (6), 063001 (2019).

47. H. Yasuda, T. Tachi, M. Lee, J. Yang, Origami-based tunable truss structures for non-volatile mechanical memory operation. *Nature Communications* **8** (1), 1–7 (2017).

48. Dassault Systèmes, *Abaqus Documentation, Hyperelastic behavior of rubberlike materials* (2010), version 6.10.

49. C. Tzikang, *Determining a Prony series for a viscoelastic material from time varying strain data*, Tech. rep., NASA (2000).

Acknowledgments

Funding: SM co-funded by the European Union under Horizon Europe Programme, project 'SUBBIMATT - Sustainable, Biobased and Bio-Inspired Materials for Smart Technical Textiles', HE Grant Agreement 101129911 — SUBBIMATT. NMP is supported by the European Union BOHEME project, H2020 FET Open programme, GA 863179. DM is funded by the European Union, project 'S-FOAM – Self-Foldable Origami-Architected Metamaterials' , ERC grant HE GA 101086644 S-FOAM. View and opinions expressed are those of the author(s) only and do not necessarily reflect those of the European Union or the European Research Council Executive Agency. Neither the European Union nor the granting authority can be held responsible for them.

Author contributions: Conceptualization: S.M, D.M. Methodology: S.M, D.M. Data acquisition & Formal analysis: S.M. Numerical simulations: S.M. Experiments & prototyping: S.M, D.M. Supervision: D.M., N.M.P. Writing—original draft: S.M, D.M. Writing—review & editing: S.M, D.M, N.M.P. Funding acquisition: D.M, N.M.P.

Competing interests: There are no competing interests to declare.

Data and materials availability: All the data, physical samples, simulation outputs have been obtain at the Laboratory of Design of Metamaterials and Structures, DICAM, University of Trento. The primary raw data from the experiments and simulations are available in the open-access repository on Zenodo: https://doi.org/10.5281/zenodo.15118000 or upon request via email to the corresponding author.

Supplementary materials

Materials and Methods

Supplementary Text

Figs. S1 to S34

Tables S1 to S2

References *(7-49)*

Video S1 to S6

Supplementary Materials for

Programming the Energy Landscape of 3D-Printed Kresling Origami via Crease Geometry and Viscosity

Samantha Mora[†], Nicola M. Pugno[†], Diego Misseroni[*†]

[*]Corresponding author. Email: diego.misseroni@unitn.it

[†]These authors contributed equally to this work.

This PDF file includes:

Materials and Methods

Supplementary Text

Figures S1 to S34

Tables S1 to S2

Captions for Videos S1 to S6

Other Supplementary Materials for this manuscript:

Videos S1 to S6

S.1 Materials and Methods

S.1.1 Initial sizing of Kresling cells

We determined an initial geometrical configuration of the Kresling cell that could potentially exhibit bistability. The approach relied on a five-parameters model incorporating the elastic deformation of stretchable mountain and valley creases (*14, 46*) with their rotational behavior (*26*). As illustrated in Fig. S1A, we first considered the following initial geometrical parameters: an initial height denoted by h_o, upper and lower polygons with n sides circumscribed within a radius r, an initial relative angle θ_o between these polygons. The original lengths of the creases, denoted by a_o (side of the polygon), b_o (peaks), and c_o (valleys), and their corresponding dihedral angles δ_{ao}, δ_{bo}, and δ_{co}, can be calculated using the expressions:

$$a_o = 2r \sin\left(\frac{\pi}{n}\right) \tag{S1}$$

$$b_o = \sqrt{4r^2 \sin^2\left(\frac{\theta_o}{2}\right) + h_o^2} \tag{S2}$$

$$c_o = \sqrt{4r^2 \sin^2\left(\frac{\theta_o + \frac{2\pi}{n}}{2}\right) + h_o^2} \tag{S3}$$

$$\delta_{ao} = \arctan \frac{h_o}{2r \sin\left(\frac{\theta_o}{2}\right) \sin\left(\frac{\theta_o}{2} + \frac{\pi}{n}\right)} \tag{S4}$$

$$\delta_{bo} = \pi - \arccos \frac{h_o^2 \cos\left(\theta_o + \frac{2\pi}{n}\right) - r^2 \left[\cos\left(\theta_o + \frac{\pi}{n}\right) - \cos\left(\frac{\pi}{n}\right)\right]^2}{h_o^2 + r^2 \left[\cos\left(\theta_o + \frac{\pi}{n}\right) - \cos\left(\frac{\pi}{n}\right)\right]^2} \tag{S5}$$

$$\delta_{co} = \pi - \arccos \frac{h_o^2 \cos\left(\theta_o\right) - r^2 \left[\cos\left(\theta_o + \frac{\pi}{n}\right) - \cos\left(\frac{\pi}{n}\right)\right]^2}{h_o^2 + r^2 \left[\cos\left(\theta_o + \frac{\pi}{n}\right) - \cos\left(\frac{\pi}{n}\right)\right]^2} \tag{S6}$$

When the compressive load F is applied to the top of the Kresling cell, it produces an axial displacement u and a twisting rotation ϕ between the upper and lower polygons, while the final height of the Kresling cell becomes h, as shown in Fig. S1A. Furthermore, the length of the crease

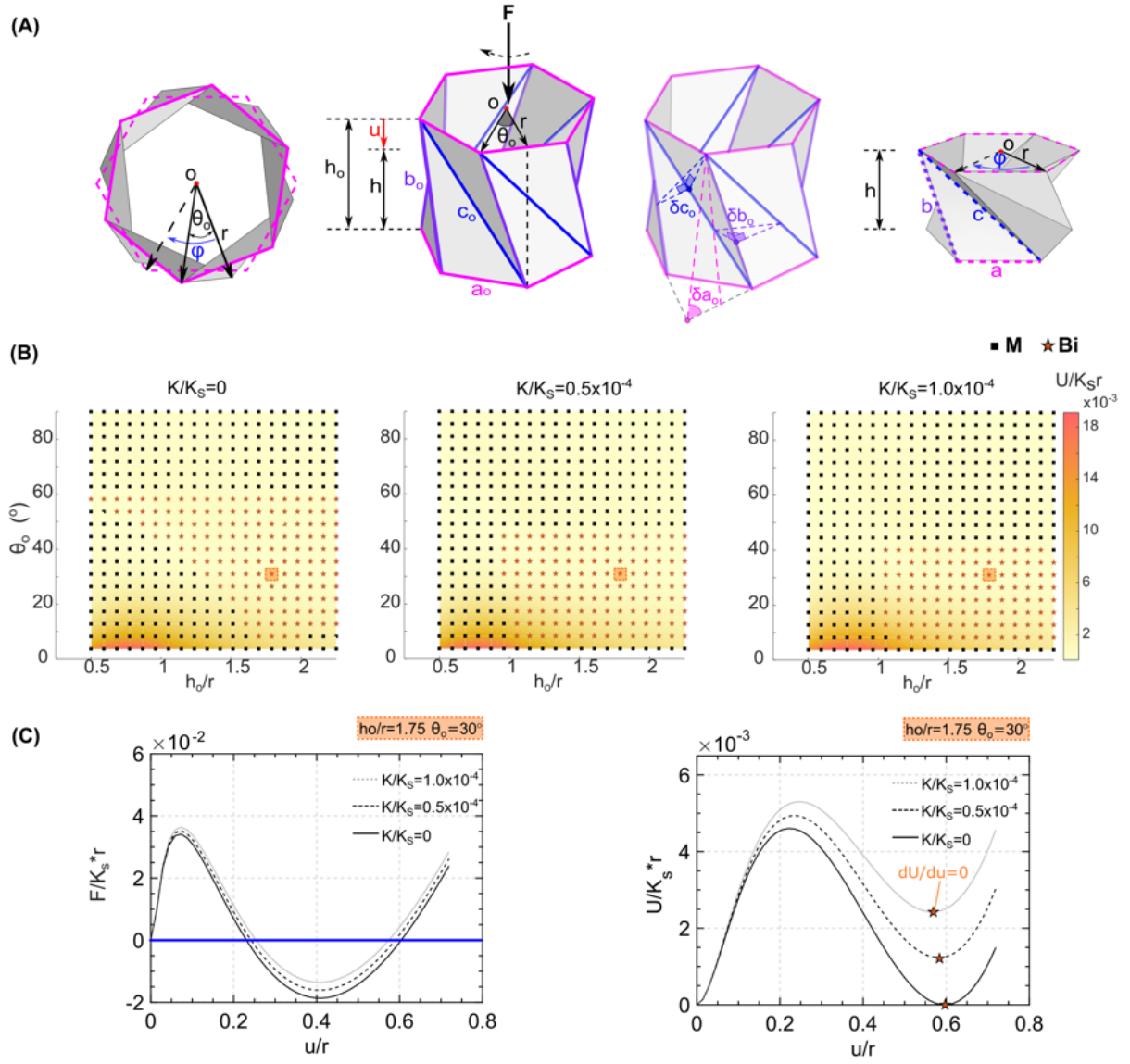

Figure S1: **Initial sizing of the Kresling cell. (A)** Kresling cell geometrical parameters during compression/expansion process. **(B)** Initial assessment of monostable (M) and Bistable (Bi) configurations through a five-parameters model, by considering their initial relative angle θ_o and aspect ratio h_o/r and rotational versus stretching stiffness ratio K/K_s. (C) Normalized Force (F) and Energy (U) plots versus normalized displacement u/r of the configuration $\theta_o = 30^o$ and h_o/r=1.75.

corresponding to the side length of the polygon a_o remains constant with negligible deformation, as it remains circumscribed within the polygon's circle of radius r. At this stage, it can be considered that $a = a_o$, and the lengths of the creases corresponding to the peaks, b, and valleys, c with their respective dihedral angles δ_a, δ_b, and δ_c are defined as follows:

$$b = \sqrt{4r^2 \sin^2\left(\frac{\phi}{2}\right) + (h_o - u)^2} \tag{S7}$$

$$c = \sqrt{4r^2 \sin^2\left(\frac{\phi + \frac{2\pi}{n}}{2}\right) + (h_o - u)^2} \tag{S8}$$

$$\delta_a = \arctan \frac{h_o - u}{2r \sin\left(\frac{\phi}{2}\right) \sin\left(\frac{\phi}{2} + \frac{\pi}{n}\right)} \tag{S9}$$

$$\delta_b = \pi - \arccos \frac{(h_o - u)^2 \cos\left(\phi + \frac{2\pi}{n}\right) - r^2 \left[\cos\left(\phi + \frac{\pi}{n}\right) - \cos\left(\frac{\pi}{n}\right)\right]^2}{(h_o - u)^2 + r^2 \left[\cos\left(\phi + \frac{\pi}{n}\right) - \cos\left(\frac{\pi}{n}\right)\right]^2} \tag{S10}$$

$$\delta_c = \pi - \arccos \frac{(h_o - u)^2 \cos(\phi) - r^2 \left[\cos\left(\phi + \frac{\pi}{n}\right) - \cos\left(\frac{\pi}{n}\right)\right]^2}{(h_o - u)^2 + r^2 \left[\cos\left(\phi + \frac{\pi}{n}\right) - \cos\left(\frac{\pi}{n}\right)\right]^2} \tag{S11}$$

During the compression process, the total elastic energy stored in the creases, denoted as U, can be calculated as the sum of the deformation energy of the peaks and valleys, U_b, and the contribution from the rotational springs of the creases, U_s, as given by the following expressions, which are defined by five parameters: b, c, δ_a, δ_b and δ_c.

$$U_b = \frac{1}{2} n K_{sb} (b - b_o)^2 + \frac{1}{2} n K_{sc} (c - c_o)^2 \tag{S12}$$

$$U_s = \frac{1}{2} n K_a (\delta_a - \delta_{ao})^2 + \frac{1}{2} n K_b (\delta_b - \delta_{bo})^2 + \frac{1}{2} n K_c (\delta_c - \delta_{co})^2 \tag{S13}$$

$$U = U_b + U_s \tag{S14}$$

Here, K_{sb} and K_{sc} represent the stretching stiffness of the peaks and valleys, respectively, while the rotational stiffness of the creases is represented by K_a for the side polygon, K_b for the peaks, and K_c for the valleys. The total potential energy in the Kresling cell, $\Pi(u)$, can be determined by the sum of the total elastic energy stored in the creases U, and the work done by the external force F that produces an axial displacement u:

$$\Pi(u) = U - Fu \tag{S15}$$

If we adhere to the principle of minimum total potential energy, we can identify an equilibrium state (*47*). Thus, we assume that:

$$\delta\Pi/\delta u = 0 \tag{S16}$$

Then, we can define the applied axial force F, under the mentioned equilibrium conditions and in terms of the total elastic energy stored energy in the creases, as follows:

$$F = \delta U/\delta u \tag{S17}$$

The previously mentioned equations enabled a preliminary evaluation of various geometrical configurations to determine the initial sizing of a Kresling cell. The energy landscapes calculated from Eq. S14, determined which initial geometrical parameters can be used to shape Kresling cells prone to ensure a second local of energy minimum and satisfying the condition $\delta U/\delta u = 0$, for further analyses. The geometrical configurations considered in this preliminary assessment include: aspect ratios h_o/r within the range of 0.4 to 2.25, polygons with a number of sides equal to n=6 and initial rotational angles θ_o ranging from $\pi/4n$ to $3\pi/n$ ($7.5° \leq \theta_o \leq 90°$). The total elastic energy stored in the creases U, and axial displacement u, were normalized to represent dimensionless quantities in the plots.

The stretching stiffness K_s is defined in terms of Young's modulus E, and cross-sectional area A as $K_s = EA$. By defining the stretching stiffness of the peaks and valleys per unit length, we obtain $K_{sb} = K_s/b_o$ and $K_{sc} = K_s/c_o$, respectively. Similarly, the rotational stiffness K, can be also expressed per unit length, with $K_b = Kb_o$ for the peaks and $K_c = Kc_o$ for the valleys. For this initial analysis, the contributions of both stiffness components to the total elastic energy were introduced as three different ratios: $K/K_s = 0, 0.5 \times 10^{-4}, 1.0 \times 10^{-4}$. As a result, two main scenarios were observed during the compression process of the Kresling cells: Bistability (Bi) and Monostability

(M), as illustrated in the plots of Fig. S1B. When considering a rotational stiffness $K = 0$, the results correspond to those obtained by the bar and truss model defined by two parameters, (b,c).

Configurations with an initial rotational angle within the range $15° \leq \theta_o \leq 60°$ and an aspect ratio $h_o/r \geq 1.5$ exhibited an apparent bistability. Those Kresling cells showed normalized energy landscapes with a second local of energy minimum ($\delta U/\delta u = 0$). In addition, we observed that the majority of configurations with initial rotational angles lower than $\theta_o = 40°$ and h_o/r <1.5 tended to present a monostable behavior. While those with higher values, $\theta_o > 60°$, allowed small rotational displacements limiting the folding process and the panels tended to overlap prematurely. In contrast, Kresling cells with initial relative angles $\theta_o < 7.5°$, were prone to buckle during the initial folding stages, displaying an almost rigid behavior and higher energy values. Furthermore, Fig. S1C presents the corresponding normalized force and elastic energy landscapes obtained for the configuration: $\theta_o = \pi/6$, and h_o/r=1.75. It exhibited a potential tendency towards bistability in all the evaluated scenarios $(K/K_s = 0, 0.5 \times 10^{-4}, 1.0 \times 10^{-4})$. Thus, we selected these geometrical parameters for the initial sizing of the Kresling cells used in the subsequent analyses.

S.1.2 Parametric design of 3D Kresling cells

The 3D CAD parametric models were generated in Autodesk Inventor following the initial geometrical configuration: polygons with n = 6 sides, initial relative angle $\theta_o = \pi/6$, initial height versus radius ratio h_o/r=1.75, and panels thickness $\overline{s} \approx 0.04 h_o$. The parametric design process is summarized in Fig. S2. Firstly, the upper and lower polygons are defined in 2D sketches and rotating with respect to each other in an angle equal to $\theta_o = 30°$. The panels thickness $\overline{s}$ was defined through an offset to the polygons' perimeter and the width limit of the creases was determined by auxiliary circles with radius r'. Then, 3D sketches were constructed to enable the 3D structure of the panels, and by using the command Boundary-surface their profiles can be linked to form the surfaces of the panels. Next, the surfaces were merged with the Patch command, and volumetric bodies were obtained to shape the panels and the creases. As a result we obtained a 3D Kresling cell which represent the intact crease case.

The creases were designed with gradual reductions in their cross-sections, preserving a V shape at the top and a variable circular shape at the bottom. A cutting radius $s_c = r' \cdot RF$ is

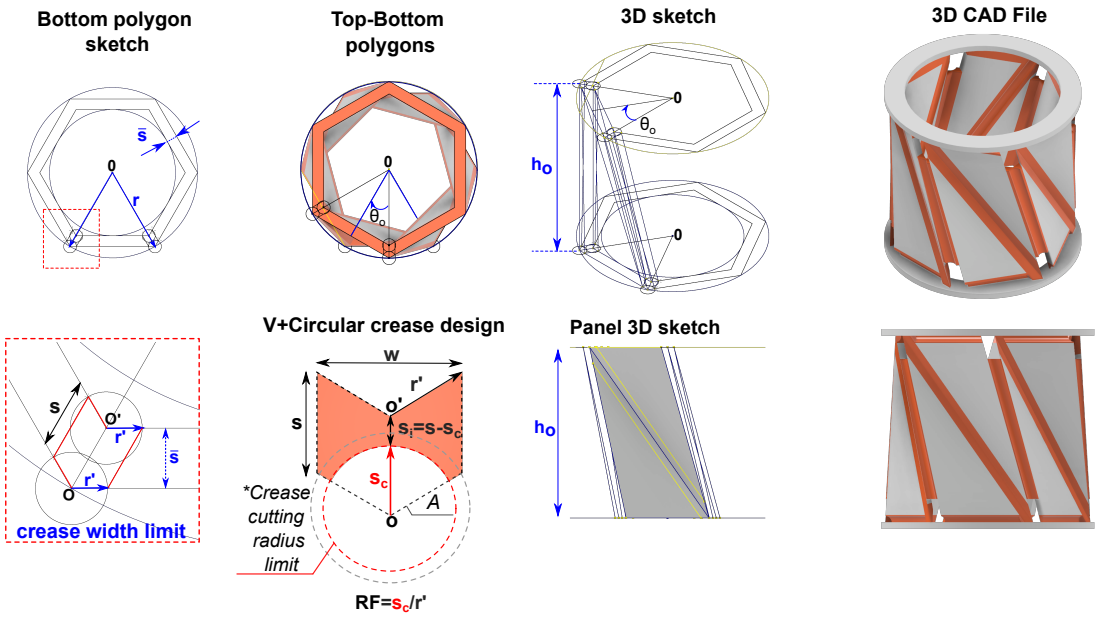

Figure S2: **Parametric design process of a 3D Kresling cell**. Creation of former 2D and 3D sketches in Autodesk Inventor.

defined according to the imposed reduction factors from $0.25 \leq RF \leq 0.80$, decreasing the external thickness s and an internal thickness s_i is obtained. Afterwards, the 3D CAD model were saved as *.step files for the Abaqus/CAE numerical simulations.

S.1.3 Numerical simulations considerations

The entire modeling process for simulating the kinematics of Kresling cells and generating the load paths for the parametric study is schematized in Fig. S3. The input 3D CAD files for the Kresling cells models were saved as *.step files to be imported from Abaqus/CAE Standard for their assembly. Traditionally, 3D printed Kresling cells have been designed and modeled as linear elastic shells. This is particularly applicable to polymeric sheets with thicknesses less than 1 mm, while also considering the use of rigid or flexible materials. However, employing rubbery creases, which are treated as nearly incompressible material, requires the use of hyperelastic models with 3D hybrid modified formulation elements to achieve more realistic results.

In addition, complex and irregular 3D geometries such as Kresling inspired structures, require the use of tetrahedron elements besides the application of free mesh with partition strategies. Thus, intricate shapes can be accurately modeled while maintaining computational efficiency at the

same time. Given the hyperelastic nature of the flexible Polyjet photopolymers, the selected mesh was composed by 10 node quadratic tetrahedron with hybrid modified constant pressure elements C3D10MH. An adaptive mesh refinement study determined a suitable mesh density that enables the achievement of convergence within a balanced computational time.

Four types of tetra-mesh from a coarse to refined number of elements were analyzed comparing their obtained maximum force, that leads to the highest stress concentrations on the Kresling cell, as well as the CPU time and refinement error ($R_E(\%)$), as described in Fig. S4. The latter was obtained by using the expression: 100 $(F_{Mi} - F_{M4})/F_{M4}$, where F_{Mi} represents the maximum force obtained in the numerical simulation with each mesh case i, F_{M4} is the maximum force from the last attempt corresponding to the very refined mesh case M4. The selected mesh corresponded to the case M3, which is formed by minimum three elements assigned across the panels and creases cross-sections. This refined mesh fitted more accurately to the Kresling cell geometry, reducing modeling errors and ensuring convergence.

Moreover, kinematic couplings were assigned between the reference points RP and the top and bottom ring surfaces to effectively transmit the applied displacement, and the assigned boundary conditions along the entire cylinder. The constitutive models used in the analyses included an elasto-plastic model for the rigid photopolymers assigned to the panels, and a visco-hyperelastic model for the flexible materials assigned to the creases.The material characterization data necessary to define these constitutive models were obtained through uniaxial tests, detailed in the following sections S.1.5 and S.1.6, and summarized in Tables S1 and S2.

Furthermore, tie constraints were used to create a uniform contact among the panels, creases, top and bottom ring surfaces. Fixed boundary conditions were applied at the bottom of the cylinder, specifically at reference point RP_1, to restrict displacements and rotations in all directions. A vertical displacement, u, approximately equal to one third of the initial height of the Kresling cells ($\approx 1/3\ h_o$), was imposed at the top in the respective reference point RP_2 and the corresponding applied Force was computed to determine the respective force/displacement curves. This target displacement prevents further overlapping of the panels during the compression of the Kresling cell.

The rotation at the top was released to simulate the natural twisting plus compression motion of Kresling cells. A VISCO step was used to perform quasi-static analyses, incorporating time-

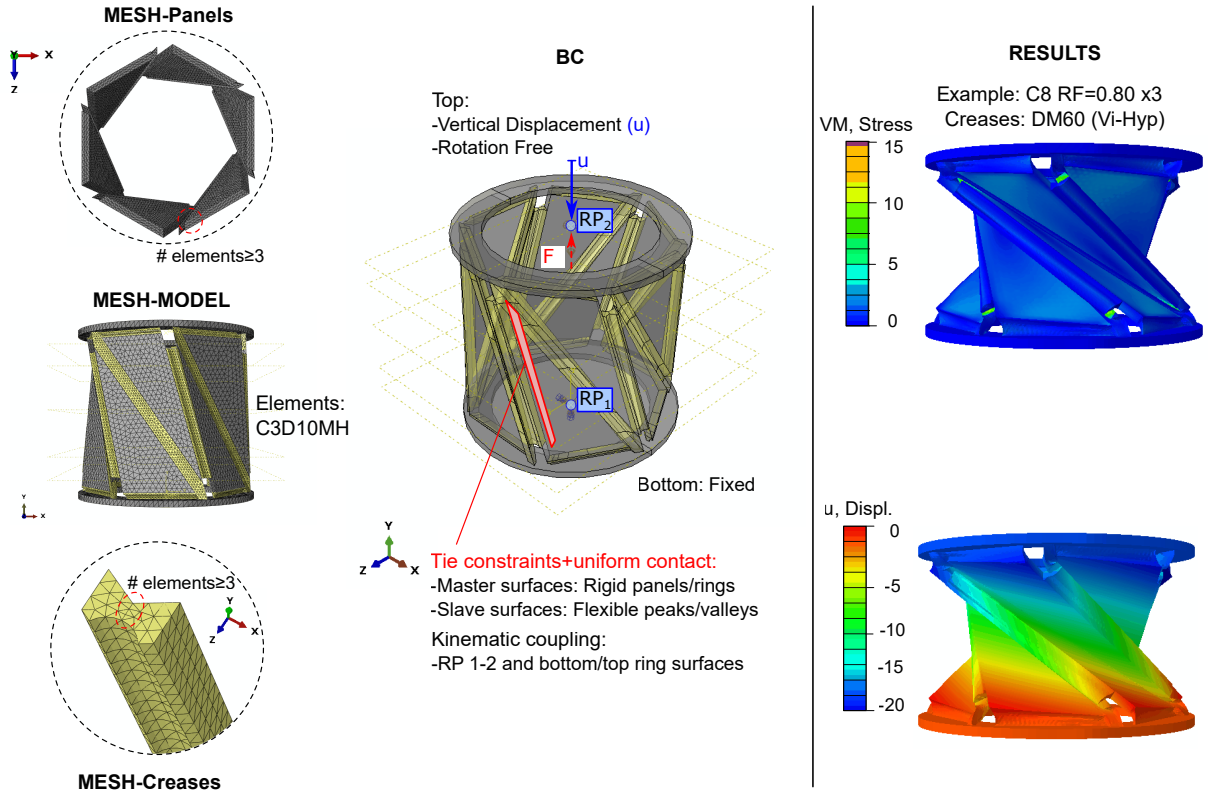

Figure S3: **Numerical simulations process in Abaqus/ CAE Standard.** Mesh generation, boundary conditions (BC) and example of obtained results in terms of Von Mises stress in MPa, VM, and vertical displacement, u, in mm. *RP_2 represents the reference point where the vertical displacement is applied, generating a restoring force F_R considered for the load path plots.

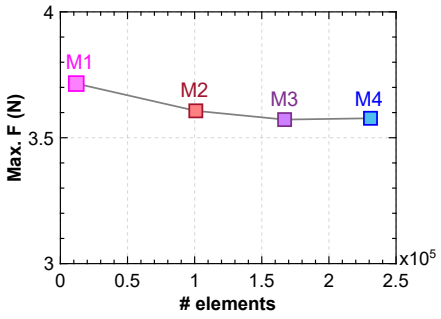

Mesh	# elements	Cr_s	PA_s	CPU_{time} (s)	R_E (%)
M1	11816	1.10	1.00	731	3.85
M2	100877	0.30	0.60	23104	0.83
M3	167011	0.25	0.50	25318	-0.15
M4	230964	0.20	0.40	60982	-

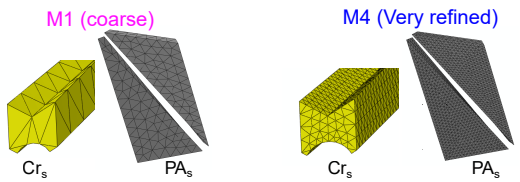

Figure S4: **Mesh refinement study parameters.** Based on the maximum force achieved, Max(F), total number of elements, including number of seeds along creases (cr_s) and panels (PA_s), CPU time in seconds and refinement error percentage $(R_E(\%))$.

dependent material behavior without inertia effects. The geometric nonlinearity option (NLGEOM) was activated to consider large deformations in the analysis. We first focus on the initial relaxation region of the analyzed rubbery materials within a time defined as τ_i^*, during which most of the stress decay occurs, as shown in Fig. 4B, to observe the viscosity effects during bistability achievement. Then, the total simulation duration t_t was estimated to lie within this initial relaxation region by using a velocity of 0.1 mm/s to reach the target displacement u. The VISCO step was defined with a initial time size set to $0.01t_t$, while the maximum and minimum increments were $0.1t_t$ and 10^{-6}, respectively. Thus, we can accurately capture the viscosity effects and ensure the convergence by reducing the number of increments in the solver. In addition, we performed simulations for each rubbery material over extended time periods to predict whether bistability can also be achieved in both short- and long-term relaxation regions. For instance, to determine the total simulation duration t_t for the short-term relaxation region, we considered a reference time τ equal to the highest τ_i term from the Prony series described in Table S2. In this region, a lower stress decay in the relaxation curve of each rubbery material was also observed. For long-term effects, when the material is fully relaxed and the stress relaxation curve approaches a horizontal asymptote, we used total simulation durations t_t of $n\tau$, with n=6.

S.1.4 Design and Fabrication of samples for tensile tests

Polyjet photopolymers main groups can be classified into rigid thermoplastics, rubbers and a hybrid types of composites, so called Digital Materials. The latter represent a combination between glassy and flexible polymers, with various levels of shore hardness from A30 to A95. In the present study, the selected rigid photopolymers were VeroYellow, VeroBlack and Digital ABS. The tested rubbery Digital Materials were: AgilusClear 30 (Shore A30), FLXA-YT-S60 DM (Agilus30 + Vero Yellow, Shore A60), FLXA-9970 DM (Agilus30 + VeroClear, Shore A70), FLXA-9985 DM (Agilus30 + VeroClear, Shore A85) and FLXA-YT-S95 DM (Agilus30 + VeroYellow, Shore A95). In this study they are referred with the acronyms AG30, DM60, DM70, DM85 and DM95, respectively.

All the samples were fabricated using a 3D printer Stratasys J750 with a layer resolution of approximately 27 microns in High-Mix mode. The support material was first smoothed in a soapy water solution bath for one hour and then, it was removed using water jetting.

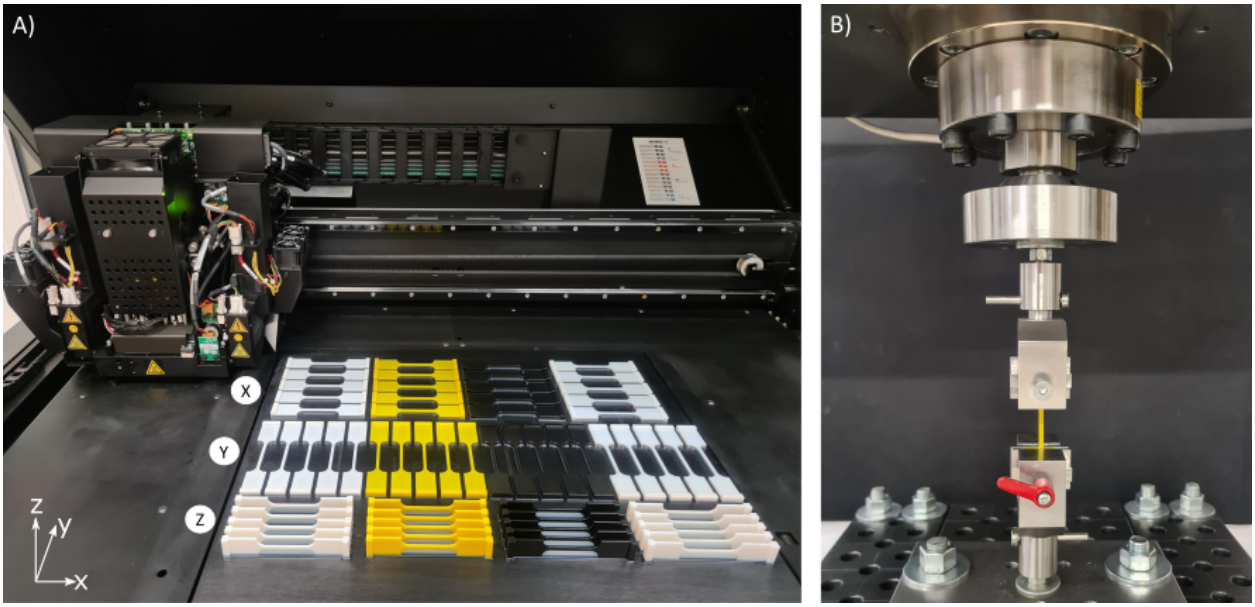

Figure S5: **Specimens made of photopolymers for uniaxial tests. (A)** Fabrication via Polyjet technique with orientations along the X,Y,Z axis of the build tray. **(B)** Experimental setup for uniaxial tests.

For the uniaxial tensile tests, dog-bone-shaped samples were designed following the ASTM D638 standard for rigid polymers, and the ASTM D412 standard for rubbers. Five samples were fabricated for each material type. They were printed in three directions: longitudinal (X), transversal (Y) and perpendicular (Z) to the build tray, as shown in Fig. S5A. For the stress relaxation tensile tests conducted on the rubbery material, dog-bone sample design adhered to the ISO 6914, ASTM E328, and ASTM D412 standards. Three samples were printed longitudinally oriented to the build tray for each type of Digital Material.

S.1.5 Uniaxial tensile tests and constitutive models

The uniaxial tests were carried with a MIDI 10 testing machine by imposing a cross-head velocity of 0.1 mm/sec, as shown in Fig. S5B. The tests stopped when fracture occurred in the sample. During the test both applied displacement and load were recorded. In particular, two types of load cells with different capacities were used to measure the applied tensile load during the experiments: 100kN for rigid polymers, and 10 kN for rubbery materials. The data rate acquisition was equal to 1 sample/sec. The constitutive models employed in the numerical simulations, were obtained based on experimental data from the previously mentioned uniaxial tests. The average among the different

printing orientations, in X,Y and Z, was considered for the mechanical properties estimation. In the case of rigid photopolymers, such as VeroBlack (VB), an elasto-plastic model was selected. The average stress-strain curves and Young's modulus are shown in Fig. S6A and B, respectively. The Young's Modulus was estimated from the slope of the $\sigma - \varepsilon$ curves within the elastic range. The latter is determined by fitting a straight trendline to the experimental curve, which extends from the beginning of the curve to the point where the R^2 values approach closest to 1. The elasto-plastic behavior was modeled in Abaqus/CAE standard, considering the experimental $(\sigma - \varepsilon)$ curves by using the material calibration utility.

First, the nominal $(\sigma - \varepsilon)$ curves inputs get converted into true strains (ε_t) and true stresses (σ_t) with the expressions: $\varepsilon_t = \ln(1 + \varepsilon)$ and $\sigma_t = \sigma(1 + \varepsilon)$. The Young's modulus is calculated as previously explained and used as an input datum. Thus, the yield point can be identified and the plastic strains, ε^{PL}, and stresses, σ^{PL}, are finally estimated to characterize the elasto-plastic model: $(\varepsilon = \varepsilon^{EL} + \varepsilon^{PL})$. Moreover, we evaluated the loss of mechanical properties over time of rigid photopolymers from the Vero group, such as VeroBlack (VB). Similarly, samples were fabricated and tested one day, one and six months after, following the mentioned uniaxial test procedure.

Rubbery materials are mostly defined by strain energy potential functions due to their hyperelastic behavior. Their mechanical characterization requires a further step to find a model that fits the nominal curves $(\sigma - \varepsilon)$ with the tensile tests of the Digital materials group: AG30, DM60, DM70, DM85 and DM95. Considering that the experimental data was obtained from uniaxial tests, the material constants C_{ij} from linear hyperelastic polynomial models were fitted to the nominal stresses. Thus, they were calculated through a least-squares method in Abaqus/CAE material model calibration tool (*48*). Then, the relative error (RE) of the stress measure is minimized and it is defined by the expression:

$$RE = \sum_{i=1}^{n} \left(1 - \frac{\sigma_i^{th}}{\sigma_i^{exp}}\right)^2, \tag{S18}$$

where σ_i^{exp} represents the experimental stress measures and σ_i^{th} is the nominal stress. In this case, the latter is determined by the tensile uniaxial stress T_1, which is derived from the strain energy potential U and the stretch in the loading direction λ_1, as follows:

$$T_1 = 2(1 - \lambda_1^{-3}) \left(\lambda_1 \frac{\partial U}{\partial \overline{I_1}} + \frac{\partial U}{\partial \overline{I_2}}\right) \tag{S19}$$

Thereby, a Neo-Hookean model fitted the nominal stresses of the tested digital materials group

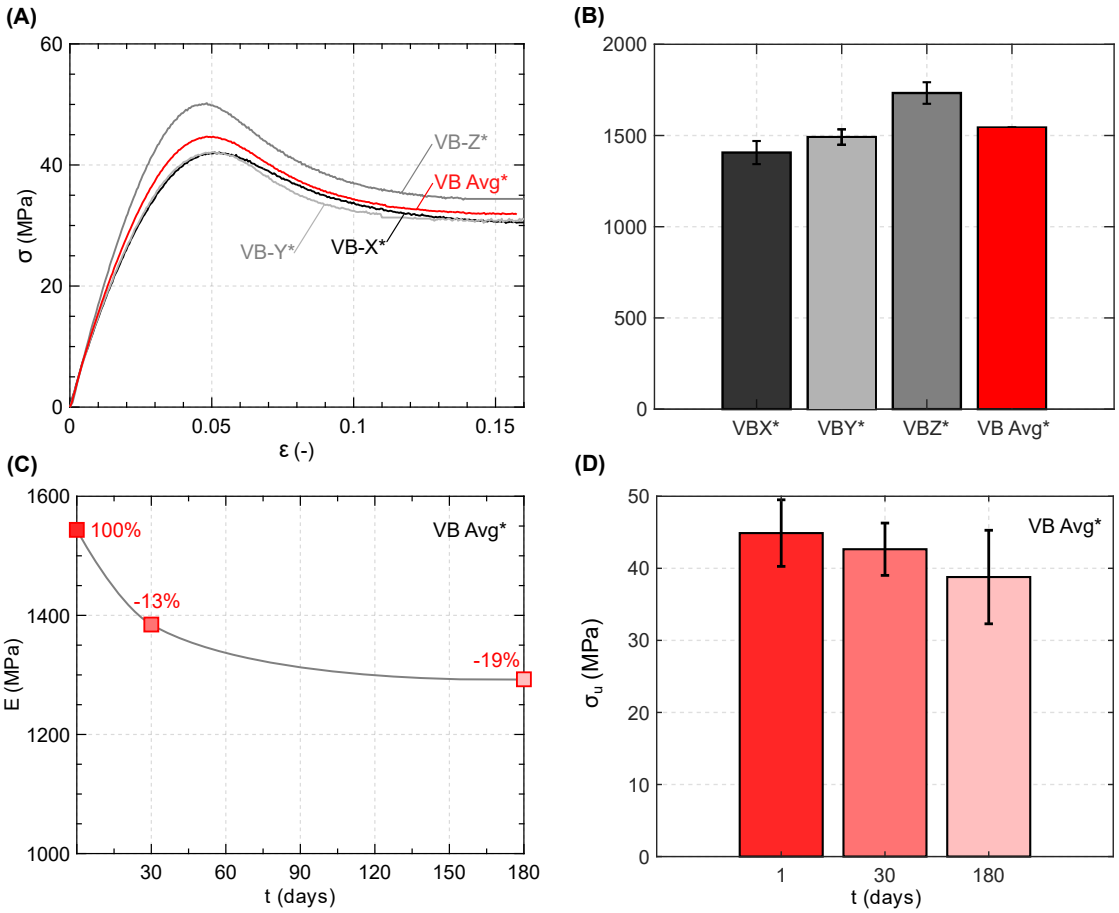

Figure S6: **VeroBlack experimental data.** **(A)** Average Stress-Strain ($\sigma - \varepsilon$) plots. **(B)** Average Young's modulus E +/- standard deviation obtained per each group of samples with a printing orientation in X, Y, and Z axis, and overall average (VB Avg*). Loss of mechanical properties, including: **(C)** Young's modulus, E, and **(D)** Ultimate tensile strength, σ_u, due to aging effects analyzed using data obtained from tests conducted after 1 (E=100%), 30, and 180 days of sample fabrication.

from AG30, DM60 to DM95 as Fig. S7A depicts. The fitting was obtained with relative errors between the range $5\% \leq RE \leq 10\%$. Moreover, this strain energy function is described in Invariant base form as: $U_N = C_{10}(\overline{I_1} - 3)$, and its equivalent stretch base is written as:

$$U_N = \frac{\mu_{10}}{2}(\lambda_1^2 + \lambda_2^2 + \lambda_1^{-2}.\lambda_2^{-2} - 3), \tag{S20}$$

Additional mechanical properties, including average elongation at break (ε_b), were determined from the experimental curves ($\sigma - \varepsilon$), as shown in Fig. S7B. Other hyperelastic models, such as Mooney-Rivlin and Polynomial N=1, showed higher relative error values ranging from $10\% \leq RE \leq 32\%$, and they also presented unstable strains during the calibration process.

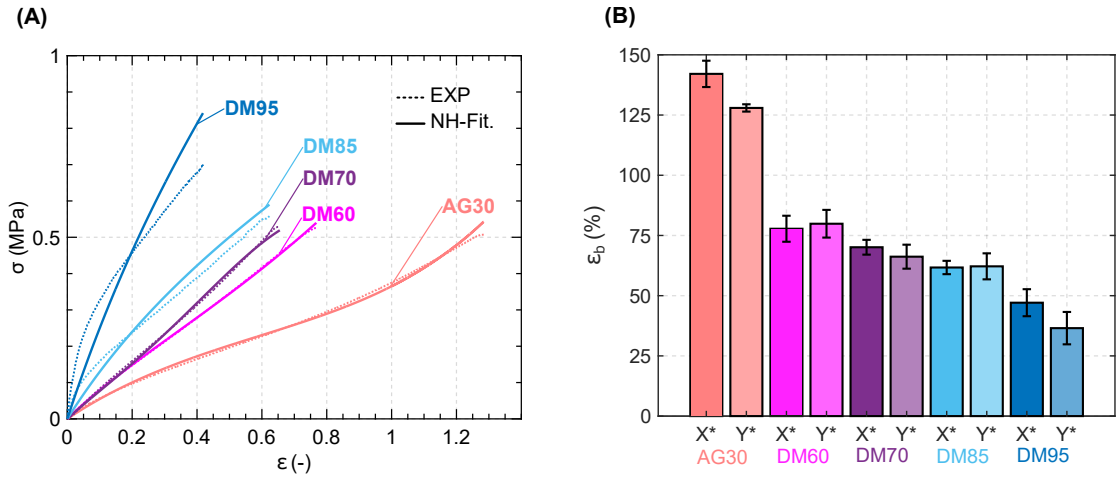

Figure S7: **Rubbery Digital materials (DM) experimental data. (A)** Average stress-strain curves obtained during the uniaxial tests (Exp) and hyperelastic models fitting with Neo-Hookean (NH-Fit) strain energy potential. **(B)** Average Elongation at break, ε_b, +/- standard deviation. (*) Average obtained per each group of samples with a printing orientation in X and Y axis.

S.1.6 Stress Relaxation tests and Viscoelastic parameters

Rubbery materials present high sensitivity to strain rates and time-dependent behavior, which can be further characterized by a visco-hyperelastic model. The time dependent constitutive equations that define linear viscoelastic materials, are based on the stress and strain history, loading-displacement rate and loading application time. Polyjet elastomers usually exhibit a significant relaxation of their peak stresses in a short time span, some of them reaching it in 20 seconds (*39*).

The most common viscoelastic models are based on the combination in series or in parallel of linear elastic (springs) and viscous components (dashpots). Then, the viscoelastic components can be determined by conducting a stress relaxation test and therefrom, obtaining the subsequent Prony parameters. The load and time data considered for determining the viscoelastic properties are recorded once the imposed strain value ε_0 is reached. The initial part of loading phase, where the strain is rapidly increasing, is usually disregarded. After this initial phase, a time t=0 is established as the starting point for analysis under a constant strain ε_0, together with an initial stress σ_0 and the corresponding elastic instantaneous modulus E_o. Therefore, the time dependent stress $\sigma(t)$ is defined by:

$$\sigma(t) = E(t)\varepsilon_o \tag{S21}$$

Considering that the material behaves as a Maxwell solid, the time dependent relaxation modulus E_t can be expressed in terms of a Prony series expansion and calculated from E_o (*49*), as shown below:

$$E(t) = E_o \left(1 - \sum_{i=1}^{N} E_i(1 - e^{-t/\tau_i})\right) \tag{S22}$$

where E_i corresponds to the "i-th" Prony coefficient, N represents the total number of terms of the Prony series, and τ_i is the relaxation time constant. Thereby, the Tensile relaxation modulus $E(t)$, can be determined by $E(t) = \sigma(t)/\varepsilon_0$. Then, the Shear relaxation modulus $G(t)$, can be obtained by the expression: $G(t) = E(t)/[2(1+\nu)]$ and the corresponding values per each analyzed rubbery photopolymer are illustrated in Fig. S8A. Furthermore, the tensile instantaneous relaxation modulus E_o, corresponding to the time t=0, is defined by $E_o = \sigma_0/\varepsilon_0$. Similarly, the shear instantaneous relaxation modulus G_o, is calculated by $G_o = E_o/[2(1+\nu)]$. The Poisson's ratio ν of elastomeric photopolymers and composites with shore hardness between DM60 and DM95, can vary from 0.48 to 0.46, and 0.49 for the rubbery AG30 (*38*). The rate-independent behavior of the material can be defined as hyperelastic under large strains in Abaqus/CAE solvers and being described by the instantaneous relaxation tensile modulus. After, we estimated a normalized shear relaxation modulus from the experimental curve $(G(t) - t)$ employing the expression: $G_n = G(t)/G_0$. Thus, Eq. S22 can be re-written in terms of the normalized shear relaxation modulus $G_n(t)$, and the dimensionless Prony constants g_i, as follows:

$$G_n(t) = 1 - \sum_{i=1}^{N} g_i(1 - e^{-t/\tau_i}) \tag{S23}$$

In addition, the long-term shear relaxation modulus G_∞ is defined by the shear instantaneous relaxation modulus G_o and the dimensionless Prony constants g_i, as given by Eq. S22:

$$G_\infty = G_o \left(1 - \sum_{i=1}^{N} g_i\right) \tag{S24}$$

Assuming a linear viscosity and nearly incompressibility of the material, given that the Poisson's ratio of the studied rubbery materials ranges within 0.46 and 0.49, the long-term tensile relaxation modulus can be estimated as: $E_\infty = G_\infty[2(1+\nu)]$.

The viscoelastic material properties, defined by the dimensionless Prony series parameters, can be determined by fitting them to experimental relaxation test data. For this reason, a series of stress

relaxation tests in tension were performed by adapting the ISO 6914 and ASTM E328 standards. Three different constant strain values, $\varepsilon_0 = 10\%$, $\varepsilon_0 = 15\%$, and $\varepsilon_0 = 25\%$, were imposed on each rubbery sample.

The stress relaxation tests for rubbery materials were conducted with a MIDI 10 testing machine by imposing a cross-head velocity of 0.1 mm/sec and at controlled room temperature (23 °C). A 10 kN load cell measured the applied tensile load. When the displacement corresponding to the target strain was reached, the machine stopped and the load relaxation was monitored. At this point, an initial time $t = 0$ is established in the force-time curve $(F - t)$, along with its corresponding peak force F_o and a constant strain ε_o. The tests were considered concluded when the force-time curve $(F - t)$ approached an almost horizontal asymptotic line.

Subsequently, the stress depending on time $\sigma(t)$ was calculated by dividing the force $F(t)$ by the cross-sectional area of the sample A_o. This conversion transformed the force-time $(F - t)$ curve into a stress-time $(\sigma - t)$ curve, which begins at the peak stress σ_o. Next, the average $(\sigma - t)$ curves for each group of samples subjected to constant strain values, $\varepsilon_0 = 10\%$, $\varepsilon_0 = 15\%$, and $\varepsilon_0 = 25\%$, were obtained.

Since the Kresling creases are designed to overcome large deformations, and ISO 6914 standards recommend the use of high strain values, we selected the maximum strain value (ε_o=25%) for estimating the Relaxation modulus and the Prony series parameters. The difference between the $G(t)$ and $G_n(t)$ curves obtained from the average values and the selected maximum strain (ε_o=25%) was not significant. We then applied these obtained Prony coefficients to the constants within the strain energy function $U_N(t)$ in order to introduce the rate-dependent behavior associated with viscosity. Consequently, in the case of a Neo-Hookean material model defined by an instantaneous constant C_{10}^o, the visco-hyperelastic relaxation function can be expressed as follows:

$$U_N(t) = C_{10}^o \left(1 - \sum_{i=1}^{N} g_i (1 - e^{-t/\tau_i})\right) \tag{S25}$$

These parameters are then incorporated into a visco-hyperelastic constitutive model described by Eq. S25 for subsequent numerical simulations in Abaqus/CAE.

Then, we fitted the obtained Prony parameters to the experimental data $(G_n - t)$ using a damped least squared method (DLS). It was implemented using a Matlab optimization toolbox script based on the Levenberg–Marquardt algorithm. As a result, the selected fitting coefficients correspond to

the lowest goodness of fit values, as shown in Fig. S8B. The latter is obtained from the norm of residuals, denoted as $\|e\|$ and calculated as follows:

$$\|e\| = \sqrt{\sum_{i=1}^{n} e_i^2}, \tag{S26}$$

where the residuals e_i represent the sum of the differences between the observed y_i and predicted values $f(x_i)$, being defined as: $e_i = y_i - f(x_i)$.

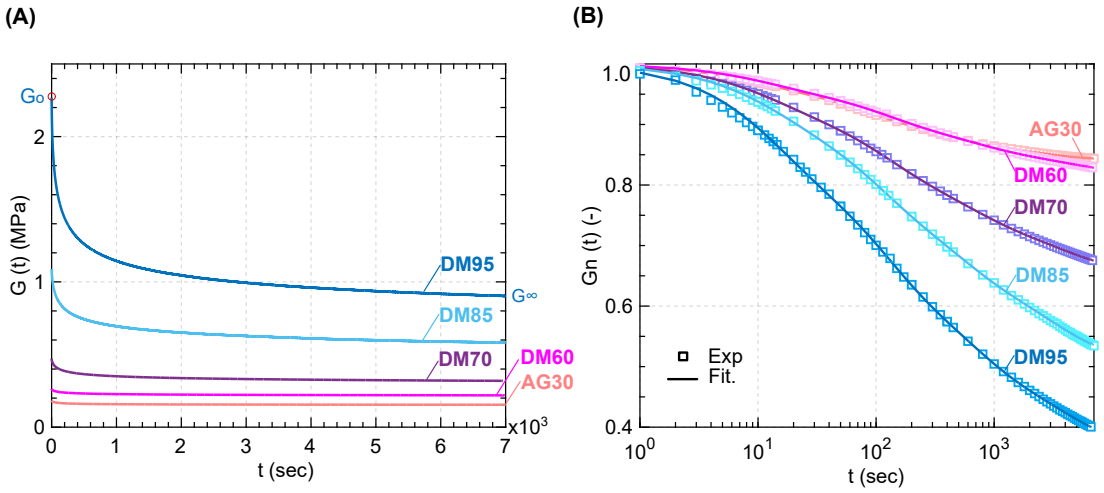

Figure S8: **Stress relaxation tests of the Rubbery Digital Materials AG30 to DM95. (A)** Relaxation function G(t) with the corresponding Instantaneous modulus G_o. Units: MPa. **(B)** Experimental and fitted data of the Normalized shear relaxation modulus $G_n(t)$, in logarithmic scale with their respective goodness of fit in terms of the norm of residuals $\|e\|$, where: AG30 $\|e\| = 3.9 \times 10^{-4}$, DM60 $\|e\| = 4.0 \times 10^{-4}$, DM70 $\|e\| = 5.8 \times 10^{-4}$, DM85 $\|e\| = 3.1 \times 10^{-3}$, DM95 $\|e\| = 2.5 \times 10^{-3}$.

Table S1: **Elastic and Elasto-plastic materials mechanical properties.**

Material	**E (MPa)**	σ_y **(MPa)**	ε_b **(%)**	σ_u **(MPa)**
VeroBlack	1543.58	19.79	15.75	44.89
UTL Resin (BMF)	567.00	10.00	40.80	14.10
Origin 402	42.00	-	230	5.5
IP-PDMS	15.30	-	240	-

Table S2: **Flexible materials mechanical properties and Prony series parameters.** $^*E_o$, E_∞, G_o, G_∞ units in MPa

AG30		**DM60**		**DM70**		**DM85**		**DM95**	
$C_{10} = 0.111$		$C_{10} = 0.157$		$C_{10} = 0.163$		$C_{10} = 0.237$		$C_{10} = 0.457$	
$E_o = 0.545$		$E_o = 0.782$		$E_o = 1.398$		$E_o = 3.200$		$E_o = 6.621$	
$E_\infty = 0.459$		$E_\infty = 0.651$		$E_\infty = 0.938$		$E_\infty = 1.676$		$E_\infty = 2.498$	
$G_o = 0.183$		$G_o = 0.268$		$G_o = 0.479$		$G_o = 1.095$		$Go = 2.267$	
$G_\infty = 0.154$		$G_\infty = 0.220$		$G_\infty = 0.317$		$G_\infty = 0.570$		$G_\infty = 0.855$	
g_i	τ_i	g_i	τ_i	g_i	τ_i	g_i	τ_i	g_i	τ_i
0.030	7.612	0.035	10.350	0.060	10.717	0.071	10.787	0.143	11.435
0.052	64.359	0.055	98.390	0.099	93.980	0.132	78.847	0.189	93.977
0.045	333.610	0.048	547.863	0.090	498.890	0.131	404.112	0.154	520.646
0.030	2310.2422	0.041	4151.017	0.089	3632.445	0.146	3116.457	0.137	3697.450

S.1.7 Fabrication protocol via Polyjet 3D printing technique

The 3D printed Kresling unit cell fabrication process contemplates three main stages: Design, 3D printing and Post-processing. During the design stage, the 3D CAD parametric models were generated in Autodesk Inventor. The selected geometrical configuration for the experimental validation of the Kresling cells is: C8 case, polygons with n = 6 sides, $\theta_o = \pi/6$, h_o/r=1.75, $t \approx 0.04h_o$, creases width/thickness ratio w/s =1.50 and $RF \leq 0.66$. The Kresling cell dimensions h_o=17.5 mm and r=10 mm, were scaled three times in order to make feasible their printing and to avoid the dimensional limitations regarding manufacturing. The other geometrical parameters and ratios were maintained to keep the proportions of the analyzed Kresling cells. The parametric design process was previously summarized in Fig. S22, section S.1.2. The 3D CAD model were saved as Parasolid files ($*.x_b$) to facilitate the exportation of the assembled components in a unique file for 3D printing. At the same time, it enables to identify separately the different components of the Kresling cells, such as panels, peaks, valleys and rings, for the assignation of different materials.

For the printing process, the GrabCAD software was used for the preparation of the printing

files to be send to a Stratasys J750 printer series, including automatic slicing. Once the files are imported, the respective dimensions and position along the build tray are controlled. Since the panels were conceived to be made of rigid materials, the VeroBlack photopolymers was selected. In the case of the creases, the following flexible materials were employed in different Kresling cells: AG30, DM60, DM70, DM85 and DM95. The selected support material was SUP706B with the standard grid density mode. It is important to remark that supports were also assigned to the panels during the printing process, because of the presence of inclined faces with respect to the build tray. The printing setting was the following: High-Mix mode with a layer resolution thickness of 27 microns and matte surface finishing.

The post-processing operations include mostly the supports removal, which demands to be meticulously carried on specially considering the small dimensions of the Kresling cells creases being at the edge of Polyjet manufacturing limitation $\leq$ 1.0 mm. The prolonged contact with water or alkaline solutions of small elements and multi-material interfaces lower than 1.0 mm cross-section, lead to a premature breakage and detachment. For this reason, the exposure of the 3D multi-material sample to humidity should be controlled. As an alternative, the support residues were carefully removed mostly by hand and briefly rinsed in water for less than five minutes.

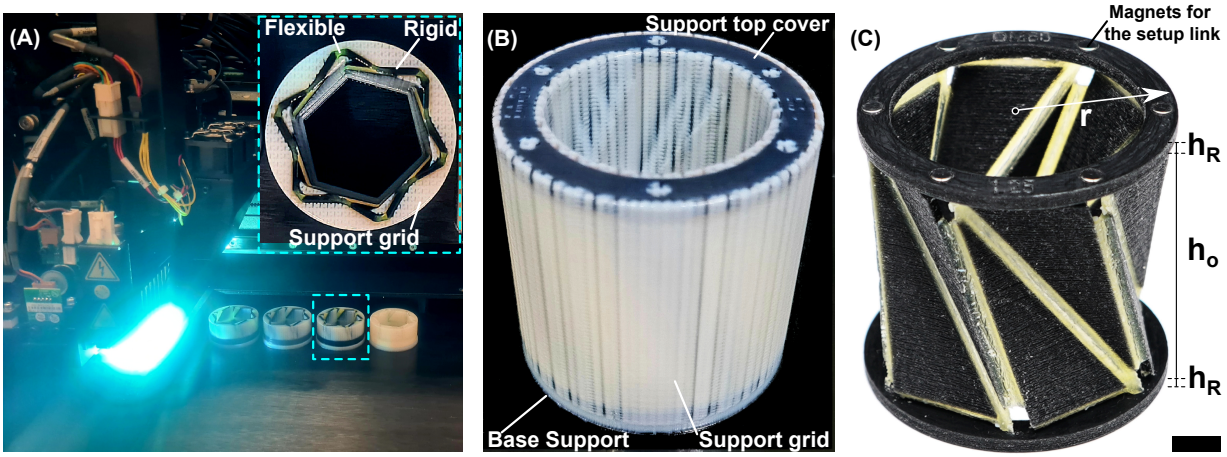

Figure S9: **Fabrication of multi-material Kresling cells. (A)** Polyjet printing process and multi-material deposition of rigid (VB), flexible (DM60) and support grid (SUP706B). **(B)** Support material distribution along the samples with matte surface finishing. **(C)** 3D printed Kresling cell from case C8 (RF=0.80) used in the experiments, with the following dimensions: r=30, h_R=3, h_o=52.50, and thickness of the panels $\bar{s}$=2.25. Units: mm. Scale bar: 10 mm.

S.1.8 Experimental setup

A further experimental validation was carried on to involve quasi-static tests on the 3D printed Kresling cells to validate the numerical simulations results. A compression load was applied at the top of the Kresling cell with a Messphysik μ-strain loading frame machine (from ZwickRoell, 0.01 µm stroke measurement resolution). The experiments were performed at a testing speed of 0.1 mm/sec. The applied Load F and displacement u were measured with a AEP TYPE F1-1kN load cell and with a displacement transducer mounted internally to the testing machine, respectively. The tests were stopped once a displacement $u = 1/3h_o$ was applied the sample. The experimental setups, shown in Fig. S10, consists of two fixtures. The top fixture guarantees free rotation, ϕ, during the folding of the Kresling (allowing the natural twist under compression inherent to Kresling patterns kinematics), while the bottom fixture prevent both displacements and rotations (*26*). The free rotational fixture is formed by a rotating plate coupled to a ball bearing (SKF 608 SKF 8x22x7) and a rotational fastener. The Kresling cell samples are directly linked to the top and bottom plates through two different systems. The first one consisted in a female-male connection system used for the Kresling cells with thicker creases, as shown in Fig. S10A. Pins were created on the surfaces of the samples rings and distributed to coincide with the vertices of the hexagonal polygons.

These pins were then inserted into the corresponding holes located in the plates. However, in this system, when using Kresling cells with thinner creases, the samples tended to slide. To prevent this problem, we implemented a second connection system based on magnets applied to the top and bottom of the samples and the plates, as described in Fig. S10B. The components of the first setup were 3D printed using the PolyJet technique on a Stratasys J750 3D printer, with tolerances of ±0.2 mm for holes and insertions. In contrast, the second setup was printed using the DLP technique through an Origin-One printer, with tolerances between ±0.1-0.25 mm for the magnet holes and insertions.

S.1.9 Hands-on experimental validation of Bistability

A manual compressive force was applied to the top of the Kresling cells, allowing free rotation at the top while constraining all displacements and rotations at the bottom. This action enabled us to recreate their spontaneous rotation, reflecting the characteristic kinematics during compression.

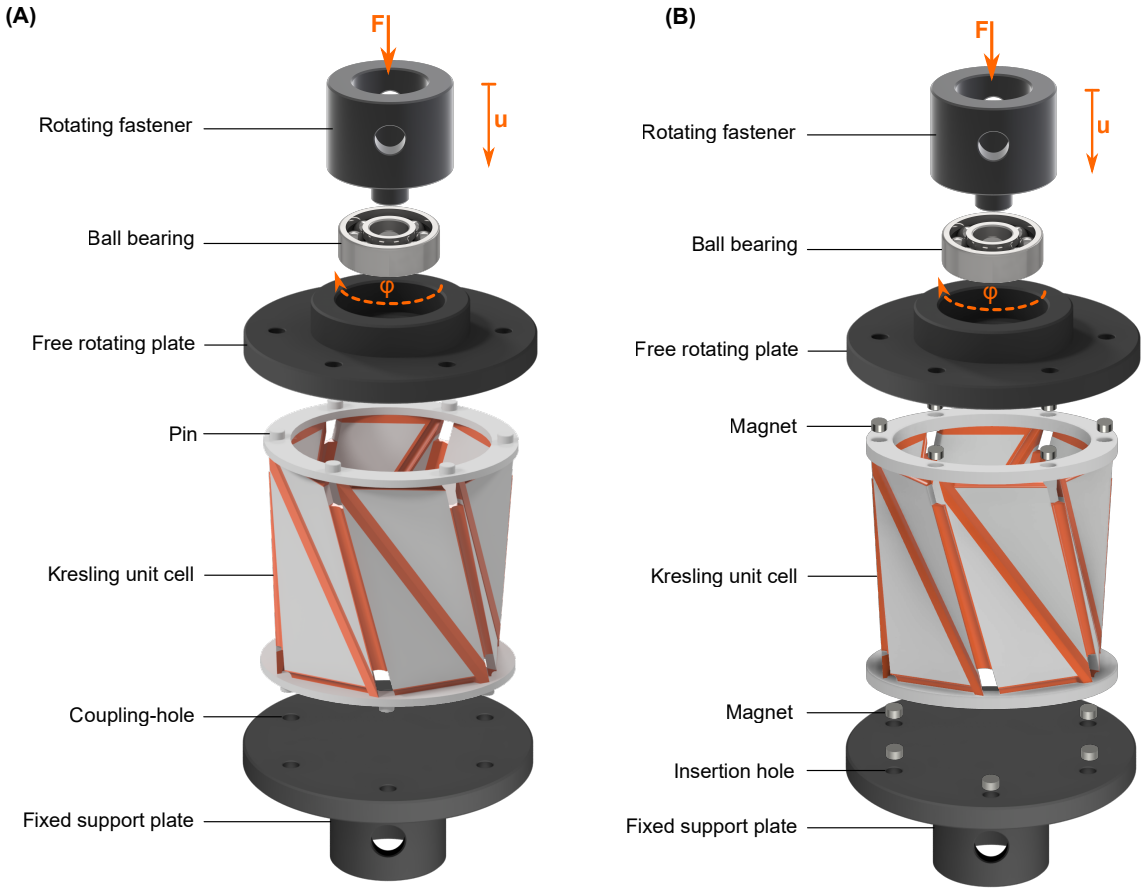

Figure S10: **Experimental setup for compression test with an applied Load F and displacement u.** Exploded schemes of the experimental setups with a fixture at the top, enabling a free rotation ϕ, and a fixed support fixture at the bottom with the following connection systems: **(A)** Pins and **(B)** Magnets.

Thus, we conducted a hands-on validation of bistability to determine which Kresling cells remained in the folded configuration after the manual force was applied. The applied compressive force generated an axial displacement u of approximately one third of the initial height h_o of the Kresling cell.

For example, we compared the behavior of Kresling cells with creases made of the rubbery material DM60 generated with gradual reductions (C8 RF=0.80) versus its corresponding intact creases cell, as shown in Fig. S11A. We also observed the effects of viscosity in Kresling cells (C8 RF=0.80) with creases made of different rubbery photo-polymers AG30, DM60, DM70, DM85 and DM95, as illustrated in Fig. S11B. In these hands-on experiments, we confirmed that all Kresling cells with creases generated with RF=0.80 remained in the folded configuration for over 60 seconds after the application of the manual compressive force, thus validating the achieved

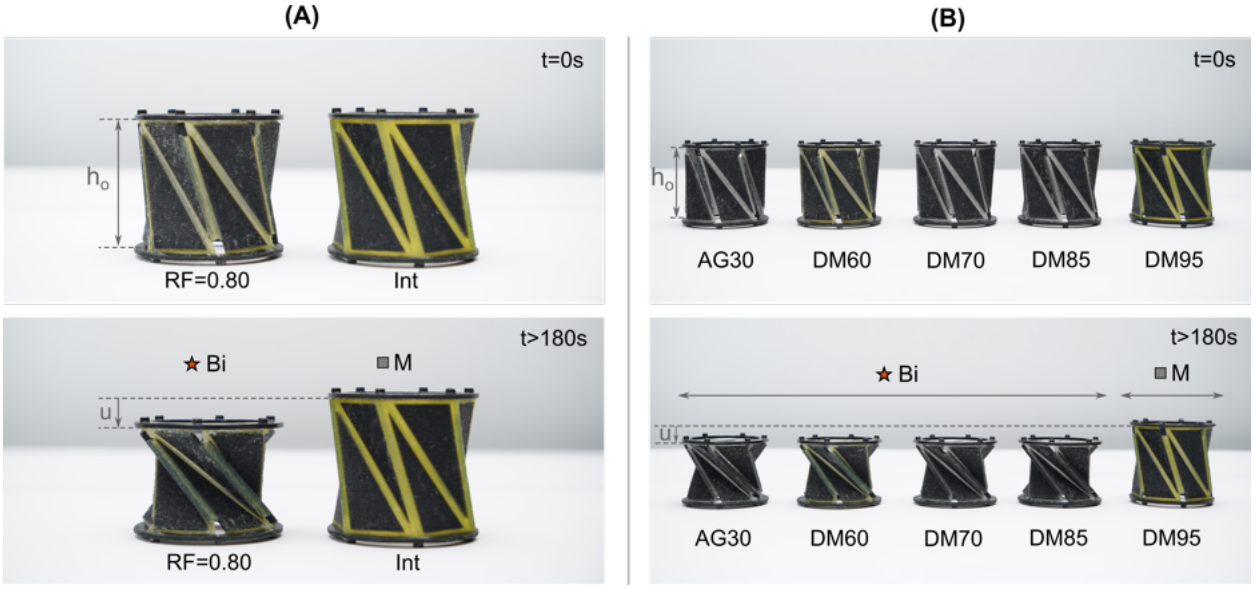

Figure S11: **Hands-on experimental investigation demonstrating the achievement of bistability (Bi) in 3D-printed multi-material Kresling cells of Case 8, by comparing their folding process.** **(A)** RF=0.80 versus Intact creases cell (Int). **(B)** Different RF=0.80 cells with creases made of rubbery photopolymers: AG30, DM60, DM70, DM85, and DM95. *Note: The Kresling cells were fabricated with an initial height h_o=52.5 mm, and rigid panels made of VB. The applied force aimed to achieve an axial displacement $u \approx 1/3 h_o$.

bistability in the experiments conducted with the testing machine. Conversely, the Kresling cells with creases made of the highly viscous DM95 or the intact cell immediately returned to their original configuration, exhibiting a monostable behavior. The complete hands-on experimental validation is further described in videos S2 and S4.

S.1.10 Microscopic characterization of 3D printed creases results

The dimensional accuracy of the printing process affects the real dimensions of the 3D printed Kresling cells. The measurements of the peaks and valleys creases from the case C8, with gradual reductions between $0.25 \leq RF \leq 0.80$, were analyzed. We established a comparison between those obtained in reality after the Polyjet process and the corresponding exact measurements in the CAD models. A transversal section passing through the half of the Kresling cell was considered to design the sample for the characterization of the geometry of both types of creases, peaks and valleys. This sample replicates the intermediate substrates of the 3D printed Kresling cell.

The real dimensions of 3D printed samples were determined via a stereo microscope (Nikon

SMZ800) equipped with an ED Plan 1.5x lens and with a DS-Ri2 camera. The mean values and the corresponding standard deviations (SD) were obtained from three real measurements (n=3) of the geometrical parameters characterizing the creases, as illustrated in Fig. S12 and Fig. S13 for both creases, peaks and valleys. We determined the corresponding mean percentage error, M_{PE} (%) between the dimensions from printed samples (Real) and those used from the CAD models, as follows:

$$M_{PE}(\%) = \frac{100}{n} \sum_{n=1}^{n} \left(\frac{M_{CAD} - M_{Real}}{M_{Real}} \right) \tag{S27}$$

The obtained real and exact measurements of the analyzed creases, with the respective M_{PE} (%) error are described in Fig. S14, in Fig. S15, Fig. S16 and Fig. S17, including peaks and valleys. The measurements taken along the multi-material interface between the rigid and the rubbery photopolymer show differences with an error between $2 \leq M_{PE}$ (%) ≤ 8. The transition zone where the two materials are merging is not homogeneous. For this reason, the dimensions along the edges of the 3D printed creases were not easily measured, potentially leading to an error. Since the internal thickness s_i is a crucial parameter for generating gradual reductions along the creases, we have selected this control parameter to evaluate the impact of differences between the exact and real measurements on the resulting experimental load paths and compare them to the numerical results. Subsequently, an updated CAD model of Kresling cells may be created by adjusting the internal thickness s_i according to the mean real measurements of the analyzed 3D printed creases.

Furthermore, we also observed that when the exact dimensions were designed less than 1.20 mm, the obtained real dimensions in the 3D printing process led to greater values exhibiting a negative error -1 $\leq M_{PE}$ (%) $\leq$ -25. Specifically, in the cases related to creases with smaller internal thickness s_i generated with the reduction factors ranging within $0.57 \leq RF \leq 0.80$. In contrast, a positive error is achieved within $3 \leq M_{PE}$ (%) ≤ 10, when the exact dimensions from the CAD files are above 1.20 mm, such as the cases with reduction factors between $0.25 \leq RF \leq 0.50$. It means that the resulting creases exhibited smaller real dimensions. This fact can be attributed to the printing limitation of fabricating defective load bearing elements with cross-sections around 1 mm, besides the characteristic dimensional accuracy of Polyjet J750 printers. In the case of printing with High-Mix mode, where the layer height reaches 13-16 microns, the exhibited dimensional accuracy ranges within ±0.06-0.1% for part lengths under ≈100 mm (*42*), even grasping values around ±0.10 mm in real applications.

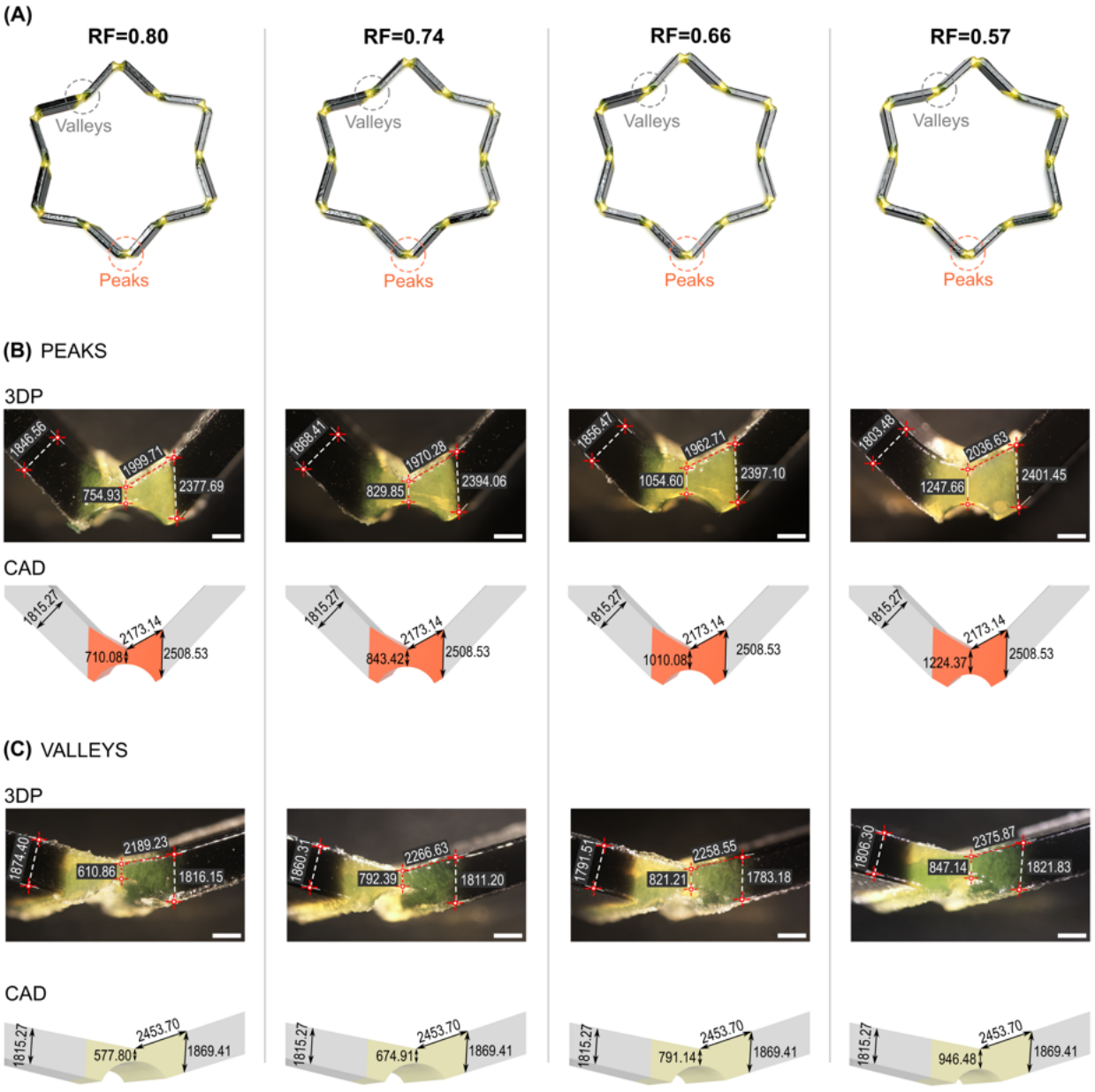

Figure S12: **Microscope characterization of 3D printed creases. (A)** Intermediate transversal section of the 3D printed Kresling cells from case C8 with gradual reduction factors ranging between $0.57 \leq RF \leq 0.80$ (scale 3:1). Comparison between the real (3DP) and the exact (CAD) measurements of the corresponding: **(B)** Peaks and **(C)** Valleys. Units: microns. Scale bar:1 mm.

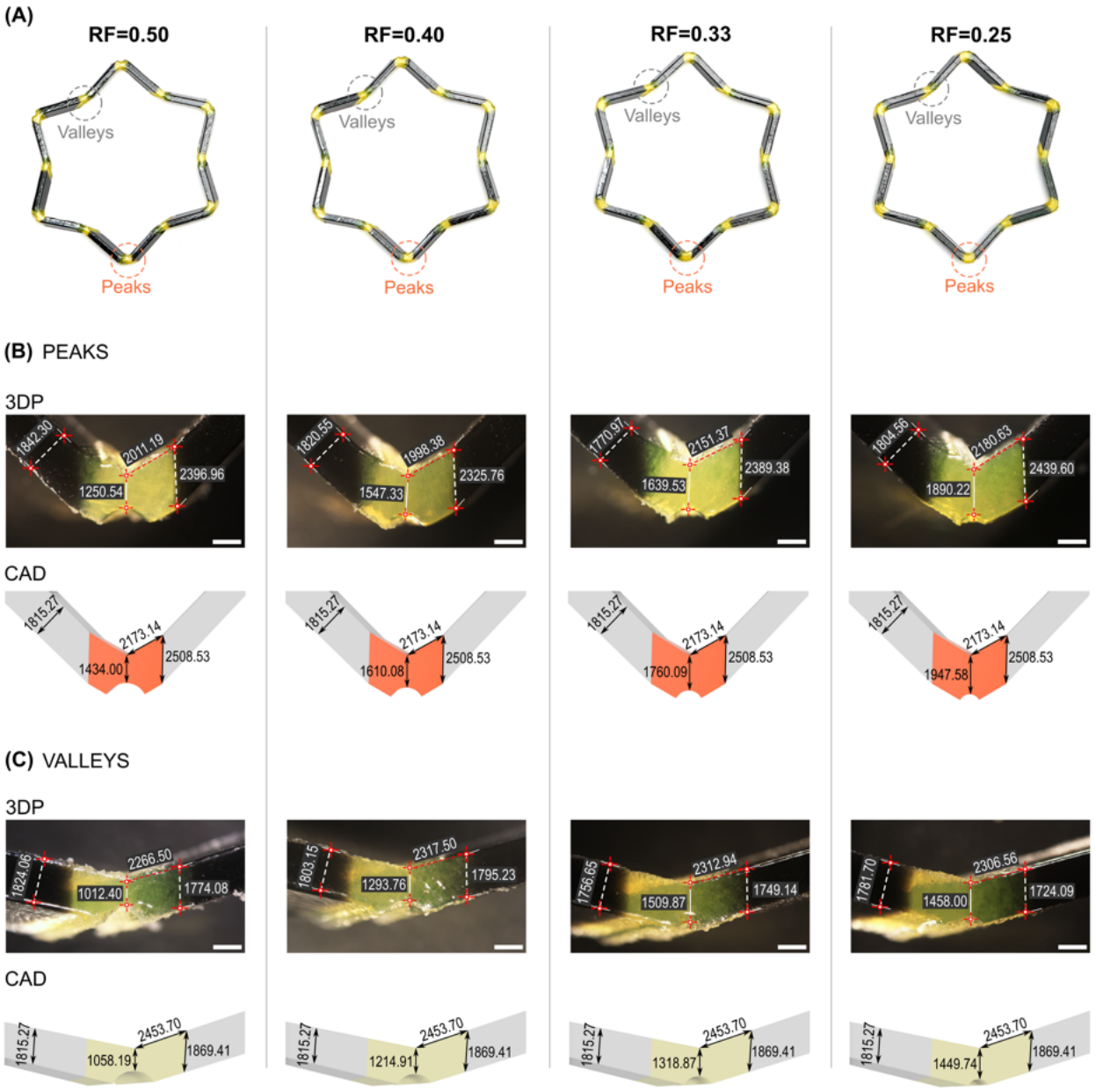

Figure S13: **Microscope characterization of 3D printed creases. (A)** Intermediate transversal section of the 3D printed Kresling cells from case C8 with gradual reduction factors ranging between $0.25 \leq RF \leq 0.50$ (scale 3:1). Comparison between the real (3DP) and the exact (CAD) measurements of the corresponding: **(B)** Peaks and **(C)** Valleys. Units: microns. Scale bar:1 mm.

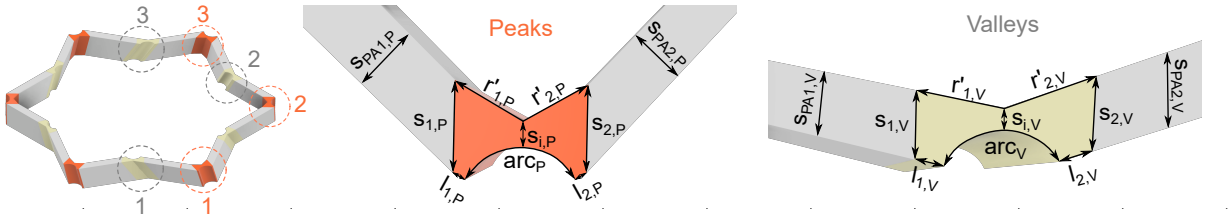

Geometrical Parameters RF=0.80											
Peaks measurements											
	Meas#	**r'1,P**	**r'2,P**	**si,P**	**s1,P**	**s2,P**	**sPA1,P**	**sPA2,P**	**arcP**	**l1,P**	**l2,P**
REAL	1	1805.42	1977.77	786.63	2336.39	2323.52	1842.47	1701.28	3843.36	421.35	487.45
	2	2049.90	2123.95	743.41	2567.10	2559.89	1840.53	1753.66	3947.92	335.62	347.94
	3	1797.31	1897.40	734.76	2350.34	2249.66	1856.68	1751.66	3913.40	549.37	538.36
	Mean	1884.21	1999.71	754.93	2417.94	2377.69	1846.56	1735.53	3901.56	435.45	457.92
	SD	143.55	114.86	27.79	129.36	162.05	8.82	29.68	53.28	107.57	98.59
CAD	1	2173.78	2173.14	710.08	2512.84	2508.53	1815.27	1732.96	3773.05	368.96	373.54
	M_{PE} (%)	13.32	7.98	-6.32	3.78	5.22	-1.72	-0.15	-3.41	-18.02	-22.59

Valleys measurements											
	Meas#	**r'1,V**	**r'2,V**	**si,V**	**s1,V**	**s2,V**	**sPA1,V**	**sPA2,V**	**arcV**	**l1,V**	**l2,V**
REAL	1	2095.18	1666.30	639.68	1868.19	1894.55	1851.63	1900.95	3814.28	792.53	656.45
	2	2079.31	1987.27	639.68	1893.64	1732.67	1909.83	1733.86	3800.96	727.67	638.99
	3	2393.20	2258.65	553.23	1876.31	1821.23	1861.73	1793.39	3626.94	986.39	889.77
	Mean	2189.23	1970.74	610.86	1879.38	1816.15	1874.40	1809.40	3747.39	835.53	728.40
	SD	176.82	296.52	49.91	13.00	81.06	31.10	84.69	104.53	134.61	140.02
CAD	1	2453.70	2455.58	577.80	1857.34	1869.41	1815.27	1732.61	3653.10	844.40	824.90
	M_{PE} (%)	10.78	19.74	-5.72	-1.19	2.85	-3.26	-4.43	-2.58	1.05	11.70

Geometrical Parameters RF=0.74											
Peaks measurements											
	Meas#	**r'1,P**	**r'2,P**	**si,P**	**s1,P**	**s2,P**	**sPA1,P**	**sPA2,P**	**arcP**	**l1,P**	**l2,P**
REAL	1	2044.80	1999.25	829.85	2481.65	2331.27	1913.83	1727.26	3460.71	448.72	518.83
	2	1956.78	1980.91	829.85	2453.26	2460.88	1864.04	1748.99	3423.04	610.22	702.65
	3	1843.65	1930.68	899.85	2406.09	2390.02	1827.35	1756.54	3427.05	609.43	707.45
	Mean	1948.41	1970.28	853.18	2447.00	2394.06	1868.41	1744.26	3436.93	556.12	642.98
	SD	100.84	35.50	40.41	38.17	64.90	43.41	15.20	20.69	93.01	107.54
CAD	1	2173.78	2173.14	843.42	2512.84	2508.53	1815.27	1732.96	3494.55	502.29	506.87
	M_{PE} (%)	10.37	9.33	-1.16	2.62	4.56	-2.93	-0.65	1.65	-10.72	-26.85

Valleys measurements											
	Meas#	**r'1,V**	**r'2,V**	**si,V**	**s1,V**	**s2,V**	**sPA1,V**	**sPA2,V**	**arcV**	**l1,V**	**l2,V**
REAL	1	2064.31	2149.35	899.01	1870.29	1712.57	1885.14	1682.04	3703.44	877.00	801.23
	2	2457.63	2458.85	622.39	1894.36	1911.09	1839.71	1799.86	3562.02	872.50	885.46
	3	2277.95	2257.50	855.78	1962.17	1809.93	1856.07	1739.69	3725.26	899.96	807.23
	Mean	2266.63	2288.57	792.39	1908.94	1811.20	1860.31	1740.53	3663.57	883.15	831.31
	SD	196.90	157.07	148.81	47.64	99.27	23.01	58.91	88.62	14.73	46.99
CAD	1	2453.70	2455.58	674.91	1857.34	1869.41	1815.27	1732.61	3652.71	958.31	940.19
	M_{PE} (%)	7.62	6.80	-17.41	-2.78	3.11	-2.48	-0.46	-0.30	7.84	11.58

Figure S14: **Microscope characterization of 3D printed peaks and valleys from case C8 (scale 3:1) with 0.74 ≤ RF ≤ 0.80.** Mean values, and standard deviation (SD) of the real measurements, besides the mean percentage error $M_{PE}(\%)$ with respect to the exact (CAD) measurements. Units: microns.

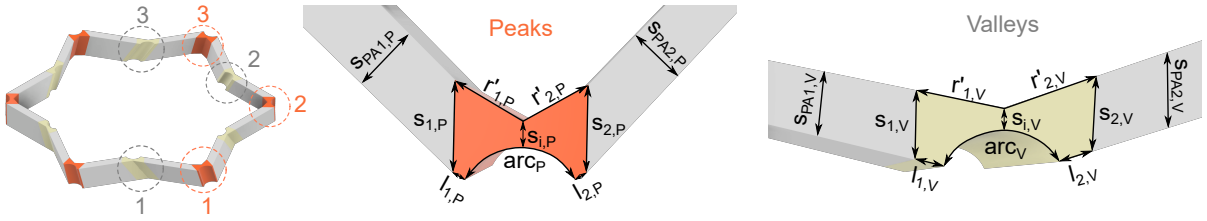

Geometrical Parameters RF=0.66											
Peaks measurements											
	Meas#	**r'1,P**	**r'2,P**	**si,P**	**s1,P**	**s2,P**	**sPA1,P**	**sPA2,P**	**arcP**	**l1,P**	**l2,P**
REAL	1	1925.05	1952.67	1089.18	2355.76	2441.13	1882.14	1701.58	3306.21	592.87	661.01
	2	1762.63	1897.89	1097.82	2367.57	2346.68	1840.89	1818.57	3144.04	656.89	707.30
	3	2076.20	2037.56	976.80	2358.92	2403.50	1846.38	1773.73	2918.37	746.48	754.29
	Mean	1921.29	1962.71	1054.60	2360.75	2397.10	1856.47	1764.63	3122.87	665.41	707.53
	SD	156.82	70.37	67.52	6.11	47.55	22.40	59.02	194.78	77.16	46.64
CAD	1	2173.78	2173.14	843.42	2512.84	2508.53	1815.27	1732.96	3494.55	502.29	506.87
	M_{PE} (%)	11.61	9.68	-25.04	6.05	4.44	-2.27	-1.83	10.64	-32.48	-39.59
Valleys measurements											
	Meas#	**r'1,V**	**r'2,V**	**si,V**	**s1,V**	**s2,V**	**sPA1,V**	**sPA2,V**	**arcV**	**l1,V**	**l2,V**
REAL	1	2276.31	2216.95	812.56	1870.04	1810.70	1858.39	1766.07	3234.99	987.65	735.99
	2	2200.04	2255.46	924.94	1816.62	1842.53	1738.40	1790.08	3205.89	914.09	880.13
	3	2299.29	2135.98	726.12	1771.06	1696.32	1777.74	1736.65	3083.61	1163.36	1060.41
	Mean	2258.55	2202.80	821.21	1819.24	1783.18	1791.51	1764.27	3174.83	1021.70	892.18
	SD	51.95	60.98	99.69	49.54	76.89	61.17	26.76	80.33	128.08	162.55
CAD	1	2453.70	2455.58	791.14	1857.33	1869.41	1815.27	1732.61	3044.68	1100.72	1084.35
	M_{PE} (%)	7.95	10.29	-3.80	2.05	4.61	1.31	-1.83	-4.27	7.18	17.72

Geometrical Parameters RF=0.57											
Peaks measurements											
	Meas#	**r'1,P**	**r'2,P**	**si,P**	**s1,P**	**s2,P**	**sPA1,P**	**sPA2,P**	**arcP**	**l1,P**	**l2,P**
REAL	1	1843.58	1878.57	1262.07	2383.19	2311.19	1788.05	1730.54	2845.25	843.64	920.16
	2	1951.89	2039.94	1244.78	2474.39	2412.00	1804.26	1770.34	2813.76	815.30	898.31
	3	2072.20	2191.38	1236.13	2409.32	2481.15	1818.14	1762.74	2531.63	910.13	947.11
	Mean	1955.89	2036.63	1247.66	2422.30	2401.45	1803.48	1754.54	2730.21	856.36	921.86
	SD	114.36	156.43	13.21	46.97	85.47	15.06	21.13	172.70	48.68	24.44
CAD	1	2173.78	2173.14	1224.37	2512.84	2508.53	1815.27	1732.96	2697.78	883.24	887.84
	M_{PE} (%)	10.02	6.28	-1.90	3.60	4.27	0.65	-1.25	-1.20	3.04	-3.83
Valleys measurements											
	Meas#	**r'1,V**	**r'2,V**	**si,V**	**s1,V**	**s2,V**	**sPA1,V**	**sPA2,V**	**arcV**	**l1,V**	**l2,V**
REAL	1	2430.01	2413.36	847.14	1888.91	1806.66	1823.66	1801.08	2723.95	1423.84	1265.66
	2	2266.27	2237.62	847.14	1888.21	1807.67	1846.33	1794.40	2855.89	1149.21	1090.58
	3	2438.34	2431.34	838.50	1886.06	1764.47	1839.21	1766.05	2811.48	1354.00	1246.38
	Mean	2378.21	2360.77	844.26	1887.73	1792.93	1836.40	1787.18	2797.11	1309.02	1200.87
	SD	97.03	107.03	4.99	1.49	24.66	11.59	18.60	67.13	142.73	96.00
CAD	1	2453.70	2455.58	946.48	1857.34	1869.41	1815.27	1732.61	2609.96	1283.88	1269.77
	M_{PE} (%)	3.08	3.86	10.80	-1.64	4.09	-1.16	-3.15	-7.17	-1.96	5.43

Figure S15: **Microscope characterization of 3D printed peaks and valleys from case C8 (scale 3:1) with 0.57 ≤ RF ≤ 0.66.** Mean values, and standard deviation (SD) of the real measurements, besides the mean percentage error $M_{PE}(\%)$ with respect to the exact (CAD) measurements. Units: microns.

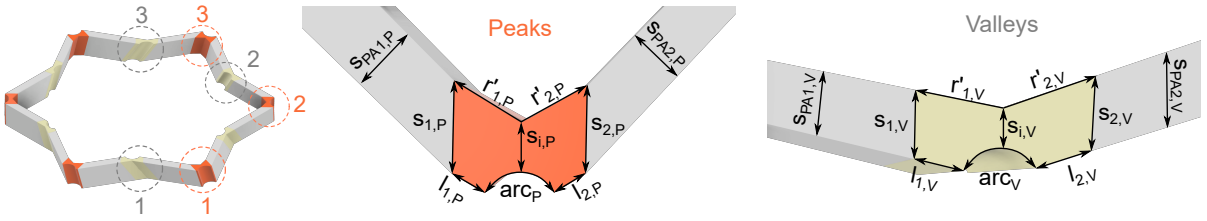

Geometrical Parameters RF=0.50

Peaks measurements

	Meas#	$r'_{1,P}$	$r'_{2,P}$	$s_{i,P}$	$s_{1,P}$	$s_{2,P}$	$s_{PA1,P}$	$s_{PA2,P}$	arc_P	$l_{1,P}$	$l_{2,P}$
REAL	1	1938.23	1904.66	1296.64	2318.11	2340.35	1784.59	1781.64	2361.64	987.28	1017.38
	2	1975.79	2093.31	1297.49	2412.80	2448.53	1837.37	1773.89	2472.90	978.77	1082.89
	3	2038.33	2035.59	1327.49	2436.15	2402.00	1904.94	1810.34	2531.46	942.40	1078.77
	Mean	1984.12	2011.19	1307.21	2389.02	2396.96	1842.30	1788.62	2455.33	969.48	1059.68
	SD	50.57	96.66	17.57	62.51	54.27	60.33	19.20	86.26	23.84	36.69
CAD	1	2173.78	2173.14	1434.00	2512.84	2508.53	1815.27	1732.95	2361.35	1043.96	1048.55
	M_{PE} (%)	8.72	7.45	8.84	4.93	4.45	-1.49	-3.21	-3.98	7.13	-1.06

Valleys measurements

	Meas#	$r'_{1,V}$	$r'_{2,V}$	$s_{i,V}$	$s_{1,V}$	$s_{2,V}$	$s_{PA1,V}$	$s_{PA2,V}$	arc_V	$l_{1,V}$	$l_{2,V}$
REAL	1	2322.80	2075.29	985.45	1767.51	1769.52	1807.56	1783.69	2401.85	1563.69	1661.65
	2	2324.10	2312.17	1100.89	1826.11	1806.05	1837.07	1812.26	2260.21	1538.72	1469.46
	3	2152.60	2078.57	950.87	1866.78	1746.68	1827.55	1724.35	2407.22	1193.45	1197.10
	Mean	2266.50	2155.34	1012.40	1820.13	1774.08	1824.06	1773.43	2356.43	1431.95	1442.74
	SD	98.64	135.83	78.56	49.90	29.95	15.06	44.84	83.37	206.93	233.43
CAD	1	2453.70	2455.58	1058.19	1857.34	1869.41	1815.27	1732.61	2283.87	1421.29	1408.90
	M_{PE} (%)	7.63	12.23	4.33	2.00	5.10	-0.48	-2.36	-3.18	-0.75	-2.40

Geometrical Parameters RF=0.40

Peaks measurements

	Meas#	$r'_{1,P}$	$r'_{2,P}$	$s_{i,P}$	$s_{1,P}$	$s_{2,P}$	$s_{PA1,P}$	$s_{PA2,P}$	arc_P	$l_{1,P}$	$l_{2,P}$
REAL	1	1825.07	1936.91	1547.33	2324.26	2263.44	1799.77	1714.02	2053.97	1205.87	1207.09
	2	2018.29	2079.35	1538.68	2382.63	2377.57	1818.97	1730.74	2040.43	1236.40	1260.02
	3	1992.82	1978.89	1555.97	2281.62	2336.26	1842.91	1790.18	1869.76	1337.59	1353.99
	Mean	1945.39	1998.38	1547.33	2329.50	2325.76	1820.55	1744.98	1988.05	1259.95	1273.70
	SD	104.98	73.19	8.65	50.71	57.79	21.61	40.03	102.67	68.95	74.40
CAD	1	2173.78	2173.14	1610.08	2512.84	2508.53	1815.27	1732.96	1889.97	1268.96	1273.56
	M_{PE} (%)	10.51	8.04	3.90	7.30	7.29	-0.29	-0.69	-5.19	0.71	-0.01

Valleys measurements

	Meas#	$r'_{1,V}$	$r'_{2,V}$	$s_{i,V}$	$s_{1,V}$	$s_{2,V}$	$s_{PA1,V}$	$s_{PA2,V}$	arc_V	$l_{1,V}$	$l_{2,V}$
REAL	1	2408.36	2429.37	1296.64	1822.79	1793.45	1820.92	1740.57	2044.27	1532.16	1569.42
	2	2276.83	2280.70	1262.07	1798.03	1792.89	1799.84	1740.85	1797.87	1433.65	1416.88
	3	2267.32	2228.39	1322.58	1807.67	1799.34	1788.70	1746.69	1589.70	1479.77	1414.80
	Mean	2317.50	2312.82	1293.76	1809.50	1795.23	1803.15	1742.70	1810.61	1481.86	1467.03
	SD	78.83	104.27	30.36	12.48	3.57	16.36	3.46	227.55	49.29	88.68
CAD	1	2453.70	2455.58	1214.91	1857.34	1869.41	1815.27	1732.61	1827.24	1613.72	1603.74
	M_{PE} (%)	5.55	5.81	-6.49	2.58	3.97	0.67	-0.58	0.91	8.17	8.52

Figure S16: **Microscope characterization of 3D printed peaks and valleys from case C8 (scale 3:1) with 0.40 ≤ RF ≤0.50.** Mean values, and standard deviation (SD) of the real measurements, besides the mean percentage error $M_{PE}(\%)$ with respect to the exact (CAD) measurements. Units: microns.

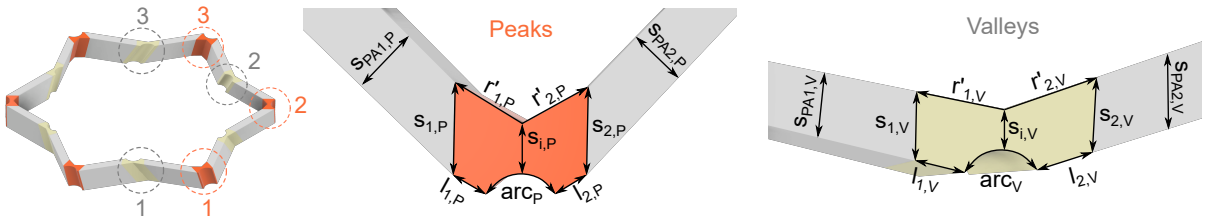

Geometrical Parameters RF=0.33

Peaks measurements

	Meas#	$r'_{1,P}$	$r'_{2,P}$	$s_{i,P}$	$s_{1,P}$	$s_{2,P}$	$s_{PA1,P}$	$s_{PA2,P}$	arc_P	$l_{1,P}$	$l_{2,P}$
REAL	1	2007.90	2155.04	1590.55	2333.07	2430.29	1859.66	1726.92	1846.22	1322.36	1490.03
	2	2028.15	2180.96	1694.28	2323.11	2403.11	1828.61	1707.10	1693.91	1380.78	1442.26
	3	2092.83	2118.11	1633.77	2312.08	2334.74	1848.64	1697.99	1580.72	1468.83	1542.94
	Mean	2042.96	2151.37	1639.53	2322.75	2389.38	1845.64	1710.67	1706.95	1390.66	1491.74
	SD	44.36	31.59	52.10	10.50	49.23	15.74	14.79	133.23	73.73	50.36
CAD	1	2173.78	2173.14	1760.09	2512.84	2508.53	1815.27	1732.96	1575.47	1418.96	1423.56
	M_{PE} (%)	6.02	1.00	6.85	7.56	4.75	-1.67	1.29	-8.35	1.99	-4.79

Valleys measurements

	Meas#	$r'_{1,V}$	$r'_{2,V}$	$s_{i,V}$	$s_{1,V}$	$s_{2,V}$	$s_{PA1,V}$	$s_{PA2,V}$	arc_V	$l_{1,V}$	$l_{2,V}$
REAL	1	2342.48	2213.98	1495.46	1748.28	1824.03	1720.14	1731.25	1467.53	1701.94	1518.26
	2	2245.91	2181.91	1538.68	1837.17	1711.47	1798.85	1711.47	1433.87	1951.36	1710.22
	3	2350.44	2343.54	1495.46	1730.69	1711.92	1750.96	1664.61	1075.60	1941.09	1873.85
	Mean	2312.94	2246.48	1509.87	1772.05	1749.14	1756.65	1702.44	1325.67	1864.80	1700.78
	SD	58.19	85.58	24.95	57.08	64.86	39.66	34.22	217.22	141.13	177.98
CAD	1	2453.70	2455.58	1318.87	1857.34	1869.41	1815.27	1732.61	1522.77	1742.04	1733.69
	M_{PE} (%)	5.74	8.52	-14.48	4.59	6.43	3.23	1.74	12.94	-7.05	1.90

Geometrical Parameters RF=0.25

Peaks measurements

	Meas#	$r'_{1,P}$	$r'_{2,P}$	$s_{i,P}$	$s_{1,P}$	$s_{2,P}$	$s_{PA1,P}$	$s_{PA2,P}$	arc_P	$l_{1,P}$	$l_{2,P}$
REAL	1	2090.82	2177.36	1970.90	2370.55	2333.97	1846.06	1729.49	805.27	1798.33	1948.19
	2	2136.14	2273.04	1823.94	2385.47	2560.47	1860.38	1773.35	1032.96	1676.56	1690.60
	3	2012.82	2091.49	1875.81	2412.80	2424.35	1807.23	1716.87	1280.27	1580.28	1665.81
	Mean	2079.93	2180.63	1890.22	2389.61	2439.60	1837.89	1739.90	1039.50	1685.06	1768.20
	SD	62.38	90.82	74.53	21.43	114.02	37.50	29.64	237.57	109.27	156.37
CAD	1	2173.78	2173.14	1947.58	2512.84	2508.53	1815.27	1732.96	1182.07	1606.46	1611.07
	M_{PE} (%)	4.32	-0.34	2.95	4.90	2.75	-1.25	-0.40	12.06	-4.89	-9.75

Valleys measurements

	Meas#	$r'_{1,V}$	$r'_{2,V}$	$s_{i,V}$	$s_{1,V}$	$s_{2,V}$	$s_{PA1,V}$	$s_{PA2,V}$	arc_V	$l_{1,V}$	$l_{2,V}$
REAL	1	2381.80	2225.93	1504.11	1817.79	1776.20	1804.06	1740.32	1346.03	1662.17	1605.54
	2	2244.79	2173.83	1513.93	1691.98	1675.51	1732.54	1718.32	1351.15	1855.47	1924.44
	3	2293.10	2291.09	1555.97	1758.96	1720.56	1808.49	1714.21	1307.83	1803.89	1740.83
	Mean	2306.56	2230.28	1524.67	1756.24	1724.09	1781.70	1724.28	1335.00	1773.84	1756.94
	SD	69.49	58.75	27.55	62.95	50.44	42.63	14.04	23.67	100.09	160.06
CAD	1	2453.70	2455.58	1449.74	1857.33	1869.41	1815.27	1732.61	1142.11	1902.48	1896.18
	M_{PE} (%)	6.00	9.17	-5.17	5.44	7.77	1.85	0.48	-16.89	6.76	7.34

Figure S17: **Microscope characterization of 3D printed peaks and valleys from case C8 (scale 3:1) with 0.25** $\leq RF \leq$**0.33** Mean values, and standard deviation (SD) of the real measurements, besides the mean percentage error $M_{PE}(\%)$ with respect to the exact (CAD) measurements. Units: microns.

S.2 Supplementary Text

S.2.1 Intact Kresling cell 3D analysis

Based on the initial geometrical configuration that leads to bistability, we parametrically designed the 3D Kresling cells, as further detailed in S.1.2. The analyzed group of intact cases was conformed by Kresling cells with a variable width of the creases. This term is expressed in terms of the width versus thickness ratio, denoted as w/s. Thus, the number of intact cases analyzed ranged within ($0.50 \leq w/s \leq 2.00$) with their respective notation: Int 1 to Int 11, as shown in Fig. S18A.

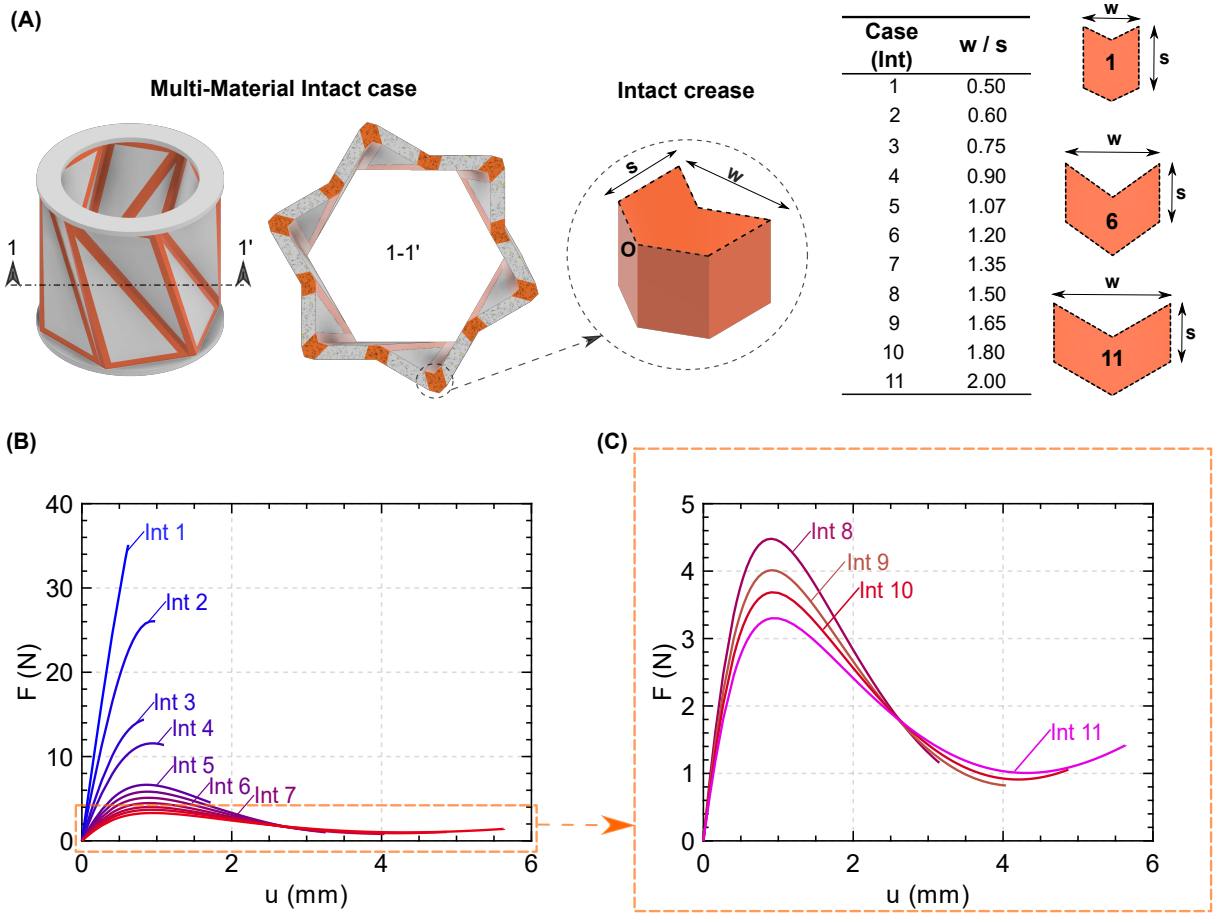

Figure S18: **Kresling cells with intact creases analysis (A)** Geometrical details of Intact creases cases, from Int 1 to Int 11, defined in terms of the ratio w/s. Load paths within the ranges: **(B)** $0.50 \leq w/s \leq 2.00$ and **(C)** $1.50 \leq w/s \leq 2.00$.

The load paths obtained from the numerical simulations, depicted in Fig. S18B, reveal that despite the utilization of flexible creases, the intact cases did not achieved the theoretical bistability as predicted by the preliminary five-parameters model assessment. Specifically, the force values did

not reached values below zero, preventing a second local minimum energy state. We have observed that the intact cases with narrower creases (Int 1 to 4) ranging between ($0.50 \leq w/s \leq 0.90$), tended towards monostability and become highly stiff instead. In contrast, the intact cases (Int 5 to 11) with wider width creases ($1.07 \leq w/s \leq 2.00$), exhibited a monostable behavior. Although using flexible creases facilitates the folding process, the Kresling cell quickly reverts to its initial configuration once the axial load is applied, and second stable state is still not achieved, as evidenced by the load paths in Fig. S2C. This behavior can be attributed to the restoring force related to the viscoelastic nature of photopolymers. Therefore, these initial results indicate that utilizing elastomeric creases requires further design strategies to potentially achieve a bistable configuration in practice.

S.2.2 Creases design: Complementary results

The parametric study of the Kresling cells with the creases design, results from the numerical simulations in Abaqus/CAE Standard, shown in Fig. S19. We assessed how the gradual reductions creases affected the energy landscape and the transition form a bistable (Bi) to a monostable (M) behavior. As narrower the internal thickness s_i, the Kresling cell tends to achieve bistability.

This is especially observed in wider creases with a ratio $w/s \geq 1.20$, with an internal thickness s_i and reduction factors between $0.66 \leq RF \leq 0.80$, taking values between $0.58 \geq s_i/s \geq 0.05$. It is evidenced in the load paths with their corresponding stored energy landscapes, U, from Fig. S20 to Fig. S23. Moreover, the sequential experiments conducted on the Kresling cells within the range potentially exhibiting bistability ($0.66 \leq RF \leq 0.80$) are presented in Fig. S24. The results reveal a loss of load capacity of approximately 50% due to the degradation of the thin rubbery creases (RF=0.80). In contrast, thicker creases (RF=0.66) appeared more resistant, losing around 30% of load capacity. The analyzed Kresling cell cases were designed according to the geometrical parameters detailed in Fig. S25 for a 1:1 scale.

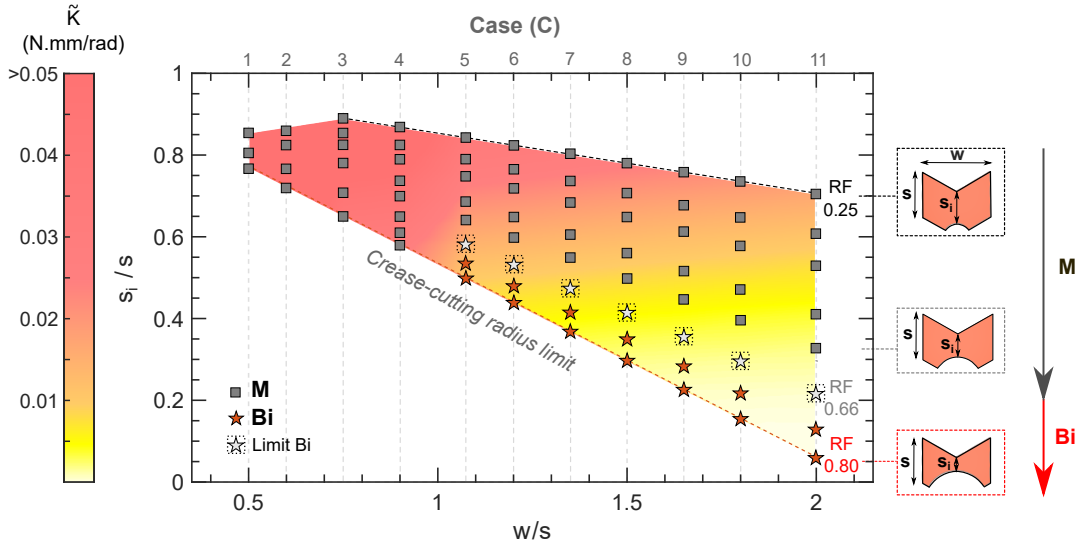

Figure S19: **Parametric study of the creases geometry.** Geometrical parameters with their attained Rotational Stiffness ($\tilde{K}$), that lead to monostability (M) or bistability (Bi). 'Limit Bi': boundary between (Bi) and (M) determined experimentally. *The crease edge limit determines the range of reduction radius factors, RF, to maintain a Circular shape at the lower part of the crease. Results from Kresling cells at 1:1 scale.

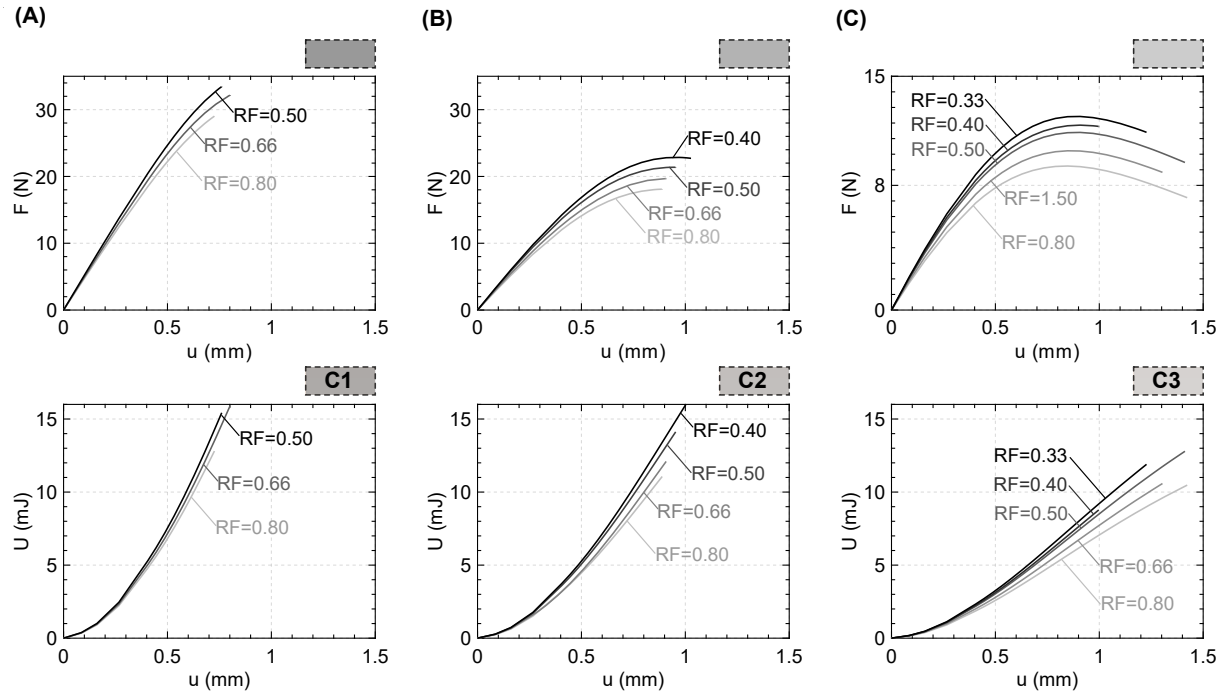

Figure S20: **Load paths and stored energy (U) landscapes variation according to the crease internal thickness (s_i) decrement based on the reduction factors RF. (A)** C1 ($w/s = 0.50$), **(B)** C2 ($w/s = 0.60$) and **(C)** C3 ($w/s = 0.75$). The corresponding curves were generated until the panels started to be in contact during the numerical simulations.

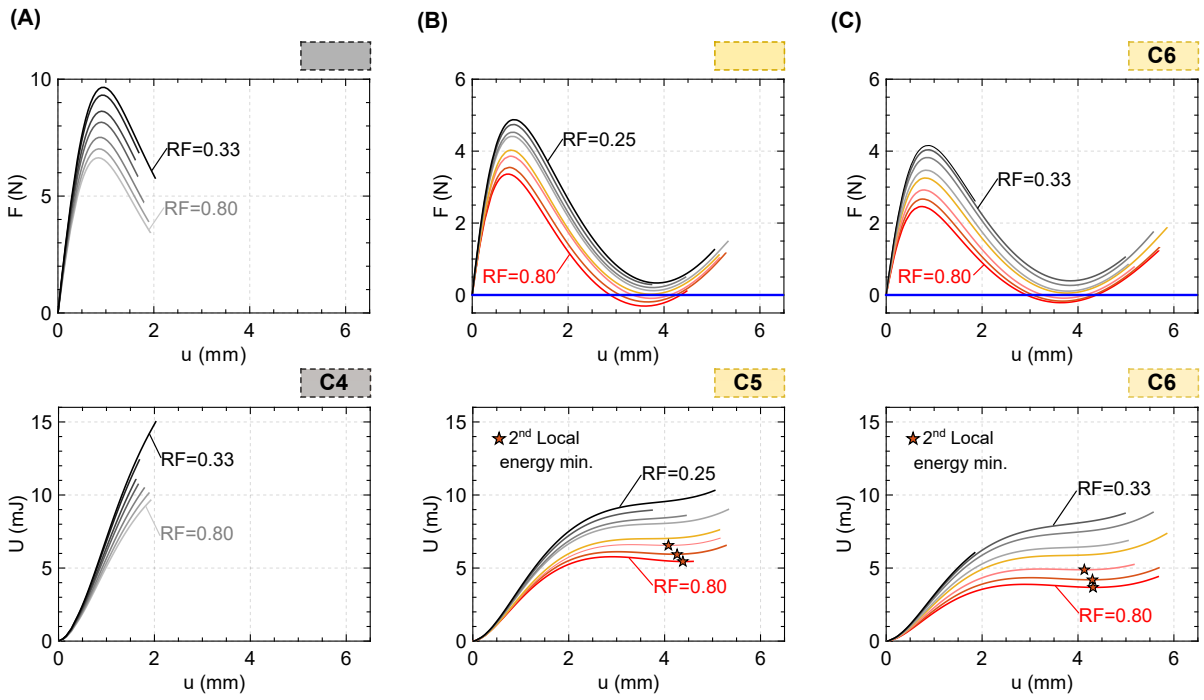

Figure S21: **Load paths and stored energy (U) landscapes variation according to the reduction factors RF. (A)** C4 (w/s = 0.90), **(B)** C5 (w/s = 1.07), and **(C)** C6 (w/s = 1.20). The corresponding curves are presented in the following order RF: 0.25, 0.33, 0.40, 0.50, 0.57, 0.66, 0.74, and 0.80.

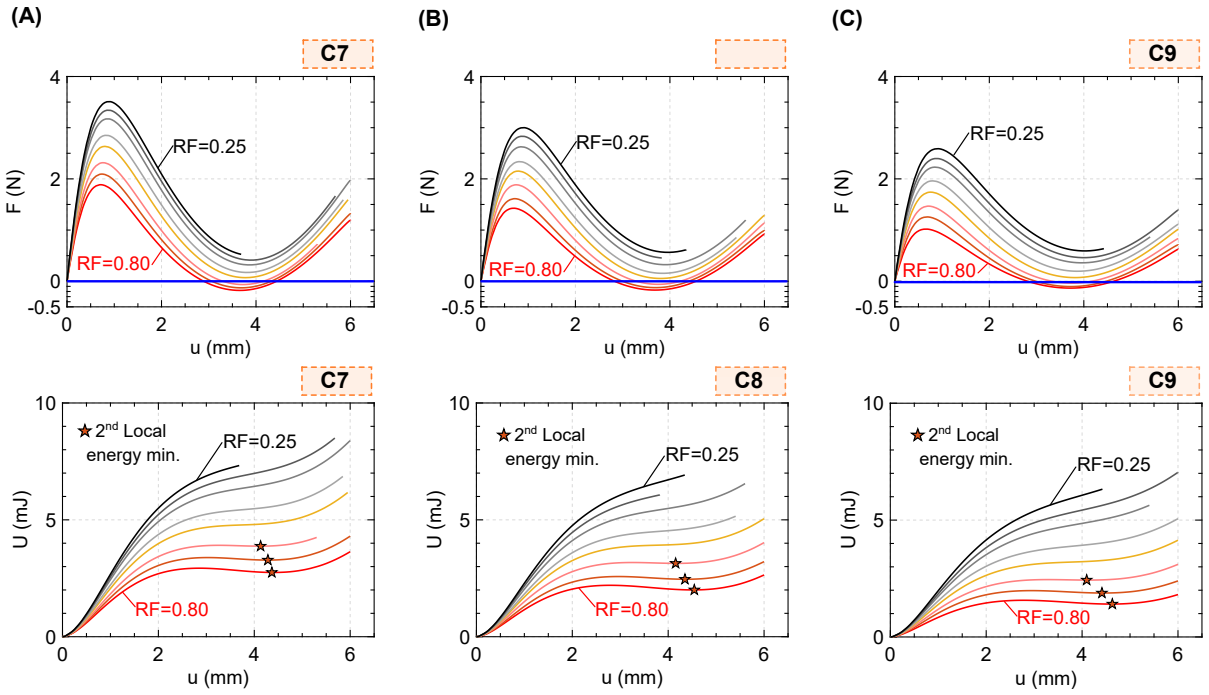

Figure S22: **Load paths and stored energy (U) landscapes variation according to the reduction factors RF. (A)** C7 (w/s = 1.35), **(B)** C8 (w/s = 1.50) and **(C)** C9 (w/s = 1.65). The corresponding curves are presented in the following order RF: 0.25, 0.33, 0.40, 0.50, 0.57, 0.66, 0.74, and 0.80.

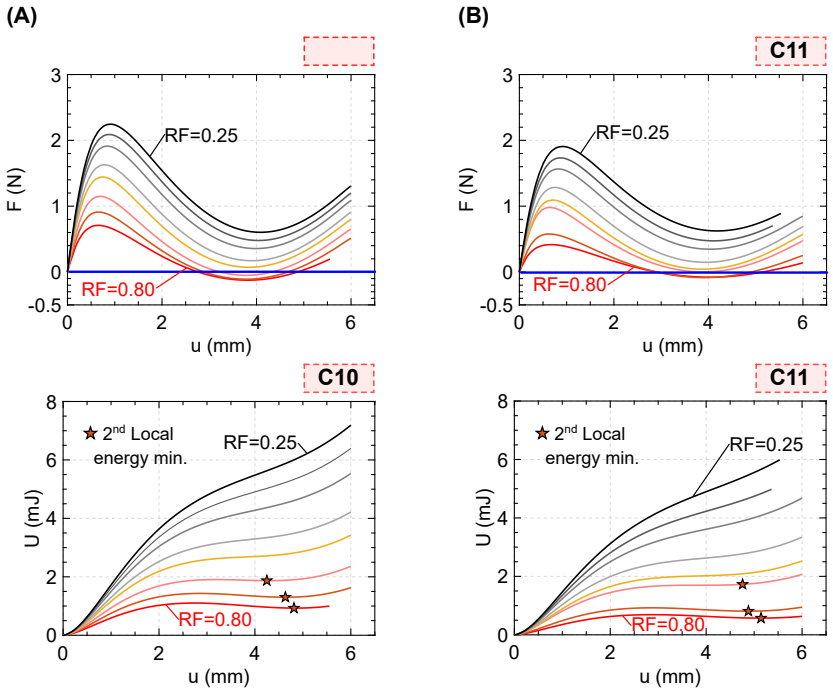

Figure S23: **Load paths and stored energy (U) landscapes variation according to the reduction factors. (A)** C10 (w/s = 1.80), and **(B)** C11 (w/s = 2.00). The corresponding curves are presented in the following order RF: 0.80, 0.74, 0.66, 0.57, 0.50, 0.40, 0.33, and 0.25.

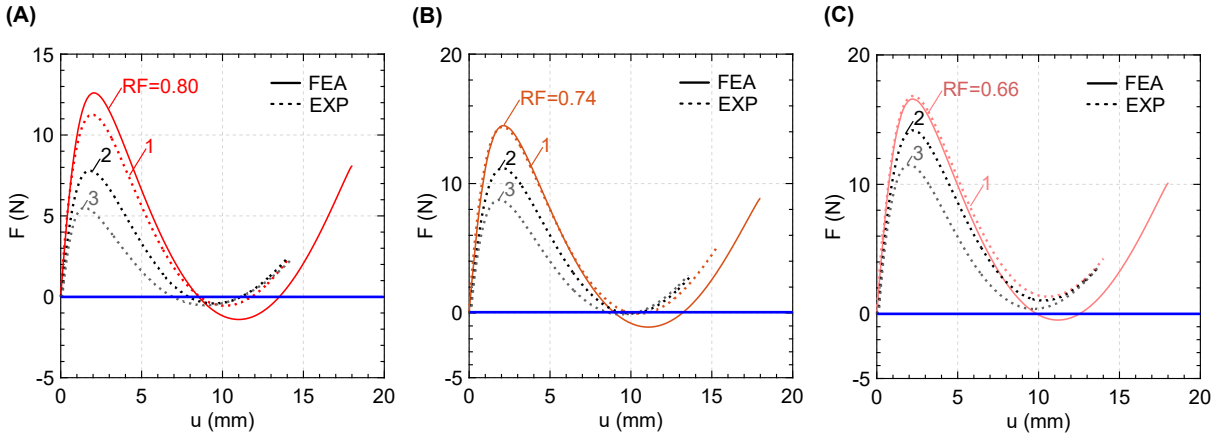

Figure S24: **Effect of the degradation of the rubbery crease cross- sections on the load path after performing sequential experiments on the same samples. (A)** RF=0.80, **(B)** RF=0.74 and **(C)** RF=0.66. Kresling cells case C8 fabricated with creases made of DM60, at 3:1 scale.

Geometrical Parameters							
Case #	w/s	s	r'	RF	s_c	s_i	s_i/s
1	0.50	1.71	1.00	0.80	0.80	1.31	0.77
				0.66	0.66	1.38	0.81
				0.50	0.50	1.46	0.85
2	0.60	1.43	1.00	0.80	0.80	1.03	0.72
				0.66	0.66	1.10	0.77
				0.50	0.50	1.18	0.82
				0.40	0.40	1.23	0.86
3	0.75	1.14	1.00	0.80	0.80	0.74	0.65
				0.66	0.66	0.81	0.71
				0.50	0.50	0.89	0.78
				0.40	0.40	0.94	0.83
				0.33	0.33	0.98	0.85
				0.25	0.25	1.02	0.89
4	0.90	1.14	1.20	0.80	0.96	0.66	0.58
				0.74	0.89	0.70	0.61
				0.66	0.79	0.74	0.65
				0.57	0.68	0.80	0.70
				0.50	0.60	0.84	0.74
				0.40	0.48	0.90	0.79
				0.33	0.40	0.94	0.82
				0.25	0.30	0.99	0.87
5	1.07	0.86	1.08	0.80	0.86	0.43	0.50
				0.74	0.80	0.46	0.53
				0.66	0.71	0.50	0.58
				0.57	0.61	0.55	0.64
				0.50	0.54	0.59	0.69
				0.40	0.43	0.64	0.75
				0.33	0.35	0.68	0.79
				0.25	0.27	0.72	0.84
6	1.20	0.86	1.20	0.80	0.96	0.38	0.44
				0.74	0.89	0.41	0.48
				0.66	0.79	0.46	0.53
				0.57	0.69	0.51	0.60
				0.50	0.60	0.56	0.65
				0.40	0.48	0.62	0.72
				0.33	0.40	0.66	0.77
				0.25	0.30	0.71	0.82
7	1.35	0.85	1.35	0.80	1.08	0.31	0.37
				0.74	1.00	0.35	0.41
				0.66	0.89	0.40	0.47
				0.57	0.77	0.47	0.55
				0.50	0.68	0.52	0.61
				0.40	0.54	0.58	0.68
				0.33	0.45	0.63	0.74
				0.25	0.34	0.69	0.80

Geometrical Parameters							
Case #	w/s	s	r'	RF	s_c	s_i	s_i/s
8	1.50	0.85	1.50	0.80	1.20	0.25	0.30
				0.74	1.11	0.30	0.35
				0.66	0.99	0.35	0.41
				0.57	0.86	0.42	0.50
				0.50	0.75	0.48	0.56
				0.40	0.60	0.55	0.65
				0.33	0.50	0.60	0.71
				0.25	0.38	0.67	0.78
9	1.65	0.85	1.65	0.80	1.32	0.19	0.23
				0.74	1.22	0.24	0.28
				0.66	1.09	0.30	0.35
				0.57	0.94	0.38	0.45
				0.50	0.83	0.44	0.52
				0.40	0.66	0.52	0.61
				0.33	0.54	0.58	0.68
				0.25	0.41	0.65	0.76
10	1.80	0.85	1.80	0.80	1.44	0.13	0.15
				0.74	1.33	0.18	0.22
				0.66	1.19	0.25	0.30
				0.57	1.03	0.34	0.40
				0.50	0.90	0.40	0.47
				0.40	0.72	0.49	0.58
				0.33	0.59	0.55	0.65
				0.25	0.45	0.63	0.74
11	2.00	0.85	2.00	0.80	1.60	0.05	0.06
				0.74	1.48	0.11	0.13
				0.66	1.32	0.18	0.22
				0.57	1.14	0.28	0.33
				0.50	1.00	0.35	0.41
				0.40	0.80	0.45	0.53
				0.33	0.66	0.52	0.61
				0.25	0.50	0.60	0.70

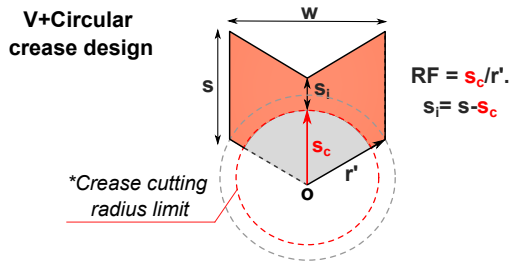

Figure S25: **Geometrical Parameters of creases with gradual reductions.** Dimensions taken from the top of the Kresling cells. Units: mm, scale: 1:1.

S.2.3 Estimation of Rotational Stiffness in Creases

Whether a rubbery material is considered for the design of the creases, large deformations are expected to be developed. The V-shape+Circular cross-section of the creases can be simplified into an equivalent rectangular strip that delimits the zone predominantly under bending. Its dimensions are the width w and the internal thickness s_i, where the latter varies according to a reduction factor RF. Thereby, we assessed the effects of the decrement of cross-sections on the rotational stiffness, $\tilde{K}$, of the designed creases. The angular rotation ψ, corresponding to a given bending moment M applied on the equivalent section, can be estimated considering the formulations of bending of an incompressible elastic Neo-Hookean block proposed by (*44*). This method assumes that the deformed configuration of the block follows the shape of a planar sector of a cylindrical tube with a thickness s_f, an initial angle ψ_i and a radius $\overline{r}$, as shown in Fig. S26A. The last two terms define the cylindrical coordinates of the system, thus: $\overline{r}\epsilon[\overline{r}_f, \overline{r}_f + s_f]$ and $\psi\epsilon f[-\psi_i, \psi_i]$, being the out of plane terms neglected. The term $\overline{r}$ can be calculated by fulfilling the impressibility constraint, where the deformed section is equal to the initial area defined by s_i and w. Then, the following relation can be established:

$$\overline{r}_f = \frac{w\ s_i}{2\ \psi_i\ s_f} - \frac{s_f}{2} \tag{S28}$$

Considering a Neo-Hookean response of the section, one of the principal stress components T_ψ in cylindrical form is defined as:

$$T_\psi(\overline{r}) = G_o\left(-\frac{w^2}{8\psi_i^2\overline{r}^2} + \frac{6\psi_i^2}{w^2}\overline{r}^2 - 1\right) - \frac{G_o}{2}\left(-\frac{w^2}{4\psi_i^2(\overline{r}_f + s_f)^2} + \frac{4\psi_i^2(\overline{r}_f + s_f)^2}{w^2} - 2\right). \tag{S29}$$

where, G_o is the initial shear modulus and the thickness s_f of the deformed configuration can be obtained by the following expression:

$$s_f = \frac{w}{\psi_i\sqrt{2}}\sqrt{-1 + \sqrt{1 + 4\psi_i^2\frac{s_i^2}{w}}} \tag{S30}$$

The bending moment M, corresponding to the stress on the deformed configuration, is calculated by the following integration in the interval $[\overline{r}_f, \overline{r}_f + s_f]$:

$$M = \int_{\overline{r}_f}^{\overline{r}_f + s_f} \overline{r}T_\psi(\overline{r})\, d\,\overline{r} \tag{S31}$$

Using Eq.S31, we calculated the bending moment M of the equivalent cross- sections, M, obtained at a given rotational angle ranging within $0 \leq \psi \leq \pi/2$. The analytical results of the creases from cases C8 ($w/s = 1.50$) and C11 ($w/s = 2.00$) were selected for validation against numerical simulations in Abaqus/CAE-Standard, as indicated in Fig. S26B and C, respectively. The thicknesses of the equivalent rectangular blocks correspond to the variable internal thickness s_i generated by reduction factors ranging from $0.25 \leq RF \leq 0.80$. Moreover, the corresponding mesh was created using biquadratic hybrid elements (CPE8RH). The equivalent rectangular blocks were subjected to bending until reaching a rotational angle of $\psi = \pi/2$ allowing us to obtain the corresponding bending moment M. This demonstrated the close alignment between the FEA calculations and the analytical formulation. Furthermore, the plots from Fig. S27 depict the bending moment values obtained in Eq.S31 at a given rotational angle $0 \leq \psi \leq \pi/2$, applied to the equivalent cross-sections corresponding to crease cases C1 to C11, along with their respective reduction factors RF, as well as the related intact crease cases.

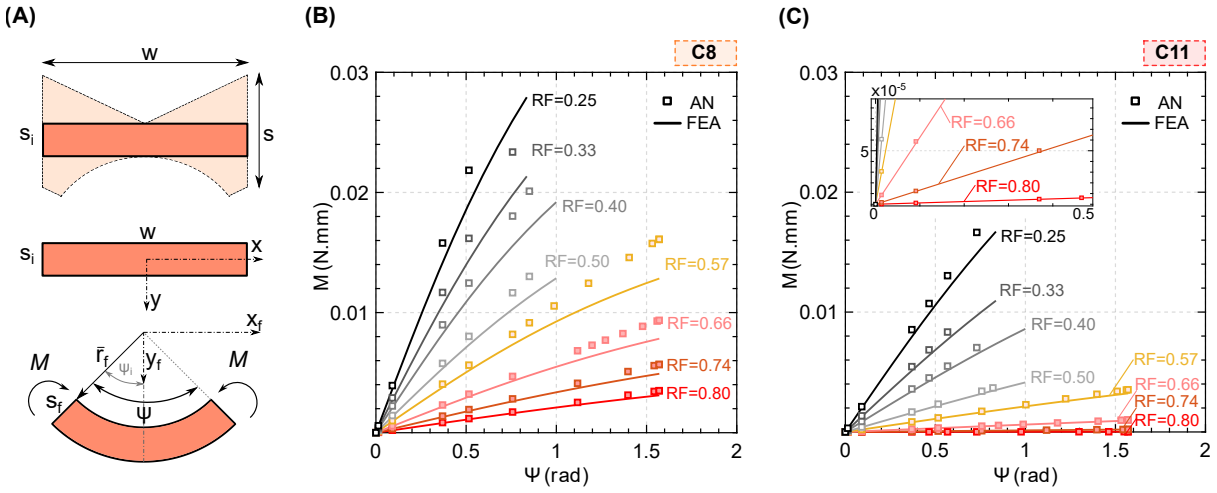

Figure S26: **Rotational stiffness calculation. (A)** Bending of an incompressible rectangular block equivalent to the crease cross-section. Comparison of analytical and FEA results for the bending moment, M, and angular rotation, ψ, in cases: **(B)** C8 ($w/s = 1.50$) and **(C)** C11 ($w/s = 2.00$). *Note: Results are presented in the order reduction factors ranging from $0.25 \leq RF \leq 0.80$, representing a variable s_i

Then, the rotational stiffness was obtained using the expression: $\tilde{K} = M/\psi$. We observed that rotational stiffness depends on the variation of internal thicknesses s_i, their associated reduction factors RF, and the width of the creases w. For instance, bistable creases with thinner internal thicknesses, generated by reduction factors $0.66 \leq RF \leq 0.80$ and ranges of $0.40 \geq s_i/s \geq 0.30$

(C8) and $0.21 \geq s_i/s \geq 0.05$ (C11), achieved the highest angular rotation value $\psi = \pi/2 \approx 1.57$ rad at lower bending moments. Consequently, they exhibited higher flexibility and lower rotational stiffness than their thicker creases counterparts, which fall within the ranges $s_i/s \geq 0.57$ (C8) and $s_i/s \geq 0.37$ (C11), as previously shown in Fig. S19.

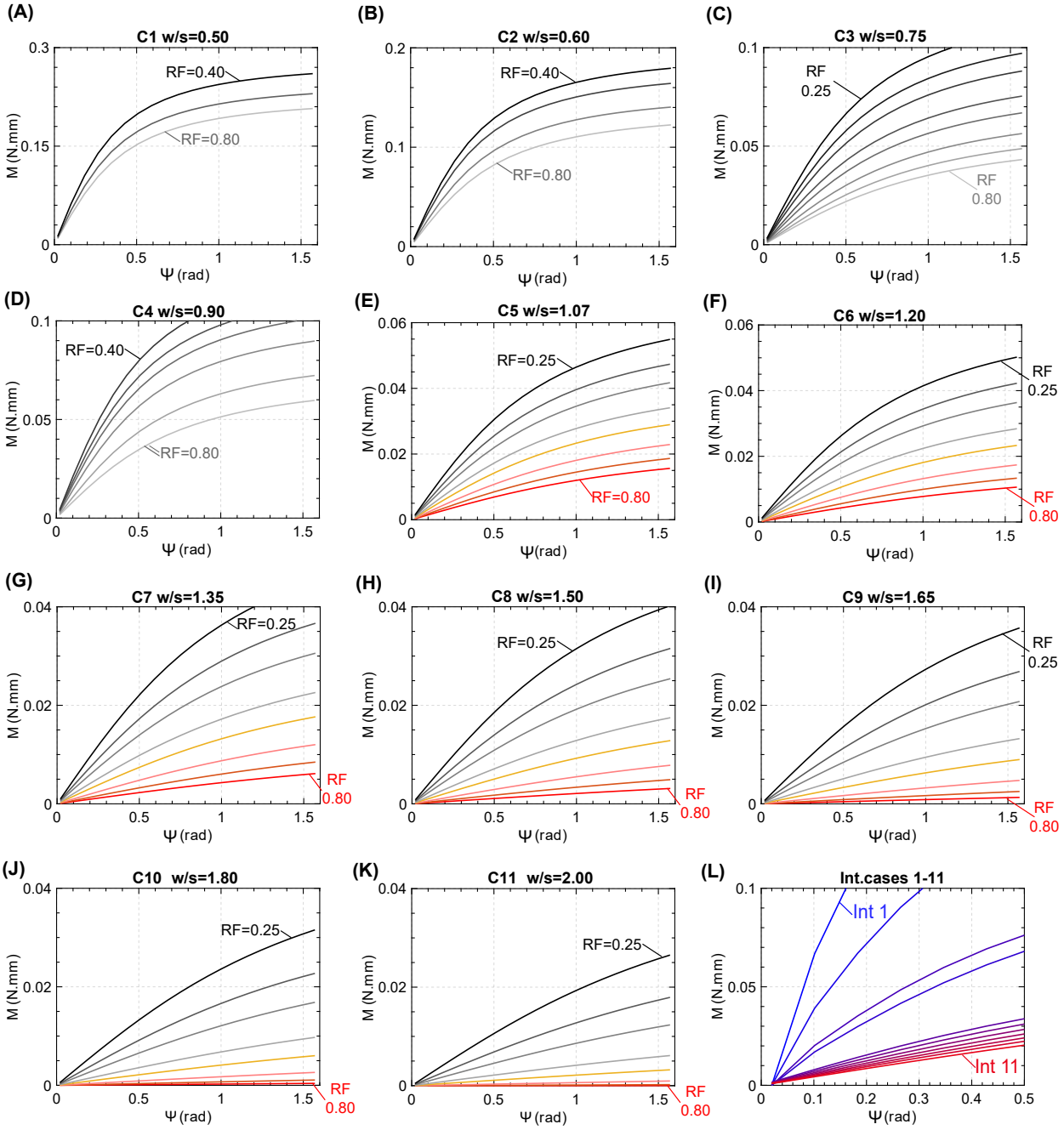

Figure S27: **Bending Moment M versus Rotational angle ψ curves.** Calculation obtained from the equivalent cross-sections of the cases C1 (A) to C11 (K), and Intact cases from 1 to 11.

S.2.4 Effects of creases viscosity on bistability: Complementary Results

The assessment of bistability in Kresling cells with creases made from different rubbery materials is presented in Fig. S28, which is constructed from the load paths and energy landscapes illustrated in Figs. S29-S32, based on analyses of Kreling cells at 1:1 scale (x1). We determined whether creases with varying viscosity and relaxation moduli can still achieve bistability, as explored in the parametric study in section 2.1. The numerical simulations were conducted for a time duration corresponding to the limits of the initial (τ_i^*), short- (τ), and long-term ($n\tau$) relaxation regions to predict whether viscosity effects influence the achievement of bistability at different time scales. Moreover, we conducted experiments on Kresling cells (C8 RF=0.80, fabricated at a 3:1 scale) with creases made of AG30, DM60, DM70, DM85, and DM95, as shown in Fig. S33. An average load capacity loss of approximately 50% was observed due to degradation of the crease cross-sections, with lower peak load decrements in softer photopolymers (AG30, DM60, and DM70) which have lower viscosity and relaxation moduli.

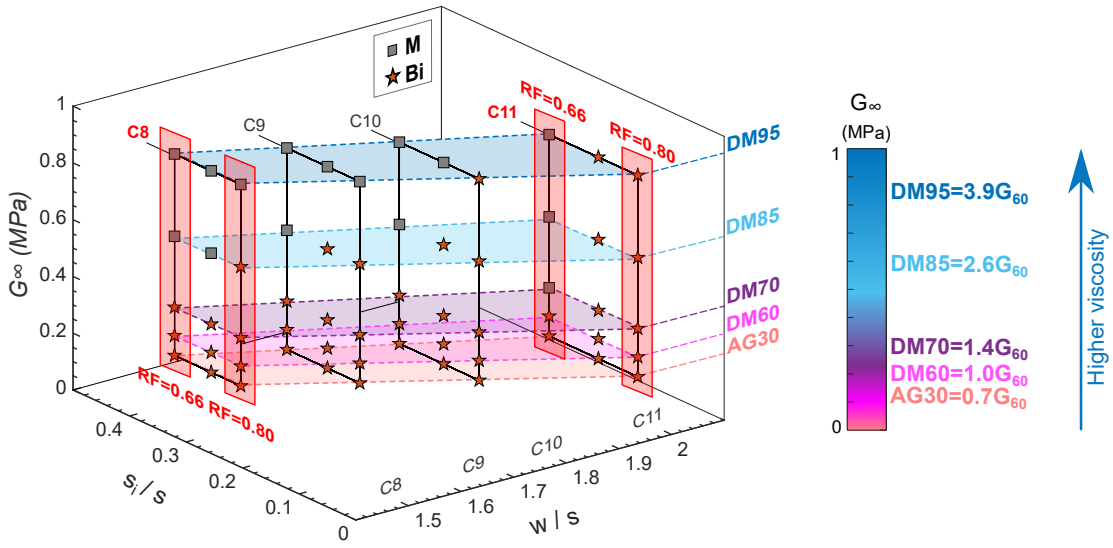

Figure S28: **Visco-hyperelastic effects on bistability.** Parametric study assessing the achievement of bistability in creases made of rubbery materials (AG30, DM60, DM70, DM85, and DM95) with varying visco-hyperelastic properties, characterized by relaxation modulus G_∞. Where G_{60} = 0.220 MPa. The study focuses on Cases C8, C9, C10, and C11, designed with reduction factors RF=0.80, RF=0.74 and RF=0.66.

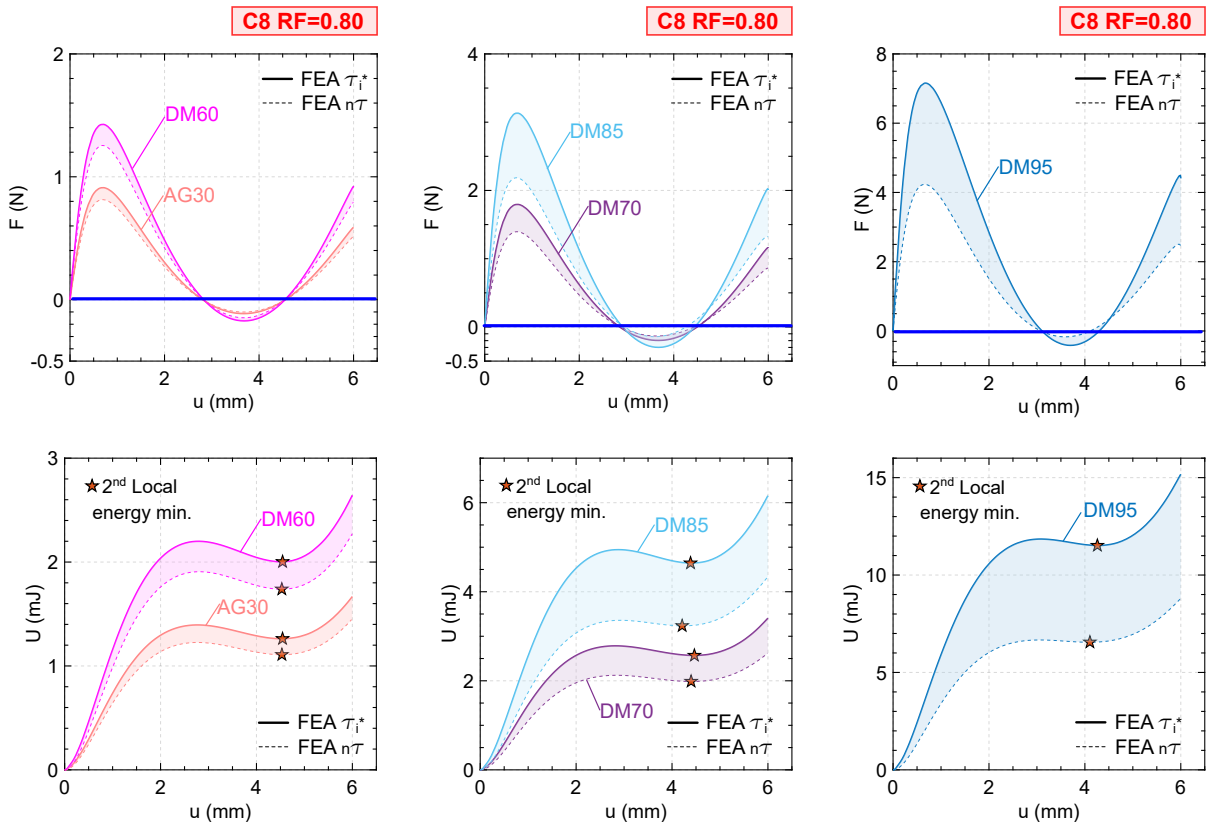

Figure S29: **Load paths and stored energy landscape variation of case C8 RF=0.80.** Creases made of: AG30, DM60, DM70, DM85 and DM95. Results for C8 RF=0.80 cells at a 1:1 scale (×1). Filled regions include FEA simulations within the range $\tau_i^* \leq \tau \leq n\tau$.

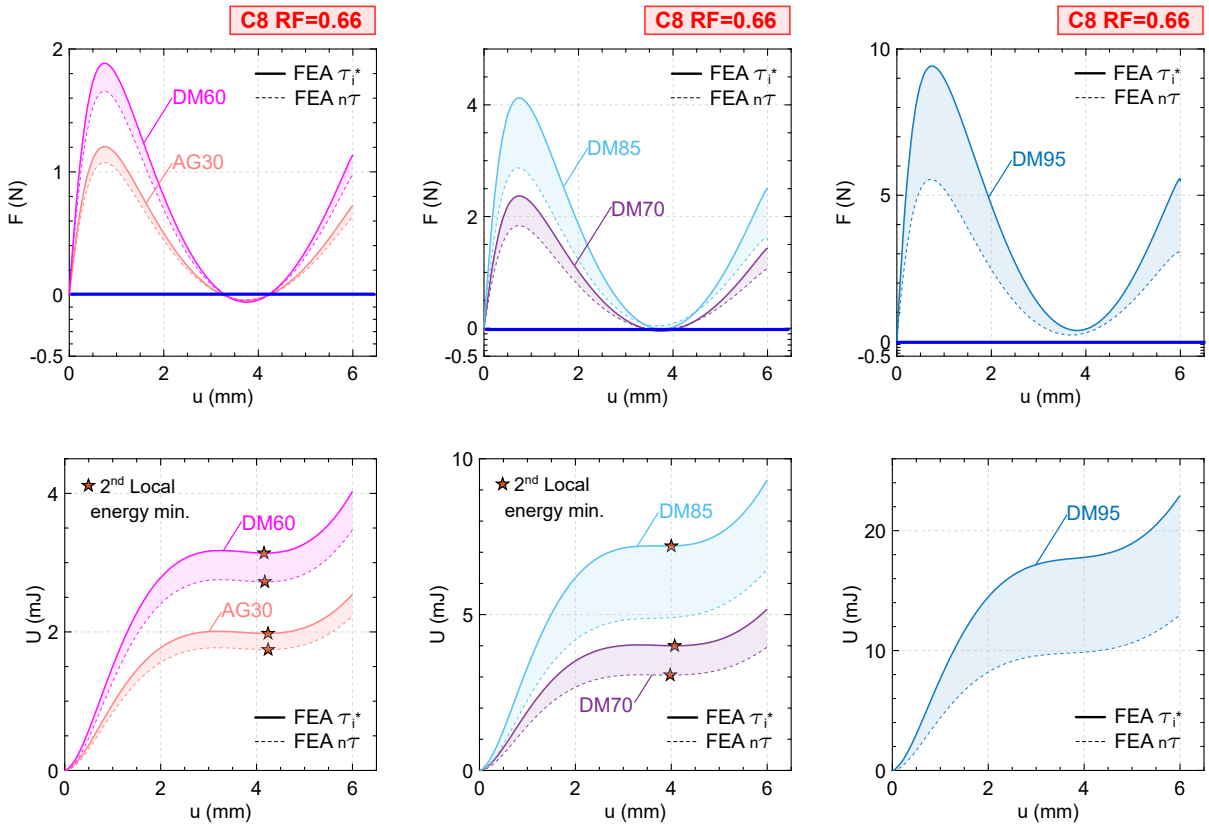

Figure S30: **Load paths and energy landscape variation of case C8 RF=0.66.** Creases made of: AG30, DM60, DM70, DM85 and DM95.Results for C8 RF=0.66 cells at a 1:1 scale (×1). Filled regions include FEA simulations within the range $\tau_i^* \leq \tau \leq n\tau$.

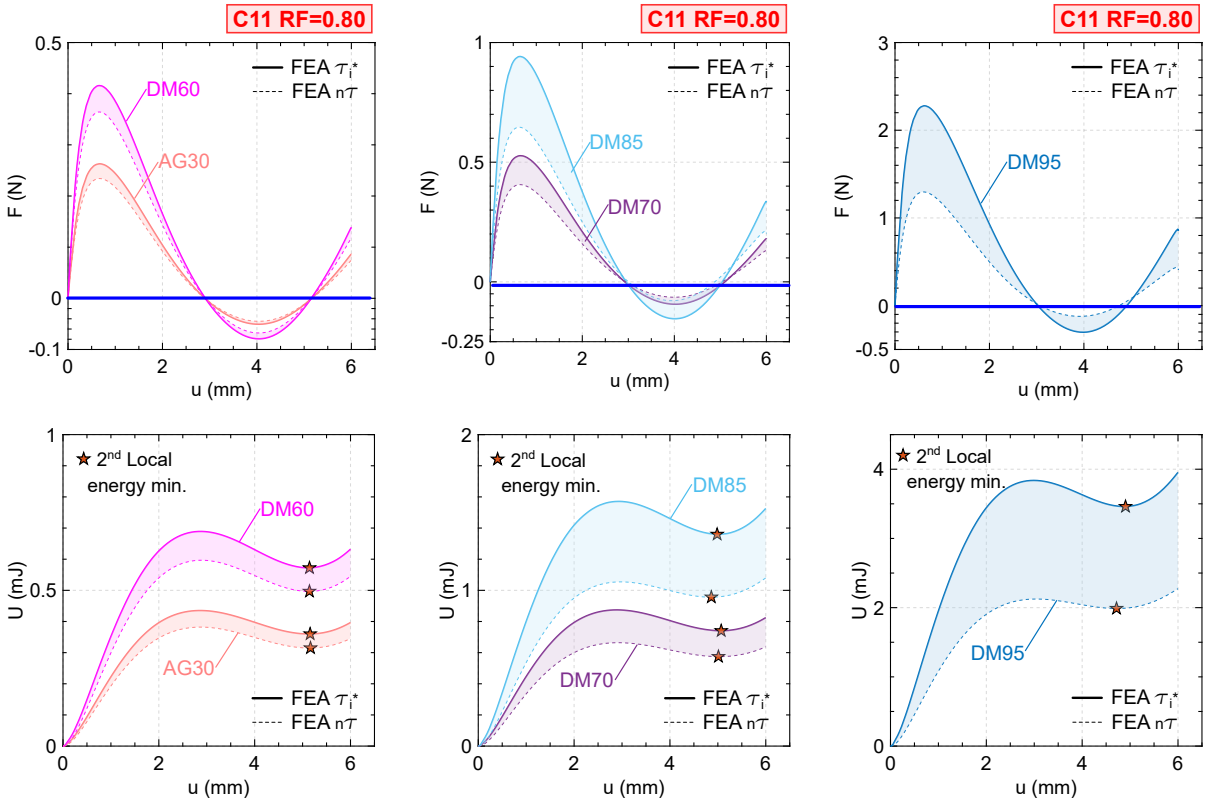

Figure S31: **Load paths and energy landscape variation of case C11 RF=0.80.** Creases made of: AG30, DM60, DM70, DM85 and DM95. Results for C11 RF=0.80 cells at a 1:1 scale (×1). Filled regions include FEA simulations within the range $\tau_i^* \leq \tau \leq n\tau$.

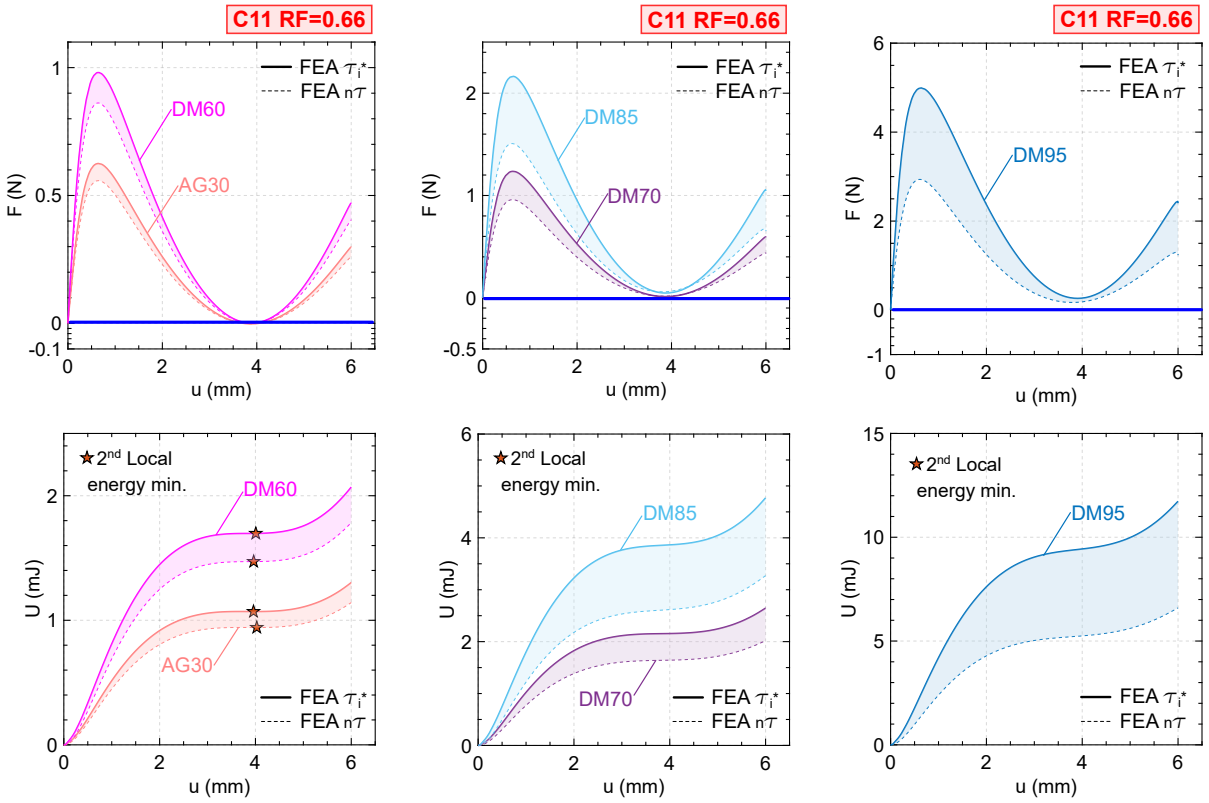

Figure S32: **Load paths and energy landscape variation of case C11 RF=0.66.** Creases made of: AG30, DM60, DM70, DM85 and DM95. Results for C11 RF=0.66 cells at a 1:1 scale (×1). Filled regions include FEA simulations within the range $\tau_i^* \leq \tau \leq n\tau$.

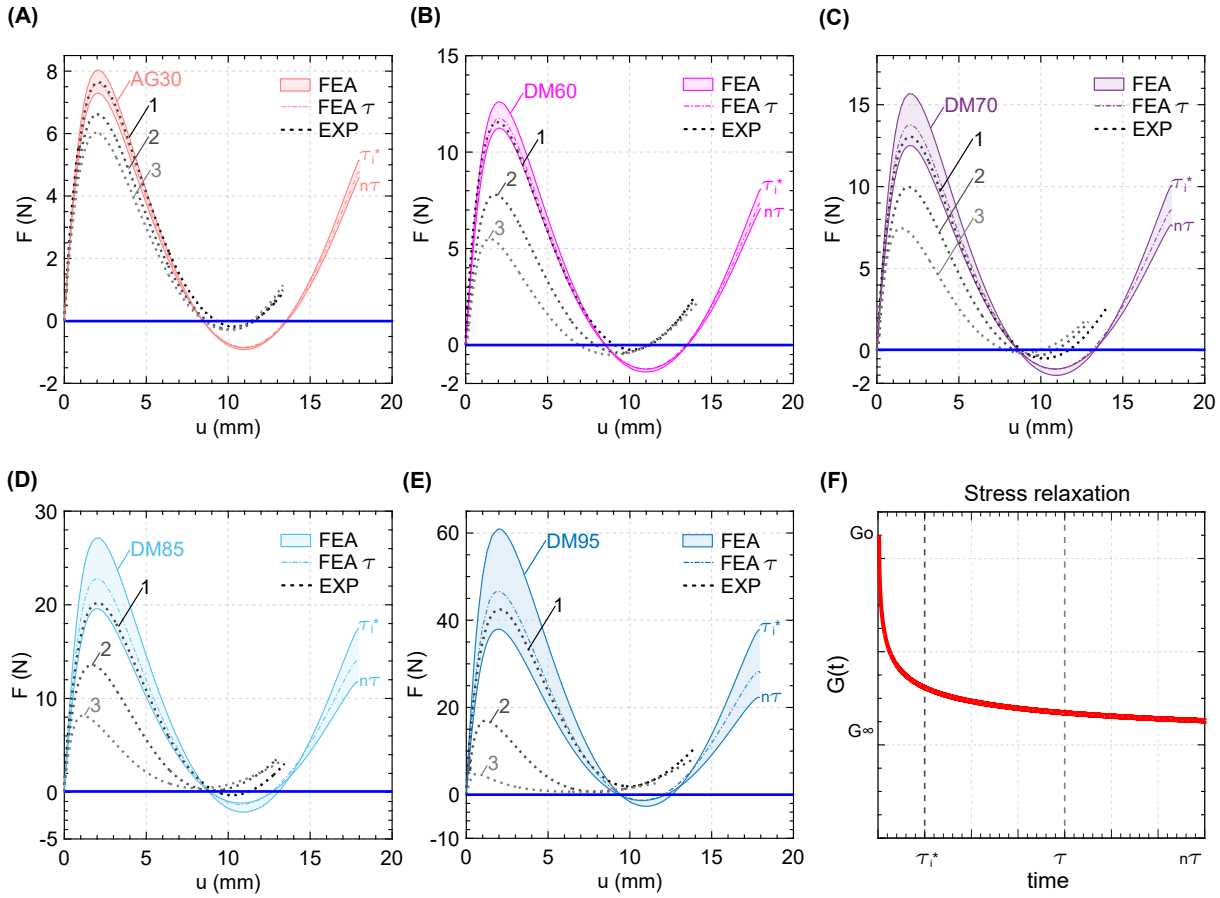

Figure S33: **Effect of the degradation of the rubbery crease cross-sections on the load path.** Experimental results after performing three sequential tests on Kresling cells C8 RF=0.80 with creases made of: **(A)** AG30, **(B)** DM60, **(C)** DM70, **(D)** DM85 and **(E)** DM95. Kresling cells fabricated at a 3:1 scale. Filled regions include FEA simulations within the range $\tau_i^* \leq \tau \leq n\tau$. (F) Experimental relaxation curve. Times τ_i^*, τ and nτ, respectively considered for the numerical analysis of viscosity effects. Experiments were performed at a test speed which correspond to a relaxation time τ_i^*=180 s.

S.2.5 Monomaterial Kresling cells: Complementary Results

The load paths and stored energy landscapes of the rubbery photopolymers DM60, DM70 and DM85 are shown in Fig. S34. They exhibited monostability and complement the analyses presented for monomaterial Kresling cells, as described in Section 2.5.

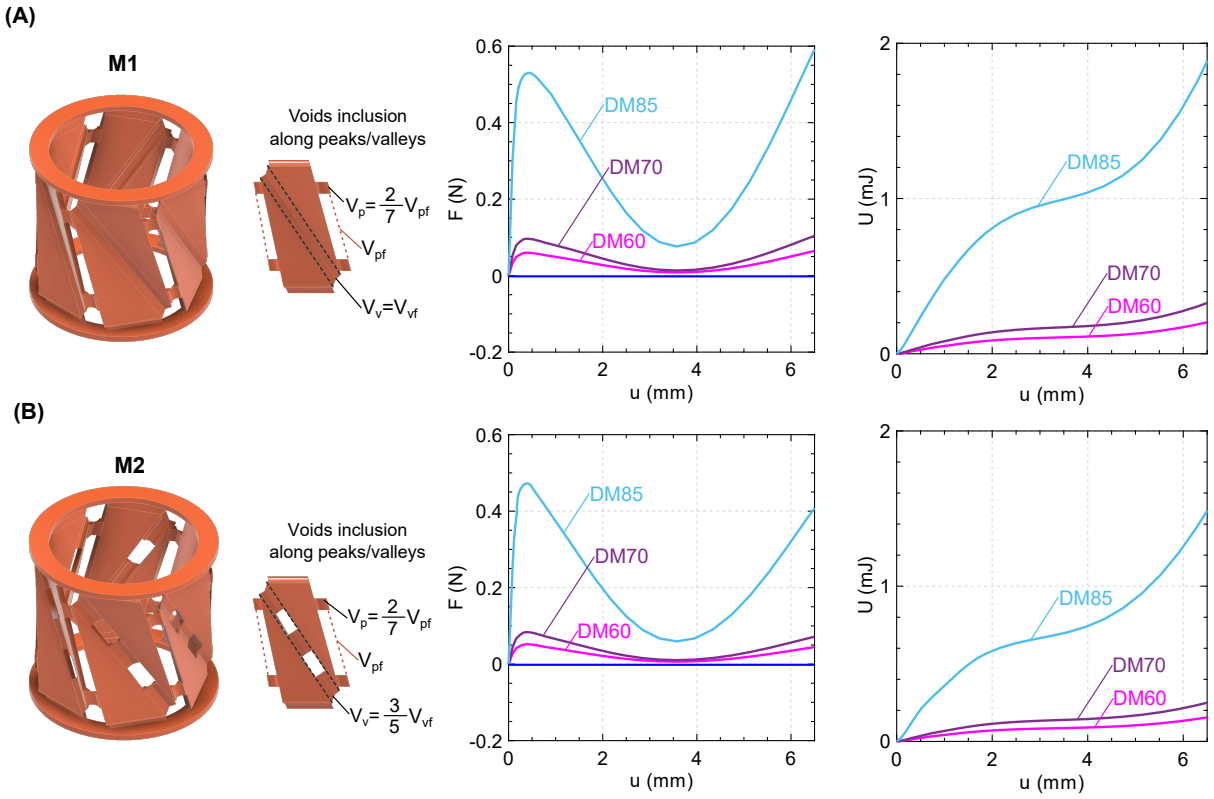

Figure S34: **Load paths and energy landscapes of Monomaterial Kresling cells**. Cases with variable void inclusions along the creases: **(A)** M-1 and **(B)** M-2. Results of Kresling cells at a 1:1 scale.

Caption for Video S1. Experimental validation of the parametric study on crease geometry of 3D printed Kresling cells. Comparison between Numerical (FEA) and Experimental (Exp) load path results from compressive tests on the C8 case. Kresling cell creases, generated with reduction factors RF = 0.80, 0.66, and 0.50, exhibited bistable or monostable behavior.

Caption for Video S2. Hands-on Experimental validation of Bistability in 3D printed Kresling cells. Evidence of bistable or monostable behavior in various Kresling cells with creases made of DM60. The creases were generated with reduction factors in the range of $0.25 \leq RF \leq 0.80$ and an intact crease case (INT).

Caption for Video S3. Experimental validation of the crease degradation in 3D printed Kresling cells. Effect of rubbery crease cross-section degradation on the load path, observed after three sequential experiments on the same sample (C8, RF=0.80, creases made of DM60).

Caption for Video S4. Effects of viscosity on bistable Kresling cells: Hands-on experimental validation. Evidence of bistable or monostable behavior in Kresling cells (C8, RF = 0.80) with creases made of rubbery materials that have different viscosity and relaxation modulus compared to DM60 (G_{60}=0.220 MPa):AG30 ($G_\infty=0.7G_{60}$), DM70 ($G_\infty=1.4G_{60}$), DM85 ($G_\infty=2.6G_{60}$), and DM95 ($G_\infty=3.9G_{60}$).

Caption for Video S5. Programmable Monostable Kresling Assemblies. Compression test, folding process, and load paths from numerical (FEA) and experimental (EXP) analysis for the following cases: (i) all creases made of DM60, (ii) stiffer creases (DM95) in the even layers, and (iii) stiffer creases (DM95) in the odd layers. Numerical simulations stopped at the first contact between panels.

Caption for Video S6. Prototyping of 3D printed Kresling cells via Polyjet technique. Different stages of fabrication and post-processing for multi-material 3D-printed Kresling cells using a Stratasys J750 printer within the PolyJet framework.